Thèse de doctorat

Pour l'obtention du grade de Docteur délivré par

L'Université Sultan Moulay Slimane

Discipline**: Physique**

Spécialité**: Physique des matériaux**

Présentée et soutenue publiquement par

OUKAHOU Said

Le 09 Juin 2023

Atomistic simulation of physical and chemical properties of materials for energy storage

Membres du jury :

Président :	M. Bouchaib Manoun	Professeur à la Faculté des Sciences et Techniques, Settat ;
Rapporteurs :	M. Bouzid Manaut	Professeur à la Faculté Polydisciplinaire, Beni Mellal ;
	M. Ahmed Fathi	Professeur à la Faculté Polydisciplinaire, Khouribga ;
	M. Taoufik Mouhib	Professeur à l'Ecole Nationale des Sciences Appliquées, Berrechid ;
Examinateur:	M. My. Mustapha charafi	Professeur à la Faculté Polydisciplinaire, Khouribga ;
Co-directeur de thèse:	M. Abdellatif HASNAOUI	Professeur à la Faculté Polydisciplinaire, Khouribga ;
Directeur de thèse :	M. Khalid SBIAAI	Professeur à la Faculté Polydisciplinaire, Khouribga.

Contents

List of Figures

List of Tables

Abstract

Providing cleaner sources of energy will require significant improvements to the solid-state materials available for energy storage and conversion technologies. Rechargeable lithium batteries are generally considered the best candidates available for future energy storage applications, especially for implementation in hybrid or fully electric vehicles, due to their series of advantages such as high energy density, stability, high voltage, and low weight. Nevertheless, the production of the future generation of rechargeable batteries will require significant improvements in the materials used for the cathode, anode and electrolyte. In this context, lithium manganese phosphate $LiMnPO_4$ (LMP) has attracted significant attention as cathode material for lithium-ion batteries (LIBs) due to its outstanding properties such as high voltage, good stability, identical theoretical capacity to LFP, environmental friendliness, and inexpensive cost. However, LMP suffers from low electronic and ionic conductivities. Therefore, this thesis aims to improve these characteristics of LMP by Ni/Fe single-doping, Ni–Fe co-doping, and biaxial strain strategies using density functional theory (DFT). Firstly, the mixed olivine structures $LiMn_{1-x}M_xPO_4$ / $Mn_{1-x}M_xPO_4$ (M= Ni, Fe; x=0, 0.25, 0.5, 0.75, 1)) phases are investigated. The results revealed that Ni and Fe affected the structural, electronic, kinetic, electrochemical potential and magnetic properties. The unit cell volume of LMP has been shown to decrease with increasing Ni and Fe concentrations in Mn sites. The open circuit voltage of $LiMn_{1-x}Ni_xPO_4$ slightly increases from 4.39V (for LMP) to 4.41V (for $LiMn_{0.25}Ni_{0.75}PO_4$) which indicates a good improvement of Li-intercalation voltages with increasing the concentration of Ni. Moreover, the band gap (E_g) of LMP (3.62 eV) is reduced with substitutions of Mn sites by Ni and Fe, especially for the compounds $LiMn_{0.5}Ni_{0.5}PO_4$ (2.77 eV) and $LiMn_{0.5}Fe_{0.5}PO_4$ (3.35 eV), improving hence the electronic conductivity. Furthermore, the diffusion energy barrier of Li-ion in $Mn_{0.5}Ni_{0.5}PO_4$ (0.34 eV) and $Mn_{0.5}Fe_{0.5}PO_4$ (0.39 eV) are found to be lower than the pristine $MnPO_4$ (0.42 eV), indicating that 50 % of either Fe or Ni is beneficial to improve the kinetic properties in LMP. Secondly, the effect of Ni–Fe codoping on the electrochemical performance of lithiated/delithiated pristine phases (i.e. $LiMn_{0.5}Ni_{0.25}Fe_{0.25}PO_4$ (LMNFP)/ $Mn_{0.5}Ni_{0.25}Fe_{0.25}PO_4$ (MNFP)) are investigated using DFT calculations. The results indicate that Ni–Fe co-doping affect the structural, electronic, kinetic properties, and electrical conductivity of pristine LMP. The volume of LMP decreases with Ni–Fe codoping. Moreover, a small change in unit cell volume between lithiated and delithiated phases is found for all structures, indicating good reversibility during Li insertion/extraction. Ni–Fe codoping reduces the band gap of LMP

from 3.62 to 1.55 eV resulting in a good improvement in the electronic conductivity. The migration barrier energy was calculated to be 0.34 eV for Li-ions in MNFP, which is lower than that of MP (0.40 eV) indicating that Ni–Fe codoping is beneficial for enhancing the ionic conductivity of pristine LMP. Moreover, the effect of biaxial strain on the rate performance of pristine LMP has been investigated. The findings suggest that the biaxial tensile strain has a remarkable effect on the rate performance of LMP cathode material. The biaxial tensile strain of +2% reduces the band gap of LMP from 3.51 to 3.41eV and ameliorates the diffusion coefficient by 100 times. Furthermore, the migration barrier was calculated to be 0.37 eV for strained (+2%) defective MP, lower than 1.12 eV for unstrained defective MP, indicating that biaxial tensile strain can also mitigate the negative effect of anti-site defects on Li-ion migration.

Résumé

Le phosphate de lithium manganèse $LiMnPO_4$ (LMP) a attiré beaucoup d'attention en tant que matériau cathodique pour les batteries lithium-ion (LIB) en raison de sa série d'avantages tels que la haute tension, la bonne stabilité, la capacité théorique identique à celle du LFP, le respect de l'environnement et le faible coût. Cependant, le LMP souffre de faibles conductivités électronique et ionique. Par conséquent, cette thèse vise à surmonter ces inconvénients du LMP par des stratégies de dopage simple Ni/Fe, de codopage Ni–Fe et de déformation biaxiale en utilisant la théorie fonctionnelle de la densité (DFT).

Premièrement, les structures olivines mixtes $LiMn_{1-x}M_xPO_4$/ $Mn_{1-x}M_xPO_4$ (M= Ni, Fe ; x=0, 0.25, 0.5, 0.75, 1)) ont été étudiées. Les résultats ont révélé que Ni et Fe affectent les propriétés structurelles, électroniques, cinétiques, le potentiel électrochimique et les propriétés magnétiques. Le volume cellulaire unitaire du LMP diminue avec l'augmentation des concentrations de Ni et de Fe dans les sites Mn. La tension en circuit ouvert de $LiMn_{1-x}Ni_xPO_4$ a légèrement augmenté de 4.39V (pour LMP) à 4.41V (pour $LiMn_{0.25}Ni_{0.75}PO_4$) ce qui indique une bonne amélioration des tensions d'intercalation de Li- avec l'augmentation de la concentration de Ni. De plus, la bande interdite (Eg) des LMP (3,62 eV) est réduite avec la substitution des sites Mn par Ni et Fe, notamment pour les composés $LiMn_{0.5}Ni_{0.5}PO_4$ (2,77 eV) et $LiMn_{0.5}Fe_{0.5}PO_4$ (3,35 eV) améliorant ainsi la conductivité électronique. De plus, la barrière d'énergie de diffusion de Li-ion dans $Mn_{0.5}Ni_{0.5}PO_4$ (0.34 eV) et $Mn_{0.5}Fe_{0.5}PO_4$ (0.39 eV) est inférieure à celle du $MnPO_4$ pur (0.42 eV), ce qui indique qu'un dopage avec 50 % de Fe ou de Ni est bénéfique pour améliorer les propriétés cinétiques dans le LMP. Deuxièmement, l'effet du codopage Ni-Fe sur les performances électrochimiques des phases pristines lithiées/délithiées (c'est-à-dire $LiMn_{0.5}Ni_{0.25}Fe_{0.25}PO_4$ (LMNFP)/ $Mn_{0.5}Ni_{0.25}Fe_{0.25}PO_4$ (MNFP)) a été étudié à l'aide de calculs DFT. Les résultats indiquent que le codopage Ni-Fe affecte les propriétés structurelles, électroniques, cinétiques et la conductivité électrique du LMP primitif. Le volume du LMP diminue avec le codopage Ni-Fe. En outre, un faible changement du volume de la cellule unitaire entre les phases lithiées et délithiées a été trouvé pour toutes les structures, indiquant une bonne réversibilité pendant l'insertion/extraction du Li. Le codopage Ni-Fe réduit la bande interdite des LMP de 3.62 à 1.55 eV, ce qui entraîne une bonne amélioration de la conductivité électronique. L'énergie de la barrière de migration a été calculée à 0.34 eV pour les ions Li- dans le MNFP, ce qui est inférieur à celle du MP (0.40 eV), indiquant que le codopage Ni-Fe est bénéfique pour

améliorer la conductivité ionique du LMP vierge. Troisièmement, l'effet de la déformation biaxiale sur les performances du LMP primitif a été exploré. Les résultats suggèrent que la déformation en traction biaxiale a un effet remarquable sur la performance du matériau cathodique LMP. La déformation biaxiale de +2% réduit la bande interdite du LMP de 3.51 à 3.41eV et améliore le coefficient de diffusion de 100 fois. En outre, la barrière de migration des ions Li calculée dans le composé MP défectueux déformé à +2% (0.37 eV), a été trouvée inférieure à celle calculée dans le composé MP défectueux non déformé (1.12 eV), ce qui indique que la déformation en traction biaxiale peut également atténuer l'effet négatif des défauts antisites sur la migration des ions Li-ion.

List of Publications

Oukahou, S.; Maymoun, M.; Elomrani, A.; Sbiaai, K.; Hasnaoui, A. Enhancing the electrochemical performance of olivine $LiMnPO_4$ as cathode materials for Li-Ion Batteries by Ni-Fe co-doping. **ACS Applied Energy Materials** 2022, 1-8.

Oukahou, S.; Elomrani, A.; Maymoun, M.; Sbiaai, K.; Hasnaoui, A. Investigation of $LiMn_{1-x}M_xPO_4$ (M = Ni, Fe) as cathode materials for Li-ion batteries using density functional theory. **J. Computational Materials Science** 2022, 202, 1–11.

Maymoun, M.; **Oukahou, S**.; Elomrani, A.; Sbiaai, K.; Hasnaoui, A. Surface functionalization of penta-siligraphene monolayer for nanoelectronic, optoelectronic and photocatalytic water-splitting: a first-principles study. **Applied Surface Science**. 2022, 590, 152972.

Maymoun, M.; **Oukahou, S.**; Bahou, Y.; Hasnaoui, A.; Sbiaai, K. Strain- and electric field-enhanced optical properties of the penta-siligraphene monolayer. **New Journal of Chemistry**. 2022, 46 (29), 13905–13917.

Elomrani, A.; Lamhani, M.; **Oukahou, S.**; Sbiaai, K.; Lebègue, S.; Hasnaoui, A. Two dimensional h-BSb mono-layer as a promising anode material for lithium-ion batteries studied from ab initio simulations. **Materials Chemistry and Physics**. 2021, 275, 125191.

Maymoun, M.; Elomrani, A.; **Oukahou, S.**; Bahou. Y.; Hasnaoui, A.; Sbiaai. K. Enhancement in photocatalytic water splitting using van der Waals heterostructure materials based on penta-layers. **Physical Chemistry Chemical Physics (PCCP)**. 2023, 25, 3401–3412.

Elomrani, A; Maymoun, M.; **Oukahou, S.**; Lamhani, M.; Sbiaai, K.; Hasnaoui, A. Evaluating the potential of planar h-BSb monolayer as anode materials for sodium-ion batteries from first principles methods. **Journal of Energy Storage**. 2023, 64, 107260.

S. Oukahou*, A. Elomrani, M. Maymoun, K. Sbiaai, A. Hasnaoui*; Strain Enhanced Electrochemical Performance of Olivine LiMnPO4 as Cathode Materials for Li-Ion Batteries. **To be submitted 2023.**

Acknowledgements

The research summarized herein could not have happened without support from many different people who contributed in various ways. First, I would like to thank God for ongoing good health, living conditions & inspiration during the entire time of my research, which was a great boost to scientific progress.

In particular, I would like to express my deepest gratitude to my supervisors, **Prof. Khalid Sbiaai** and **Prof. Abdellatif Hasnaoui** for their inspirational guidance, patience, continuous support, critical comments, and unreserved support throughout my research work, at times responding to emails late at night and early in the morning; so, their selflessness and tirelessly providing consistent support will be in my memory forever. I would also like to express my sincere gratitude to all professors of Master **MMR** at the Polydisciplinary Faculty of Khouribga for their wonderful lessons in the class, useful pieces of advice, and discussions.

I would also like to thank the members of the Jury: **Mr. Bouchaib Manoun**, **Mr. Bouzid Manaut**, **Mr. Taoufiq Mouhib**, **Mr. Ahmed Fathi** and **Mr. My. Mustapha charafi**. Thank you for your advice and your pertinent comments.

My appreciation also goes to all the friends I have made along this journey, for all the laughter we have shared and support you have shown. I would like to thank my lab mates, colleagues and research team, and especially **Mohammad Maymoun**, **Hassan Ataalite**, **Abdelali Elomrani**, **Mohammed Lamhani**, **Fatihi Mohamed yassine**, **Youssef Ouldhnini**, **Abdelali Samiri**, **Hayat Haouas**, for the cherished time spent together in the lab, and in social settings. **Drs. Anass Bendaraa**, **Moloudi Dardouri, Abderrahim Khmich** and **Prof. Abdessamad HASSANI** have been incredible mentors, and I'm also grateful to them.

Last but not least, I would like to express my deep and sincere gratitude to my parents, my brothers and my sisters for their unwavering love, support and encouragement all through my studies.

Finally, there is an almost endless list of people who I would, and indeed should, like to thank for their assistance and support during the completion of my PhD. So, if you're reading this and feel I haven't mentioned you directly, when I perhaps should have done, then I can only but apologise and attempt to reassure you that your omission was not intentional!

General introduction

Owing to the widespread consumption of fossil fuels, the two main global challenges facing the world today are climate change and energy issues. To mitigate and overcome these challenges, numerous efforts have been devoted by many researchers, including capturing CO_2 and using cleaner energy resources as an alternative to petroleum or diesel in vehicular applications [1-5]. In accordance, the development of rechargeable batteries for green and cheap energy storage is the fundamental technological endeavors. More specifically, lithium-ion rechargeable batteries (LIBs) have attracted much attention as promising candidates for storage energy due to their series of advantages such as high energy density, long life cycle, and low weight. They are used in a wide range of applications from small-scale electronic technologies including cell phones, laptops, cameras, and so forth to large-scale applications such as smart grids and electric vehicles. However, recent societal developments, especially in high-tech applications, have led to an increasing requirement for LIBs with relatively improved performance such as high energy density, lightweight, low price, and long lifetime as well as high safety [6, 7]. In this regard, it is worth noting that the cathode materials represent one of the main components of batteries, which generally determine their electrochemical efficiency [8]. Layered oxide materials such as $LiCoO_2$, $Li_{1-x}(Ni_{0.33}Mn_{0.33}Co_{0.33})O_2$, and $LiNi_{0.80}Co_{0.15}Al_{0.05}O_2$ have been widely used as cathode materials in commercial LIBs; however, they face several challenges that limit their application in high-energy devices including voltage decay, rapid capacity loss, O_2 emission at high temperatures, and they contain a toxic and expensive element, that is, cobalt [9]. Therefore, significant efforts have been devoted to finding alternatives to layered oxide cathodes.

Since its discovery in 1997, the olivine $LiFePO_4$ (LFP) has been emerging in the energy-storage world as an efficient cathode material for LIBs owing to its series of advantages such as excellent cycling stability, ecological friendliness, high theoretical capacity, low cost and high thermal safety (LFP was revealed to be stable up to 400°C) [10, 10]. Nevertheless, the low Fe^{3+}/Fe^{2+} redox potential (3.4 V vs Li^+/Li) results in a low energy density of LFP limiting its application in high-energy devices [12, 13]. Consequently, many researchers have focused on other members of the olivine phosphates group, for instance, $LiNiPO_4$ (LNP), $LiCoPO_4$ (LCP) and $LiMnPO_4$ (LMP) to overcome energy-density drawbacks. LNP and LCP exhibit high potential which exceeds the safety voltage of the most commercial liquid electrolytes, wherein they present 4.7 and 5.2 V vs Li/Li^+, respectively [14]. On the other hand, LMP has a

compatible potential (4.1 V vs Li/Li^+) with the current electrolyte windows [15, 17]. In addition to suitable redox potential, LMP has other advantages like good stability, environmental friendliness, low cost and maximum energy density (700 Wh.kg-1) [17, 18], which suggests LMP as a promising candidate cathode material for LIBs. However, LMP suffers from low electronic and ionic conductivities which reduces its efficiency as cathode material [19, 20]. To overcome these constraints, numerous methods have been used such as coating LMP with carbon (C) [21], reducing its crystal size [22] and cation doping [23]. In this context, this thesis aims to get rid of these LMP drawbacks by Ni/Fe single-doping, Ni–Fe co-doping, and biaxial strain strategies using density functional theory (DFT). We will investigate then the effect of single Ni (or Fe) doping on the performance of LMP as a cathode material by computing its electrochemical, structural and electronic properties to show how doping can be beneficial to LMP. Optimal doping concentrations will be determined. Motivated by the results obtained in this first part, we will investigate the effect of the simultaneous doping with Ni and Fe on the LMP properties using different doping compositions which then will provide the values to suggest for optimal use. Moreover, and to be close to a realistic situation, we show how the biaxial stress can affect the electronic properties of defective LMP.

This thesis is organized into six chapters:

C**hapter 1** begins with giving an overview of the rechargeable battery concept, their component materials, as well as key cathode materials, and the objectives covered in this thesis.

Chapter 2 provides a brief discussion of the Quantum mechanical methods we used during this thesis. We present a brief discussion of the Schrodinger equation, the Born-Oppenheimer approximation, the Kohn and Sham equations, the local density approximation (LDA), and the generalized gradient approximation (GGA) as well as the method of solving the Kohn and Sham equations. Finally, the method used to locate the transition state and extract the migration barrier of the Li-ion is also described; it is the Nudged Elastic Band.

Chapter 3 presents a detailed study of the geometry, electrochemical potential, capacity, and electronic structure of mixed olivine phases $LiMn_{1-x}M_xPO_4$ / $Mn_{1-x}M_xPO_4$ (M= Ni, Fe; x=0, 0.25, 0.5, 0.75, 1) using DFT calculations.

Chapter 4 presents a study on the effect of Ni–Fe codoping on the structural, electronic, magnetic, electrochemical potential, and kinetic properties of Li-ions in pristine LMP, as well

as on the thermodynamic stability, theoretical capacity, charge transfer, average M–O bond lengths, and electrical conductivity. In addition, the thermodynamic stability and charge transfer of Ni/Fe single doping in lithiated/delithiated ($LiMnPO_4$/$MnPO_4$) pristine phases are investigated using DFT calculations.

Chapter 5 provides a study on the effect of biaxial strain on the dynamic and thermal stabilities, structural, electronic, ionic diffusion, electrochemical potential, and defect properties of $LMnPO_4$ (LMP) structure, as well as on the average (Mn–O, Li–O, and P–O) bond lengths, electrical conductivity, and charge transfer. The influence of intrinsic defects on Li-ion migration in strained and unstrained LMP is also discussed, using DFT calculations.

Lastly, **Chapter 6** summarizes the conclusions from this thesis and recommendations for future work.

Chapter 1

Background

1.1 Background: Energy Storage

The development of clean and sustainable energy sources is one of the most significant global challenges. There is a widespread effort to reduce the use of fossil fuels due to their limited supply and concern over the implications of global warming driven by CO_2 emissions. Around 25% of CO_2 emissions in developed countries arise from road transport [24]. It is therefore widely acknowledged that the electrification of transport is needed to address this problem. The main barrier is the storage of electrical energy, which lies at the heart of these hybrid and electric vehicles. In addition, with a shift towards utilizing sustainable natural energy resources such as solar, wind, hydro, tidal, geothermal, and biomass energy, which are inherently intermittent, energy storage will also play a vital role in large-scale applications, such as grid energy storage [25]. Therefore, energy storage technologies are considered as one of the major options for clean energy.

Lithium-ion batteries (LIBs) have been successfully and widely implemented in many applications, from electronic portables to vehicle electrics, due to their high energy density, stability, high voltage and low weight [9]. However, more performance improvements are needed for implementation into high-energy devices such as electric and hybrid vehicles, which requires both high energy density and power density [6, 26]. This improvement is significantly related to the components of the battery systems such as the cathode, anode, separator and electrolyte [1]. Notably, it is worth emphasizing that one of the main drawbacks to progress is a lack of excellent and suitable cathode materials which can meet the rigorous requirements for high-power applications in terms of cost, safety and environmental concerns. For example, most commercial LIBs use an expensive and toxic cathode material (i.e. $LiCoO_2$) which cannot meet the stringent requirements of high-power applications [27]. Therefore, many researchers and engineers are focusing on developing or designing new positive electrodes with improved performances.

There is often a lack of atomic-scale understanding of the structural, electronic, transport, and defect properties underpinning these complex lithium battery materials. As a result, many

researchers have focused on a combination of computer modeling and experimental techniques to improve current systems and develop newer, more efficient ones. In this context, this thesis details the study of olivine materials as promising cathode materials for Li-ion batteries by computational modeling techniques. The following sections of this chapter will present an overview of the rechargeable battery concept, their component materials, as well as key cathode materials and the objectives covered in this thesis.

1.2 Lithium-ion Batteries

Lithium is both the most electropositive metal (with a redox potential of -3.04 V versus the standard hydrogen electrode) and the lightest metal in the periodic table (M = 6.94 g mol^{-1}). In addition, lithium has other outstanding properties such as a wide temperature range of operation and a low self-discharge rate, which means it is an excellent component for high-energy density rechargeable batteries. Lithium batteries were first advanced in the 1950s after the discovery of the stability of the metal Li in aqueous electrolytes. These cells were marketed by the early 1970s for low-power applications that required long operating times such as watches, calculators and a selection of small medical devices. Nevertheless, around the same time, intercalation compounds were discovered, which allowed reversible insertion and extraction of Li ions. Their discovery was an important step forward and changed the research focus to the development and production of high-energy rechargeable (secondary) lithium-based battery systems [28, 29].

In the 1972s, Exxon demonstrated the first non-aqueous rechargeable lithium cell based on TiS_2 as a positive electrode, lithium metal as the negative electrode, and lithium perchlorate in dioxolane as the electrolyte. TiS_2 was considered the best intercalation compound available at the time, facilitating reversible Li ion insertion with minimal structural change. Unfortunately, the lithium anode posed several safety concerns [28]. Li metal reacts violently to water, so the cells had to be constructed in a dry atmosphere and built watertight, which increased the production costs of the cell [29]. In addition, during the operation, Li ions are shuttled back and forth between the anode and cathode; this requires the lithium anode to be repeatedly stripped and re-plated, leading to the formation of uneven (dendritic) Li growth at the anode. The dendrites would eventually extend across to the cathode resulting in a short circuit that often led to dangerous explosions. In this regard, several strategies were proposed to address these problems [30]. The most successful of them is the replacement of the lithium metal anode with an intercalation material. In this strategy, lithium is present in its ionic rather than

metallic state, eliminating the problem of dendritic growth and rendering the cells safer. The same strategy of using intercalation compounds at both the cathode and anode is still employed by modern rechargeable lithium-ion batteries.

Like all batteries, lithium-ion batteries are constituted of three main components, that are the positive electrode (high potential with respect to Li^+/Li), a negative electrode (low potential with respect to Li^+/Li), separated by an electrolyte which ensures the transfer of Li^+ ions during the charge and discharge of the battery. Figure 1.1 presents a schematic of Li-ion battery operation, showing the highly successful Sony cell, composed of a $LiCoO_2$ cathode and a graphite anode. During discharging of the battery, the negative electrode releases Li^+ ions to migrate through the electrolyte and are inserted into the crystal lattice of the positive electrode "insertion material".

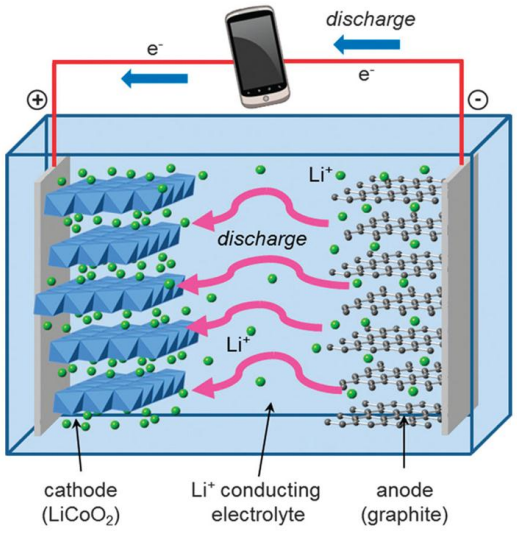

Figure 1.1: Schematic of a typical rechargeable lithium-ion battery with a $LiCoO_2$ cathode and a graphite anode [31].

Each Li^+ ion circulating between the two electrodes is associated with an electron. This electron transfers from the negative electrode to the positive electrode in the external circuit to preserve the electrical neutrality in each electrode. It should be noted that for such electric charge movements, there must be a potential difference between the two electrodes, and this difference results from the difference in the reactions occurring simultaneously at the electrodes: oxidation reaction at the negative electrode and reduction reaction at the positive electrode [28, 32, 33]. During charging, the reverse process is imposed by the supply of an external current, during which Li^+ ions re-enter the host structure of the negative electrode

material. The reactions occurring at the electrodes during the discharge can be written according to equations 1.1 and 1.2

$$\text{Anode:} \qquad Li_xC_6(s) \rightarrow 6C + xLi^+ + xe^- \tag{1.1}$$

$$\text{Cathode:} \quad Li_{1-x}CoO_2(s) + xLi^+ + xe^- \rightarrow LiCoO_2(s) \tag{1.2}$$

In 1991, SONY discovered the first commercial lithium-ion rechargeable batteries (LIBs) based on $LiCoO_2$ as the cathode part, graphite anode and an electrolyte of $LiPF_6$ dissolved in an organic solvent [34]. Since then, LIBs have been widely used in portable electronic devices, electric vehicles, and large-scale energy storage systems, due to their high energy density, low weight, high voltage, and long life cycle in addition to a flexible design [9, 35]. However, further improvements in LIBS performance are needed to fulfill the stringent requirements of high-power applications in terms of cost, safety and environmental concerns. It is very important to find cheaper and more abundant materials for this technology, but it is necessary to consider reliability, performance and safety. The following sections provide an overview of the three main components of a Li-ion battery and their role within the cell. Since the research presented here focuses on cathode materials, these are covered in more detail.

1.3 Electrolyte Materials

In order to avoid a short circuit, the two electrodes must be separated. Therefore, a thin porous material is inserted between them to keep them apart. The electrolyte has the essential job of facilitating the movement of lithium ions between the cathode and the anode through this porous separator. Consequently, the electrolyte must be an excellent ionic conductor but an electronic insulator otherwise the cell would short circuit [36].

In conventional lithium-ion batteries, the electrolyte is typically a lithium salt $LiPF_6$ dissolved in a mixture of organic solvents because these solutions are compatible with the battery's operating voltage window and offer high ionic conductivities. Although the specific mixture of organic solvents used depends on the battery manufacturer, ethylene carbonate (EC) is always present because of its crucial role in the reversibility of the reaction at the anode. In addition, EC decomposes on the graphite surface forming a solid electrolyte interface (SEI) which is a crucial layer that prevents other solvent molecules from co-intercalating with lithium in the graphite layers [37].

These typical organic-based electrolytes are thermodynamically stable up to 3.5 V, above this value, the electrolyte decomposes. Fortunately, the decomposition process is kinetically controlled, which means that in practice, cells containing these electrolytes can operate at voltages as high as 5.5 V. Even though the process of electrolyte decomposition is slow, it still happens continuously over the lifetime of the battery, causing a gradual decline in performance. The safety issues associated with using organic-based liquid electrolytes have led to a particular interest in the development of all-solid-state batteries [38].

1.4 Anode Materials

An ideal anode material will have a low potential relative to Li/Li+ and will allow highly reversible intercalation of Li ions during continuous discharge-recharge cycles. As seen previously, lithium metal was originally utilized in the first cells as an anode material. Nevertheless, dendritic growth due to continuous re-plating of its surface during cycling led to serious safety issues. However, since Li metal offers higher capacity than any of its possible alternatives (see Figure 1.2), there is still a significant amount of ongoing research investigating rechargeable battery cells using Li metal anodes. The most effective method to overcome these problems involved replacing the Li metal with an intercalation material. However, it should be noted that it has taken nearly ten years to identify a suitable intercalation material to serve as an anode. Therefore, the development of the Li-ion battery has been somewhat hampered. These 10-year failures were attributed to the lack of suitable anode materials and the inability of electrolytes to fulfill safety, cost, and performance requirements [28, 33, 39].

The current anode material is graphite, which allows lithium to be inserted between the carbon layers. The popularity of this compound is due to its good electrical and ionic conductivities, good structural stability upon lithiation/delithiation, low insertion voltage (~ 0.2-0.05 V vs. Li^+/Li), low cost, abundance and environmental friendliness. However, it has a relatively low capacity of 372 $mAh.g^{-1}$. This value represents a severe storage limitation compared to Li metal, which has a storage capacity of 3800 $mAh.g^{-1}$ [37]. Therefore, intensive efforts have been dedicated to developing higher-capacity anodes, a few of which are discussed below.

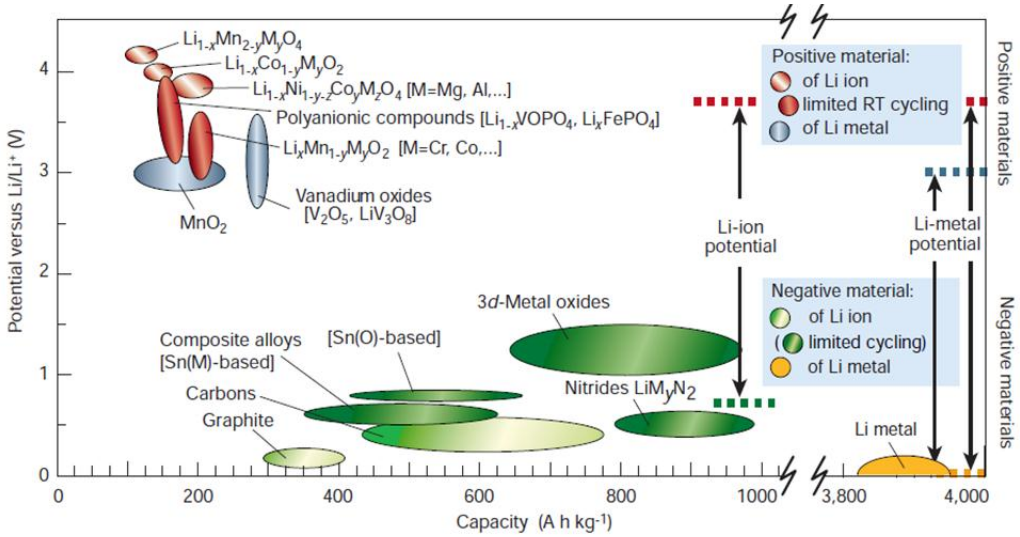

Figure 1.2: Voltage versus capacity for anode and cathode materials, either in current use or under development [40].

Metal oxides have been extensively investigated as potential anode materials for Li-ion rechargeable batteries due to their ability to provide high reversible capacities between 500 and 1000 mAh.g^{-1} [41, 42]. It should be noted that these oxide materials are classified according to their reaction mechanisms. For instance, SnO_2 has been considered the most significant reaction material of the Li-alloy. The lithium-alloy reaction mechanism is outlined in equations 1.3 and 1.4 below.

$$M_xO_y + 2yLi^+ + 2ye^- \rightleftharpoons xM + yLi_2O \quad (1.3)$$

$$M + zLi^+ + ye^- \rightleftharpoons Li_zMO_x \quad (1.4)$$

Despite the high theoretical capacity of SnO_2 (783 mAhg^{-1}), problems appear during continuous cycling, including rapid deterioration of the reversible capacity [43, 44, 45]. This capacity decay is attributed to aggregates formed by the delithiation of the Li-Sn alloy. Some developments have been made to enhance the cycling performance of SnO_2, such as the formation of porous nanostructures, nanocomposites and nanostructured thin films. Moreover, Nanostructured anatase TiO_2 has also attracted considerable interest due to its low voltage and display of fast Li insertion/extraction kinetics [46]. Unfortunately, TiO_2-based anodes generally offer low capacity compared to other developing technologies [47].

Both these oxide materials (SnO_2 and TiO_2) would currently provide lower overall cell voltages due to their discharge potentials, which are higher than those of graphite; this would

increase the safety and stability of the electrolyte but would ultimately result in reduced energy density. Consequently, to improve the energy densities of these oxide-based anode materials it would be necessary to connect them in a cell with a higher-voltage cathode material. In addition to these oxide-based anode materials, nanostructured silicon has also been widely championed as a potential anode material. Theoretically, the use of nanostructured silicon as a replacement anode for graphite could provide significantly higher capacity as well as comparable cell voltages to current materials.

1.5 Cathode Materials

The cathode material is currently the bottleneck for battery development because the current range of cathode materials generally offers much lower capacities than the corresponding anodes. From Figure 1.3, it is obvious that all cathode materials are located towards the left of the graph, which corresponds to low capacities [28]. The main goal of cathode research should be to find new materials which can uptake more significant amounts of active mass into smaller volumes. While at the same time keeping the overall safety and performance characteristics is required. The following text will provide a more detailed overview of the historical evolution of these materials (summarized in Figure 1.3), before presenting a selection of promising new materials which are currently under development.

In the quest to develop a fully functioning rechargeable (secondary) lithium battery, the first intercalation materials studied as potential cathodes were a series of dichalcogenides [47]. In the 1970s, dichalcogenides were found to offer good electrochemical performance. Among this series investigated, $LiTiS_2$ has been deemed the most attractive material for implementation as the cathode for LIBs. There were several reasons for the selection of $LiTiS_2$ as an intercalation host. Firstly, it was the lightest material [36]. Secondly, it showed semi-metallic behavior, so there was no need for a conductive coating [36]. Thirdly, lithium could be intercalated/deintercalated in a highly reversible way because no phase changes were observed during the cycle. In contrast to this last point, the more recent materials have a two-phase intercalation behavior leading to limited lithium extraction [11]. Although, heavier dichalcogenides offered many desirable properties as cathode materials for LIBs, research activity moved towards lighter oxides in the hope of finding suitable materials with increased energy densities [28].

Following the shift of focus from TiS_2, and the other dichalcogenides, the layered oxides of molybdenum (MoO_3) and vanadium (V_2O_5) were extensively studied as intercalation hosts. However, among these layered oxides, interest in MoO_3 was fleeting because of its reduced reactivity with lithium. In contrast, V_2O_5 was reported to react favorably with lithium with the intercalation of up to three Li ions per unit of V_2O_5 formula. Unfortunately, intercalation of Li ions above one per formula unit resulted in permanent structural changes, causing a phase that was able to cycle over all 3 Li ions but would rapidly lose capacity during the continuous charge/recharge cycles [48].

Following on from this, In the 1980s, layered oxides were extensively studied. For these layered oxide materials, significant variation was reported in the stacking of MO_2 layers; which was demonstrated to be related to lithium content. Therefore, the insertion/extraction of lithium resulted in structural changes.

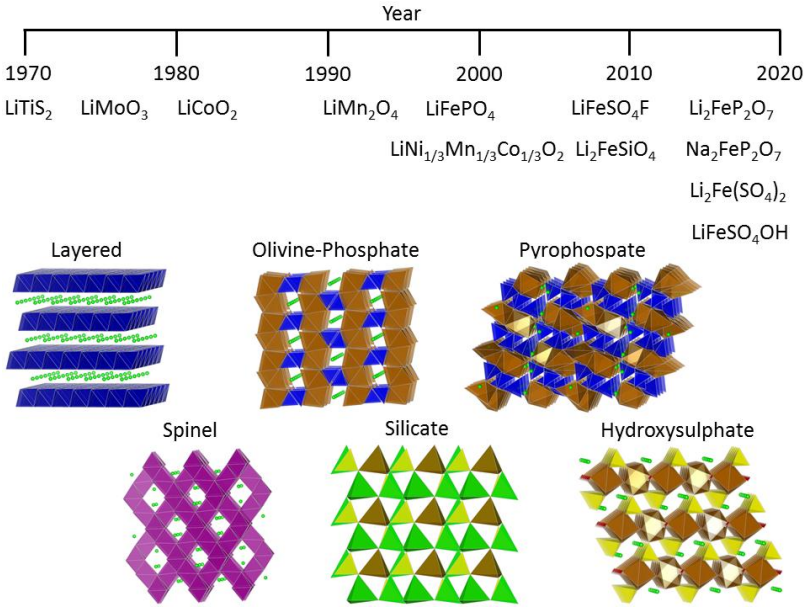

Figure 1.3: Timeline summarizing cathode development [49].

These structural changes during cycling reduced the electrochemical performance of these materials. Despite the above-mentioned problems with the $LiCoO_2$, which was first studied as a potential positive electrode material by Goodenough et al. [50] in 1980, it demonstrated its excellent characteristics as a positive electrode material [36].

In 1990, Sony released the first commercial rechargeable lithium-ion cell, which combined the $LiCoO_2$ cathode material with a graphite anode (shown in Figure 1.1) [51]. It was coined the "rocking chair" cell because lithium ions are shuttled back and forth between the

electrodes during cycling. The cell is constructed in the discharged state, so $LiCoO_2$ is the source of lithium ions. It provides a cell potential of about 4 V with a moderate cell capacity of 130 $mAh.g^{-1}$, which is about 50% of its theoretical capacity [36]. Delithiation greater than 50% results in phase changes which decrease reaction rates and cause capacity loss. In the highly charged state, which means at low lithium concentration, there are safety issues owing to the high concentration of Co^{4+}, which is highly oxidizing and tends to oxidize the electrolyte for reverting to a more stable 3+ state. The heat generated from this reaction, coupled with the volatility of the electrolyte presents a fire/explosion hazard; this is also a key mechanism through which cell capacity is lost [33]. Even though, $LiCoO_2$ has been widely commercialized as cathode material. Nevertheless, this cathode material contains a toxic and very expensive element, namely cobalt [27, 40]. Therefore, $LiCoO_2$ cannot meet the rigorous requirements for high-power applications in terms of cost, safety and environmental concerns. As a result, enormous efforts have been dedicated to finding inexpensive and high-performance viable cathode alternatives.

Since the inception of modern rechargeable lithium-ion batteries, three main cathode structures have dominated commercial lithium cells. These are $LiMO_2$ layered oxides, $LiMn_2O_4$ spinel and olivine $LFePO_4$ (LFP).

1.5.1 $LiMO_2$ Layered Oxides

$LiMO_2$ is the general form taken by the layered structures (where M = V, Cr, Mn, Fe, Co, Ni). The oxide ions adopt a cubic close-packed arrangement in which M ions occupy edge-sharing octahedral sites in alternate layers (shown in Figure 1.4); lithium ions reside in edge-sharing octahedral sites in the remaining layers. The structure has a distorted rhombohedral symmetry with space group $R\bar{3}m$. This layered structure allows for two-dimensional lithium diffusion within the layers of LiO_6 octahedra [33]. Although a significant amount of the research attention on the layered oxide family has been focused on $LiCoO_2$, other $LiMO_2$ (M = V, Cr, Mn, Fe, Ni) compounds have been investigated.

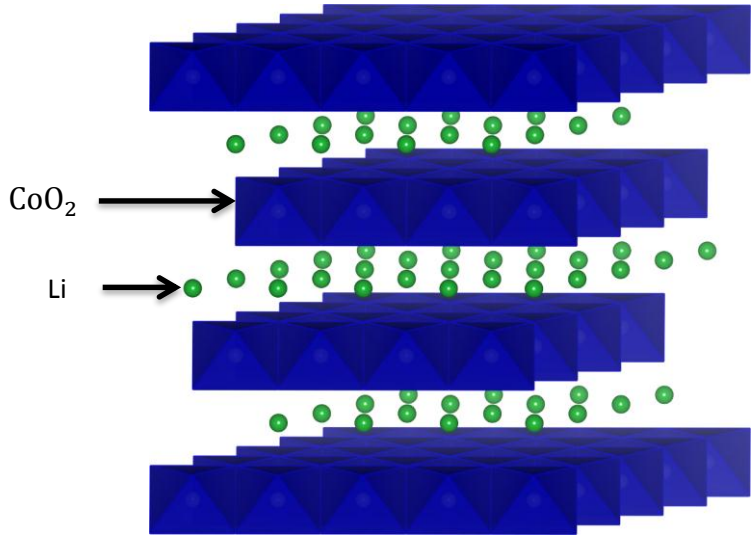

Figure 1.4: Layered structure of $LiCoO_2$ (green spheres: Li^+ ions; blue octahedral : CoO_6) [36].

$LiNiO_2$ has been considered as an alternative to $LiCoO_2$ because nickel is both less expensive and more readily available than cobalt [27]. It also can provide higher capacities. However, despite its series of advantages, it has not been implemented in a lithium-ion battery in its pure state because it is difficult to synthesize [48]. Likewise, $LiFeO_2$ has been proven to be an unsuitable alternative to $LiCoO_2$ due to its low operating voltage, although Fe is a cheaper and less toxic transition metal.

The improved stability of Mn^{4+} compared to Co^{4+} would make $LiMnO_2$ an attractive alternative to $LiCoO_2$. However, $LiMnO_2$ does not form a stable layered structure, instead during cycling, it is found to revert to the more stable spinel phase [33]. In this regard, solid solutions of Ni, Mn and Co, such as $LiNi_{0.4}Mn_{0.4}Co_{0.2}O_2$ and $LiNi_{1/3}Mn_{1/3}Co_{1/3}O_2$, have been used in commercial cells, replacing $LiCoO_2$. Within these solid solutions, Ni is used as the electrochemically redox active species, Mn ensures better structural stability, whereas Co prevents further migration of Ni into the Li sites. Nevertheless, small amounts of Ni are needed in the lithium layer to avoid structural changes during delithiation [52]. These phase changes would potentially reduce the performance of the cathode, so the Co content is adjusted accordingly [47]. However, it is worth noting that the optimal solid solution composition is yet to be determined since all variants exhibit low electrical conductivity [48].

1.5.2 $LiMn_2O_4$ Spinel

The spinel structure has space group $Fd\bar{3}m$ consisting of cubic close-packed oxide ions with Mn ions in half of the octahedral sites and Li ions in an eighth of the tetrahedral sites (Figure

1.5). The Mn_2O_4 framework offers a series of tunnels that intersect in all three dimensions, thereby facilitating the fast migration of lithium. Another advantage of the spinel structure, not available in comparative layered structures, is its high structural rigidity, which makes its tunnels more selective to the small Li+ ions [33]. $LiMn_2O_4$ was firstly revealed in 1983 [53], and by 1996 it was used, by Nipon Moli in Japan, in the first commercial lithium battery as an alternative to $LiCoO_2$ cathode material. The main motivations for the change of cathode were the manganese advantages such as its environmentally benign, greater abundance, and reduced cost compared to cobalt (manganese costs ~1% of cobalt).

The spinel framework enables the intercalation of lithium until reaching the maximum $Li_2Mn_2O_4$ composition. Within $Li_xMn_2O_4$ the intercalation of lithium is reported to occur at two different potentials, one at 4 V where $0 < x < 1$, with lithium inserted into the tetrahedral sites, and the other at 3 V where $1 < x < 2$, with lithium inserted into the octahedral sites. The redox couple in both cases is Mn^{3+}/Mn^{4+}, so the voltage difference may be related to the energy difference between the tetrahedral and octahedral sites. Li-ion batteries are not very interested in the 3V process but could be important for Li-metal batteries if cycling problems can be resolved [54, 55].

The main shortcoming of this material is the structural changes that occur upon lithium insertion, which is due to the increase in the concentration of Jahn-Teller active high spin Mn^{3+} species. These structural changes that occur during cycling can have pronounced effects on the volume of the material, with changes of up to 6%, resulting in a loss of contact between $Li_xMn_2O_4$ particles. The storage capacity of these isolated particles is reduced, leading to an overall loss of cell capacity. The formation of solid solutions by substituting small amounts of Mn with other metals (Li, Ga, Ni, Cu, Be, Co, Cr, Zn, Mg) has been used as a method to protect against such effects by improving structural stability. One of these solid solutions, $LiMn_{1.5}Ni_{0.5}O_4$ has attracted significant attention for high-power applications such as hybrid electric vehicles due to its high operating voltage of 4.7 V, reasonable cycle stability and high rate capability [33, 55]. However, this material still suffers from gradual structural degradation during cycling. Therefore, many researchers have focused on further enhancing the structural integrity of the spinel by substituting small amounts of Mn with Mg to form solid solutions with compositions such as $LiMg_{0.05}Mn_{1.5}Ni_{0.45}O_4$. Even though the vital role of these measures, the substitution of Mn by any redox inactive species will automatically result in a reduction of the cell capacity [48].

Interest in the spinel structure has focused on its potential for use in a high-power lithium-ion battery for hybrid electric vehicles (HEVs). Unfortunately, it has been found that the spinel capacity drops to ~80 $mA.g^{-1}$ under high drain rates. Although the spinel is still considered for application within HEVs, the material has had additional issues with self-discharge when it is left fully charged. This problem seems to be especially apparent with increasing temperatures. However, since the principal cause of this capacity loss is thought to be the presence of the acidic HF, which is generated by the fluoride-containing $LiPF_6$ salt and trace amounts of moisture, a solution to this problem could be to change the salt to LiBOB [49].

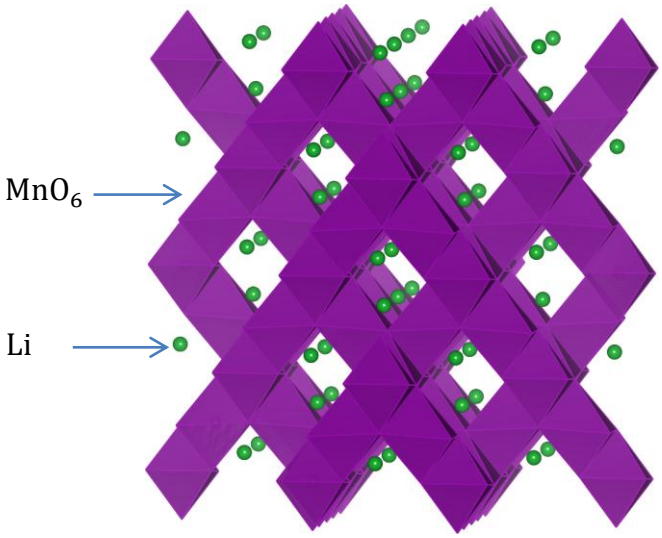

Figure 1.5: $LiMn_2O_4$ spinel oxide structure composed of LiO_4 tetrahedra and MnO_6 octahedra in a three dimensional lattice [49].

1.5.3 $LiMPO_4$ Olivine Phosphates

1.5.3.1 Phosphate ($LiMPO_4$; M = Fe, Mn, and Ni)

Olivine structure ($LiMPO_4$; M = Fe, Mn, and Ni) has an orthorhombic unit cell that accommodates four formula units of $LiMPO_4$with a symmetry group Pnma (number 62) [56]. Figure 1.6 presents the schematic of the olivine structure $LMPO_4$ which is a hexagonal close-packed array of oxygen atoms. Where Li and M ions are located in half of the octahedral sites and P ions occupy one-eighth of the tetrahedral positions. In this structure, a PO_4 tetrahedron shares an edge and two corners with MO_6 (M = Fe, Mn, and Ni) octahedrons which consist of layers in the bc plane. This construction creates channels along the [010] direction which is allowed to store and diffuse Li-ions [57]. Furthermore, diffusion of Li-ions in olivine structure

is well known to occur along the [010] direction because of the absence of continuous LiO_6 octahedra along the a and c axis directions [58].

Since its discovery in 1997, the olivine LFP has appeared in the energy storage world as an effective cathode material for LIBs due to its outstanding advantages such as high cycling performance, nontoxicity, environmental protection, high theoretical capacity (170 $mAhg^{-1}$) with 97–98% of retention over 1000 cycles [59], low price and high thermal safety (LFP has been shown to be stable up to 400°C) [10, 60]. Another characteristic of LFP is a flat voltage profile of about 3.4 V versus Li/Li^+ which is caused by lithiated and delithiated phases [34, 61]. Moreover, the unit cell volume variation between these boundary phases (lithiated and delithiated phases) is only 6.8% and their density difference is only 2.6% confirming a small difference in their crystal structures [34].

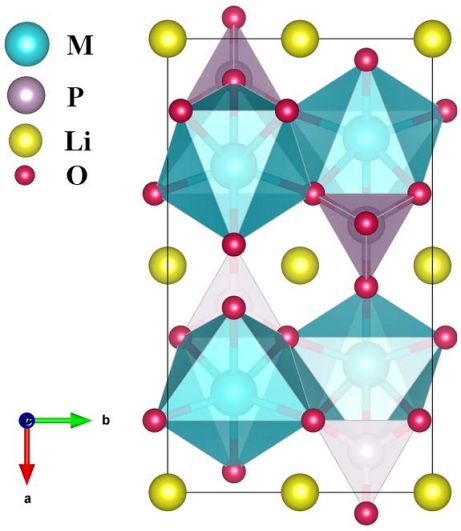

Figure 1.6: The olivine structure $LMPO_4$.

This suggests also that the delithiated phase $FePO_4$ has good structural stability, which contributes to the remarkable cycling stability of LFP. Interestingly, this similarity between LFP and FP helps in preventing capacity degradation resulting from severe volume changes in cathodes during the charge/discharge process. In order to understand the electronic properties of LFP cathode material, the band gap and the total and partial density of states (TDOS, PDOS) have been investigated by several density functional theory (DFT) studies [27, 62, 63]. From these findings, it was concluded that LFP has a semiconductor behavior with a band gap value ranging from 3.4 to 3.7 eV. This slight difference can be ascribed to the values of the Hubbard parameters (U) or the different functional or calculation methodologies. Based on the partial density of states, the valence band of LFP has been found to be mainly

composed by Fe-3d, Li-2s and O-2p orbitals whereas the conduction band is mainly formed by spin-down of the Fe-3d orbitals [23, 64].

In addition to electronic properties, kinetic properties are also the crucial factor defining the performance of LIBs. It's worth noting that both theoretical and experimental results suggest that Li migration in olivine structures is located along the b-axis, as shown in Figure 1.7 [65, 66]. The diffusion coefficient (D) of Li^+ ions in LMP has been evaluated by a variety of experimental techniques such as galvanostatic intermittent titration technique, electrochemical impedance spectroscopy, systematic cyclic voltammetry, and theoretical methods including DFT by nudged elastic band (NEB) [60-68]. As previously reported by several studies, the D values of LFP are in the range 10^{-13}-10^{-14} cm^2s^{-1} [58].It is clear from diffusion coefficient and band gap values that despite the outstanding advantages of LFP, it still has poor electric and ionic conductivity. Therefore, decreasing the diffusion path of Li-ion ions and reducing the distance that electrons require to travel through the active material are very important to improve LFP performance. In this context, various strategies have been used to get rid of the LFP shortcomings such as tuning morphology, reducing its particle size, coating LFP with nanostructured carbon, single-element doping (Li sites or Fe sites or O sites) and co-doping; which can be split into two types; one is doping with identical elements in the same site and the other is doping with different elements in different sites [69, 70]. Generally, all these techniques have demonstrated their decisive role in improving LFP performance, for instance, carbon coating can increase LFP capacity up to 165 $mAhg^{-1}$ (97 % of the theoretical capacity) and improve the charging and discharging properties at high currents.

On the other side, the performance of active materials in LIBs is strongly related to their synthesis methods. In this regard, several methods have been implemented including the solid-state reaction method which is a traditional one for LFP synthesis, and solution chemistry methods such as the spray pyrolysis method [71], sol-gel method [72], precipitation [73], hydrothermal method, solvothermal [48] and polyol synthesis [73] which have attracted much attention due to their benefits. Consequently, iron phosphate LFP has become one of the leading commercial cathode materials for lithium batteries, due to extensive efforts by several research groups around the world.

Nevertheless, LFP still suffers from a low operating voltage (~3.4 V vs Li/Li^+) resulting in a low energy density that does not meet the current requirements of high energy devices.

Therefore, several researchers have focused on developing other members of olivine family, such as $LMnPO_4$ (LMP), $LiNiPO_4$ (LNP) and $LiCoPO_4$ (LCP).

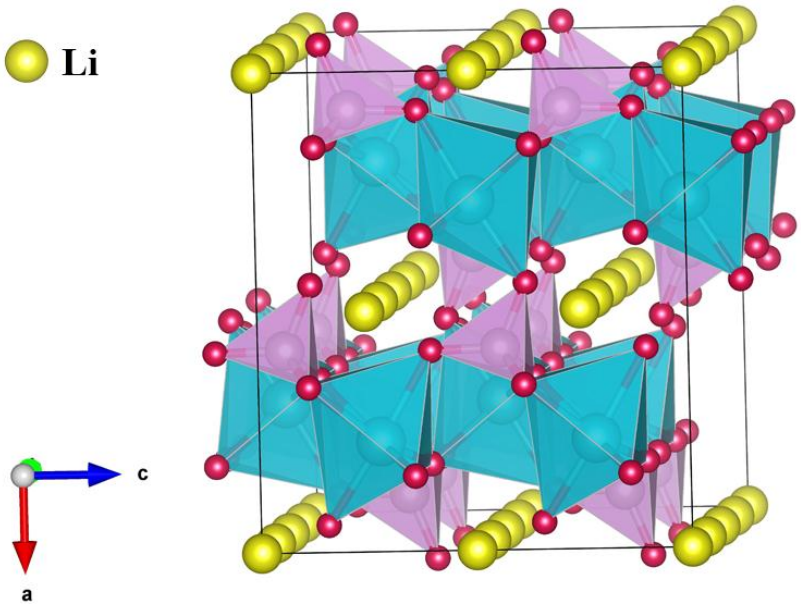

Figure 1.7: Migration paths of lithium-ion in olivine structure.

Lithium manganese phosphate (LMP) has attracted significant attention due to its charismatic properties such as good stability, identical theoretical capacity to LFP, environmental friendliness, and inexpensive cost. Moreover, LMP offers a higher voltage (4.1 V vs. Li/Li^+) than LFP (3.45 V versus Li/Li^+) and is compatible with current electrolyte windows. It can also deliver a higher theoretical energy density of 700 $Whkg^{-1}$ with good safety owing to the presence of a strong P–O covalent bond, which suggests that LMP is a promising cathode material for LIBs. However, LMP also suffers from some factors which limit its electrochemical performance such as low electronic ($<10^{-9}$ Scm^{-1}) and ionic ($<10^{-16}$- 10^{-14} cm^2s^{-1}) conductivities, higher polaron migration compared to LFP, Meta-stable nature of its delithiated phase [12]. To overcome these drawbacks, three main strategies have been explored: particle size reduction to reduce the Li-diffusion length thereby enhancing ionic conductivity of LMP, carbon coating to improve its electric conductivity and prevent surface degradation, and mixing of olivine (single element doping or co-doping in Mn sites by different transition metal such as Fe, Ni, Mg, Zn, Ti and Co, etc.). Current researches of phosphate-based cathode materials have considered the latter strategy as one of the effective solutions to improve the electrochemical performance of olivine-based cathode materials. In Section 1.3, we will see how this strategy can improve the performance of cathode materials.

Concerning LNP and LCP, these olivine materials are presently excluded due to their high voltage of 4.8 and 5.2 V, respectively. These voltages exceed the electrochemical stability window of most current commercial liquid electrolytes (4.5 V [14]). Unfortunately, LIBs haven't benefited yet from these cathode materials which can offer a high energy density thereby being used in high-energy devices (HEV, EV). In this regard, we crucially need to design new electrolytes that could withstand high voltages, with electrolytes stable at least up to 5.2 V as an example. But, in contrast to LFP, heavy metal ions pose a health hazard, especially cobalt.

1.5.3.2 Mixed Transition Metals in Olivine Materials

As mentioned above, the main drawbacks of olivine materials are their low intrinsic electronic and ionic conductivity. Therefore, many methods and different synthesis techniques have been used to get rid of these constraints. Accordingly, single doping and co-doping strategies are one of the most successful methods to improve the performance of olivine-based cathode materials for LIBs. For instance, using DFT, Oukahou et al [23]. examined the effect of Ni/Fe single-doping on the structural, electronic, kinetic, electrochemical potential and magnetic properties of LMP. They revealed that Ni/Fe single-doping can enhance the performance of pristine LMP. For example, the open-circuit voltage of virgin LMP is slightly increased from 4.39 to 4.41 V for $LiMn_{0.25}Ni_{0.75}PO_4$ which indicates the improvement in energy density of LMP. Furthermore, the substitution of Mn sites by Ni and Fe leads to a good enhancement in the electronic conductivity, where the band gap of pristine LMP (3.62 eV) is reduced with substitution by 50% of Ni (2.77 eV) and 50% of Fe (3.35 eV). Moreover, the barrier energy is decreased from 0.42 eV for pure $MnPO_4$ to 0.34 and 0.39 for $Mn_{0.5}Ni_{0.5}PO_4$ and $Mn_{0.5}Fe_{0.5}PO_4$ respectively, indicating that 50% of Ni or Fe is beneficial to enhance the ionic conductivity of pristine $MnPO_4$ [23].In this context, Zhang et al. investigated the influence of different elements doping on the electrochemical properties of LMP using first principle methods. They found that Ni, Fe, Nb, Ti, V doping at Mn in LMP can moderate the John-Teller, thereby improving the structural stability of pristine LMP. They also concluded that Fe is the most effective dopant element compared to others (Mg, Ni, V, Nb and Ti) because it can promote electronic conductivity and thermal stability, as well as reduce the barrier energy to boost the Li-ion diffusion [12]. Sukkabot studied the effect of transition-metal doping on the structural and electronic properties of LMP. He reported, using DFT+U method, that the LMP doped by Cr exhibits a volume expansion whereas the other transition metal (Co, Cu, Fe and Ni) demonstrate a volume compression because the ionic radius of Cr is greater than that

of Mn, while the ionic radius of other metals transitions is smaller than that of Mn. He also indicated the appearance of impurity at the edges of the conduction bands, which reduced the band gap and improved the electronic conductivity of pure LMP. Finally, he concluded that $LiMn_{3/4}Cr_{1/4}PO_4$ compound is a promising cathode material compared to other compounds ($LiMn_{3/4}Co_{1/4}PO_4$, $LiMn_{3/4}Cu_{1/4}PO_4$, $LiMn_{3/4}Fe_{1/4}PO_4$ and $LiMn_{3/4}Ni_{1/4}PO_4$) due to its volume expansion, narrow band gap and high Li insertion potential [74]. In addition, Gao et al. have studied the effect of Ru doping in Fe sites of LFP. They discovered, using DFT method, experiments and characterization, that Ru doping leads to a remarkable enhancement in the electrochemical performance of pristine LFP. For example, an improvement of electrical conductivity by reducing the band gap and the Li-ion diffusion coefficient by shortening the Li-ion migration length [75]. Subsequently, they have also reported that the $LiFe_{1-x}Ru_xPO_4/C$ (x = 0.01) (LFP-1) exhibits a higher discharge capacity at the first charge-discharge compared to pristine LFP/C. The LFP-1 provides excellent specific capacities of 162.6 and 110.6 $mAhg^{-1}$ at 0.1 and 10 C indicating the key role of Ru in reducing the polarization and delivering superior electrochemical reversibility of electrode. In this context, Cui et al. have conducted research on the effect of Co, Mn and S doping element on the performance of LFP cathode material using DFT calculations [76]. They found that doping plays a crucial role in enhancing electrochemical performance. For example, the stability of pristine LFP after adding doping elements has not been demolished and the diffusion of Lithium-ion was reduced from 1.02 to 0.57 eV, indicating the enhancement of ionic conductivity. The transition from p-type to n-type semiconductor characteristics occurred by S doping. They also reported that the band gap was reduced from 3.78 to 0.74 eV which suggests an improvement in electronic conductivity and the operating voltage of LFP was increased to 4.76 V, demonstrating a high energy density.

Besides the theoretical studies, wang et al. synthesized $LiFe_{1-x}Mn_xPO_4/C$ (x = 0, 0.2, 0.5) composite materials by the solid-phase method. They reported that $LiFe_{0.5}Mn_{0.5}PO_4$ exhibits good dispersibility and consistent particle morphology, resulting in excellent Li-ion diffusion and high electrical conductivity, good rate performance, as well as high energy density compared to commercial LFP [77]. On the other hand, El‑Khalfaouy et al. studied the effect of substitution Mn sites with different amounts of cobalt, i.e., $LiMn_{1-x}Co_xPO_4@C$ (x = 0.0, 0.01, 0.05, 0.15 and 0.25). They proved using a modified solution combustion method (SC) using glycine as a fuel source, and starch as an additional carbon source, that the $LiMn_{0.99}Co_{0.01}PO_4/C$ compound exhibits the highest initial discharge capacity of 157 $mAhg^{-1}$

at C/20 with a coulomb efficiency of about 98.1% which is higher than that of pristine LMP (80.38%) [78]. Subsequently, they have also reported that even after 30 cycles this cathode can recover a capacity of 151 $mAhg^{-1}$ with remarkable efficiency of about 96% compared to the initial value, which proves the excellent structural stability of this compound. Finally, this study concluded that an optimal amount of Mn substitution by Co in LMP can improve the electrochemical performance in terms of stabilizing the structure during intercalation and deintercalation of Li and enhancing the diffusion coefficient of Li-ion through the structure.

More recently, Co-doping has proven to be more effective than single-element doping at improving the poor rate performance of olivine-based cathode materials. In this regard, Ramar et al. investigated the influence of Fe/Mg single doping and Fe and Mg co-doping in LMP. They synthesized $LiMn_{0.9}Fe_{(0.1-x)}Mg_xPO_4/C$ via a ball mill-assisted soft template method. They discovered that Fe and Mg isovalent co-doped $LiMn_{0.9}Fe_{0.05}Mg_{0.05}PO_4/C$ exhibits excellent electrochemical performance compared to Fe/Mg single doped material ($LiMn_{0.9}Fe_{0.1}PO_4/C$ and $LiMn_{0.95}Mg_{0.05}PO_4/C$). For instance, $LiMn_{0.9}Fe_{(0.1-x)}Mg_xPO_4/C$ has a storage capacity of 159 $mAhg^{-1}$ at 0.1C with low polarization of ~139 mV while the $LiMn_{0.9}Fe_{0.1}PO_4/C$ and $LiMn_{0.95}Mg_{0.05}PO_4/C$ exhibit only 136.8 and 128.4 $mAhg^{-1}$at 0.1 C with the polarization of ~ 222 and 334 mV, respectively. In addition, the Fe and Mg co-doped cathode material can preserve a capacity of 116 $mAhg^{-1}$ at 1 C after 200 cycles and its capacity retention rate is 96%, furthermore, this study reported that Fe^{2+} and Mg^{2+} co-doping improves the electronic and ionic conductivity of LMP compared to Mg or Fe single doping. Libin et al. have demonstrated, using first principle calculations and simple high-temperature solid stated methods, that Zr and Co co-doping can be a successful strategy to enhance the electrochemical properties of virginal LFP. Such as, the Zr-Co co-doping improves the structural stability of pristine LFP, lowers the band gap indicating an improvement of electronic conductivity, and lengthens the Li-O bond which would facilitate the diffusion of Li-ion along the b axis in LFP thereby enhancing the ionic conductivity of LFP. Furthermore, they revealed that $Li_{0.99}Zr_{0.0025}Fe_{0.99}Co_{0.01}PO_4$ has an initial discharge-specific capacity of 139.9 $mAhg^{-1}$ at 0.1 C and a capacity retention rate after 50 cycles of 85%. Hence, they have concluded that a suitable amount of Zr-Co co-doping can be an efficient method to ameliorate the electrochemical performance of LFP as cathode material for LIBs [79]. In addition, Huihua et al. synthesized $LiMn_{0.9}Fe_{0.1-x}Zn_xPO_4/C$ (x=0, 0.05, and 0.1) composites by a solid-state process in order to study the effect of Fe and/or Zn doping on the performance of LMP. They reported that the Fe-Zn co-doped $LiMn_{0.9}(FeZn)_{0.05}PO_4/C$ show a better discharge

capacity and excellent rate capability compared to Fe/Zn single doped material. So that, it offers the capacities of 151.3 $mAhg^{-1}$ at 0.1 C and 128.4 $mAhg^{-1}$ at 1 C and retains 96.7 % of the initial capacity after 100 cycles [80]. From the above-mentioned studies, mixed transition metals in olivine materials (single doping or co-doping) is suggested as a successful method to enhance the electrochemical performance of olivine materials and thus overcome their disadvantages, namely low electronic and ionic conductivity.

1.5.4 Comparison of cathode materials

In LIBs, the suitable cathode material must meet some requirements such as high storage capacity, high working voltage, structural stability, high energy density, good conductivity and porosity, safety, environmentally benign as well as low cost to make the batteries affordable. For this purpose, this section lists some characteristics of olivine and other common commercial cathode materials (See Table1.1).

Table 1.1: Comparison of common cathode materials in LIBs.

Material structure	Composition	Theoretical Capacity [$mAhg^{-1}$]	Capacity at 0.1C [$mAhg^{-1}$] (voltage range)	Operating Voltage versus Li^+/Li [V]	Specific energy [$Wh\ Kg^{-1}$]	Cost	Refs
Layered	**$LiCoO_2$**	**274**	**185 (3.0-4.45 V)**	**3.9**	**720**	**High**	[81]
	$LiNi_{1/3}Co_{1/3}Mn_{1/3}O_2$	**278**	**160 (2.8-4.3 V)**	**3.8**	**610**	**Medium**	[82]
	$LiNi_{0.8}Co_{0.1}Mn_{0.1}O_2$	**276**	**205 (2.8-4.3 V)**	**3.8**	**780**	**Medium**	[83]
	$LiNi_{0.8}Co_{0.15}Al_{0.05}O_2$	**279**	**200 (2.8-4.3 V)**	**3.8**	**760**	**Medium**	[84]
Spinel	**$LiMn_2O_4$**	**148**	**120 (3.0-4.3 V)**	**4.1**	**490**	**Low**	[85]
Olivine	**$LiFePO_4$**	**170**	**150 (2.5-4.2 V)**	**3.4**	**510**	**Low**	[86]
	$LiMn_{0.8}Fe_{0.2}PO_4$	**171**	**160 (2.5-4.2 V)**	**4.1**	**650**	**Low**	[87]
	$LiMnPO_4$	**171**	**148.9 (2.5-4.5 V)**	**4.13**	**697**	**low**	[88]
	$LiCoPO_4$	**167**	**164**	**-**	**787**	**low**	[89]
	$LiCo_{0.8}Fe_{0.2}PO_4$	**-**	**105**	**4.8**	**-**	**Low**	[90]
	$LiNi_{0.5}Co_{0.4}\ Al_{0.01}PO_4$	**-**	**46.1 (2.25-4.8 V)**	**4.8**	**-**	**-**	[91]

As reported by several studies (see Table 1), the layered oxide material $LiCoO_2$ and its doped

derivatives ($LiNi_xCo_yAl_{1-x-y}O_2$, NCA and $LiNi_xMn_yCo_zO_2$, NMC) are widely consumed cathodes in LIBs due to their high energy density reaching 780 $WhKg^{-1}$ which is explained by the redox properties of Mn, Ni, and Co ions as well as by the good working voltage reaching 3.9V. In addition, $LiCoO_2$ has a high theoretical capacity of 274 $mAhg^{-1}$ but this material does not take advantage of the full capacity and only provides half of it due to the inability to extract all the lithium during the charging process [59]. Nevertheless, they face a number of challenges such as high cost, safety issues, and environmental concerns, especially pristine $LiCoO_2$ due to the presence of cobalt element. Besides the layered oxide material, spinel $LiMn_2O_4$ is another available cathode material which has low cost, abundance and non-toxicity. As it can be observed from Table 1, spinel has low performance compared to layered oxides and olivine cathode materials in terms of operating voltage and specific energy, as well as it suffers from capacity degradation during the charge/discharge processes.

In general, oxides suffer from instability at high temperatures. These materials can be decomposed at a low temperature and release O_2, resulting in a fire or even an explosion of the battery. In contrast, phosphate-based cathode materials have high thermal stability owing to their olivine structures. For instance, LFP has been shown to be stable up to 400°C [10, 72]. In addition, LFP can be more quickly charged/discharged than other commercial cathode materials even though it has only one dimensional Li-ion diffusion channel compared to layered oxide and spinel cathode materials that have two or even three dimensional Li-ion diffusion. Furthermore, the LFP is the cheapest cathode material due to the presence of iron which is the second most abundant element on earth. However, LFP has a low working voltage (3.4 V) and low specific energy (510 $WhKg^{-1}$) compared to layered oxide cathode materials (see Table 1). But recently, these values have improved to some extent with the substitution of Fe sites with manganese amounts (LMFP). For example, $LiMn_{0.8}Fe_{0.2}PO_4$ is superior to LFP in terms of working voltage (4.1 V), specific energy (650 $WhKg^{-1}$) as well as capacity (160 $mAhg^{-1}$at 0.1C). Therefore, phosphate-based cathode materials are promising cathode materials for the next generation of Li-ion batteries.

1.6 Objectives of this thesis

As mentioned above, LMP is one of the most promising olivine cathode materials for Li-ion batteries due to its charismatic properties. However, LMP suffers from certain factors which reduce its efficiency as cathode material such as low electronic and ionic conductivities as well as the metastable nature of its delithiated phase. Therefore, the main objective of this

thesis was to overcome these drawbacks of LMP through single doping, co-doping, and biaxial strain strategies using density functional theory (DFT).

The present thesis pursued the following objectives:

-Investigate the effect of Ni-Fe single-doping on the geometry, electronic, electrochemical potential and kinetic properties of lithiated /delithiated pristine phases of LMP using first-principles calculations.

-Examine the effect of Ni–Fe co-doping on the structural, electronic, magnetic, electrochemical potential and kinetic properties of lithiated/delithiated pristine phases (i.e. $LiMn_{0.5}Ni_{0.25}Fe_{0.25}PO_4$/ $Mn_{0.5}Ni_{0.25}Fe_{0.25}PO_4$), as well as the thermodynamic stability, theoretical capacity, charge transfer, average M-O bond lengths and electrical conductivity based on DFT calculations.

- Investigate the biaxial strain effects on the structural, electronic properties, thermal and dynamic stability, intercalation voltage, charge transfer, and kinetic properties of both pristine and defect $LiMnPO_4$, based on DFT calculations.

Chapter 2

Computational Methods

2.1 Introduction

In quantum theory, the wave function contains all the information about a specific system. To obtain this wave function, the Schrödinger equation has to be solved. However, it is not possible to solve this equation exactly for multi-electron systems. In a solid-state system, the number of electrons involved in the reactions is usually large, and effective approaches are required. DFT focuses on the electron density and is therefore an efficient method to solve the multi-electron problem and to find the ground state energy [92].

In this chapter, we will give a brief review on this theory. Readers who want a deeper understanding of DFT concepts should refer to textbooks on quantum mechanics such as [93]. The chapter begins with a brief discussion of the Schrodinger equation and the Born-Oppenheimer approximation. Afterward, the Hohenberg and Kohn theorems and the Kohn-Sham equations are briefly reviewed, as well as exchange-correlation functionals, Plane waves, Pseudopotentials and Software used. Finally, I will define the method that was performed to locate the transition state and extract the Li-ion migration barrier, which is the Nudged Elastic Band.

2.2 Quantum Theory

Quantum mechanical methods seek to solve the many-body Schrödinger equation to calculate the electronic structure of a system. Equation 2.1 shows the time-independent form of the Schrödinger equation:

$$\widehat{H}\ \Psi(R, r_i) = E\Psi, \tag{2.1}$$

where $\widehat{\mathbf{H}}$ is the total Hamiltonian of the studied quantum system, $\mathbf{\Psi}$ is the wave function that contains all the information about the system state, r and R represent the coordinate vector of all *n* electron and *N* nuclei, respectively, and **E** is the total energy for the system.

More precisely, the Hamiltonian can be written as follows:

$$\widehat{H_T} = \widehat{T_n} + \widehat{T_e} + \hat{V}_{n-e} + \hat{V}_{e-e} + \hat{V}_{n-n} \tag{2.2}$$

Where $\widehat{\mathbf{T_n}}$ is the kinetic energy of nuclei, $\widehat{\mathbf{T_e}}$ is the kinetic energy of electrons, $\hat{\mathbf{V}}_{\mathbf{e-e}}$ is the Coulomb interactions between electrons, $\hat{\mathbf{V}}_{\mathbf{n-n}}$ is the Coulomb interactions between nuclei, and $\hat{\mathbf{V}}_{\mathbf{n-e}}$ is the Coulomb interactions between electrons and nuclei that is considered as an external potential. In DFT, the external potential is not necessarily restricted to the effect of the nuclear field on the electrons but may include external magnetic and/or electric fields. Throughout this thesis, we use atomic units for all equations, that is, $\frac{1}{4\pi\mathcal{E}} \cong m_e \cong \hbar \cong 1$.

The terms of the equation are expressed as follows:

$$T_e = -\frac{1}{2}\sum_{i=1}^{N} \nabla^2$$

$$T_N = -\frac{1}{2}\sum_{i=1}^{M} \frac{\nabla^2}{M_i}$$

$$V_{e-e} = \sum_{i=1}^{N}\sum_{j>i}^{N} \frac{1}{|r_i - r_j|}$$

$$V_{e-N} = -\sum_{i=1}^{N}\sum_{j=1}^{M} \frac{Z_j}{|r_i - R_j|}$$

$$V_{N-N} = \sum_{i=1}^{M}\sum_{j>i}^{M} \frac{Z_i Z_j}{|R_i - R_j|}$$

Where $\mathbf{Z_i}$ and $\mathbf{Z_j}$ are the charges of nuclei *i* and *j*, respectively.

In these conditions, the Schrödinger equation (2.1) becomes:

$$\left[-\frac{1}{2}\sum_{\mathrm{i=1}}^{\mathrm{N}} \nabla^2 + \sum_{\mathrm{i=1}}^{\mathrm{N}}\sum_{\mathrm{j>i}}^{\mathrm{N}} \frac{1}{|\mathrm{r_i} - \mathrm{r_j}|} - \sum_{\mathrm{i=1}}^{\mathrm{N}}\sum_{\mathrm{j=1}}^{\mathrm{M}} \frac{\mathrm{Z_j}}{|\mathrm{r_i} - \mathrm{R_j}|} + \sum_{\mathrm{i=1}}^{\mathrm{M}}\sum_{\mathrm{j>i}}^{\mathrm{M}} \frac{\mathrm{Z_i Z_j}}{|\mathrm{R_i} - \mathrm{R_j}|} - \frac{1}{2}\sum_{\mathrm{i=1}}^{\mathrm{M}} \frac{\nabla^2}{\mathrm{M_i}}\right] \psi(\mathrm{r_1}, \dots, \mathrm{r_N}, \mathrm{R_1}, \dots, \mathrm{R_M}) = \mathrm{E}\psi(\mathrm{r_1}, \dots, \mathrm{r_N}, \mathrm{R_1}, \dots, \mathrm{R_M}) \tag{2.3}$$

The exact solution of Schrödinger's equation (2.3) is only possible for simple systems, such as an isolated hydrogen atom. In all other cases, approximations must be used to approach the exact solution of this equation.

2.3 Born-Oppenheimer approximation

The first approximation used to solve Schrödinger's equation (2.3) is the Born-Oppenheimer approximation [94]. This approximation assumes the nuclear and electron motions to be decoupled, which enables the electrons to move about a fixed nuclear configuration. It is well-known that the electronic mass is significantly smaller than that of the nuclei (Mn=1836Me). As a consequence, the electrons respond almost instantaneously to changes in the positions of the nuclei. Such an approximation has two significant implications for the Hamiltonian. Because the nuclei are fixed, their kinetic energy is zero and the potential energy due to nucleus-nucleus interactions become constant. Therefore, the problem goes from a complexity with n electrons + N nuclei to a complexity with n electrons. The Hamiltonian given in equation (2.2) is reduced to the so-called electronic Hamiltonian.

$$\hat{H}_{elec} = \hat{T}_e + \hat{V}_{n-e} + \hat{V}_{e-e} + C^{ste} \tag{2.4}$$

The solution of the Schrodinger equation with $\hat{\mathbf{H}}_{\mathbf{elec}}$ gives the electronic wave function, $\boldsymbol{\Psi}_{\boldsymbol{elec}}$ and the electronic energy, E_{elec}. It is worth noting that $\boldsymbol{\Psi}_{\boldsymbol{elec}}$ depends on the electron's coordinates, whereas the nuclear's coordinates enter only parametrically. The total energy, E_{tot}, of the whole system (electrons + nuclei) is a sum of an electronic term, E_{elec} and a constant nuclear term, E_{nucl}, given by:

$$E_{tot} = (E_{elec} + E_{nucl}) \tag{2.5}$$

Despite this significant simplification, the resolution of the Schrodinger equation remains very difficult because of the complexity of electronic motions and interactions that govern it.

2.4 Density functional theory (DFT)

Density Functional Theory (DFT) is a first principle electronic structure technique used to investigate and probe the structure-property relationships of many-electron systems. It allows insights into various ground-state properties which empirical methods do not provide, such as band structure, charge distribution, orbital occupancies and bonding.

The development of DFT dates back to 1927 when Thomas and Fermi first suggested that the

total energy of a system could be approximated by a function of the electron density, including the kinetic energy. Even though they did not include the exchange and correlation term, Dirac extended the theory by treating the exchange term as a function of the density. The electron density is equal to the local density at any given point as in a homogeneous electron gas, and the total energy is integral over space. Because of the tremendously simple form of the approximation, it neglects some physics such as shell structures and binding within matter. However, their work is regarded as a precursor for the development of modern DFT.

2.4.1 Hohenberg and Kohn theorems

The Hohenberg-Kohn theorems provide a viable framework for calculating a wave function and constitute the elementary principles of DFT [95]. The two theorems are defined as follows [96]:

Theorem I: The three-dimensional electron density of a many-electron system uniquely determines all the ground state properties of the system.

Theorem II: The energy of a system can be defined as a functional of the electron density, with the minimum of the energy functional corresponding to the ground-state electron density.

The first theorem means that solutions for the *n*-electron wave-function $\Psi(\mathrm{r})$ are no longer required. All that is needed is the much simpler knowledge of the three-dimensional electron density $\rho(\mathrm{r})$. The second theorem stipulates that by defining the energy function of the system, the electron density of the ground state of the system can be calculated. This defines all other properties of the system. Hohenberg and Kohn defined the energy functional which encompasses much of the complexity of the original problem according to Equation 2.6.

$$E[\rho(r)] = \int V_{ext}(r)\rho(r)dr + F_{HK}[\rho(r)] \tag{2.6}$$

The first term describes the interactions between electrons and the external potential, including nuclear interactions. The second term ($\mathrm{F}_{HK}[\rho(\mathrm{r})]$), contains the kinetic information of the electrons in the system, as well as terms resulting from electron-electron interactions.

While Hohenberg-Kohn theorems supply a simplified model for the calculation of the many-electron Schrödinger equation, and thus the foundations for the development of DFT, they are unable to provide a form for $\mathrm{F_{HK}}[\rho(\mathrm{r})]$. As a result; the information needed to calculate the

ground state of the system is still missing.

2.4.2 Kohn-Sham equations

Kohn and Sham published a series of equations based on the Hohenberg-Kohn theorems that allow the calculation of the ground state of a system. These are known as the Kohn-Sham equations and have formed the basis of modern DFT. They proposed that with the knowledge of the electron density ρ(r) of a given system with a set of interacting electrons, an equivalent system with the same electron density could be derived with non-interacting electrons [82]. Applying this approach to the problem presented by the Hohenberg-Kohn theorems of the unknown energy functional F[ρ(r)] enables it to be separated into a series of component terms, as shown in Equation 2.7.

$$\mathbf{F_{HK}}[\boldsymbol{\rho}(\mathbf{r})] = \mathrm{E_{ke}}[\boldsymbol{\rho}(\mathbf{r})] + \mathrm{E_H}[\boldsymbol{\rho}(\mathbf{r})] + \mathrm{E_{xc}}[\boldsymbol{\rho}(\mathbf{r})] \tag{2.7}$$

Here $E_{ke}[\boldsymbol{\rho}(\mathbf{r})]$ is the kinetic energy of non-interacting electrons and $E_H[\boldsymbol{\rho}(\mathbf{r})]$ is the Hartree term, containing the Coulombic energy of the electron-electron interactions. The final term ($E_{xc}[\boldsymbol{\rho}(\mathbf{r})]$) is used to describe the contribution to the energy functional from the exchange-correlation term and the energy difference between the real interacting electrons and the hypothetical non-interacting system. Essentially the exchange-correlation term can be viewed as a term containing all the unknowns of the problem into a single contribution that can be approximated [97].

It is important to note that the Hartree term ($E_H[\boldsymbol{\rho}(\mathbf{r})]$) does not account for the correlation of electron motion. Instead, this term is defined by the summation of the classical pairwise interactions between charge densities, as shown in Equation 2.8.

$$E_H[\boldsymbol{\rho}(\boldsymbol{r})] = \frac{\mathbf{1}}{\mathbf{2}} \int \frac{\boldsymbol{\rho}(\boldsymbol{r})\boldsymbol{\rho}(\boldsymbol{r'})}{|\boldsymbol{r} - \boldsymbol{r'}|} \boldsymbol{dr dr'} \tag{2.8}$$

It is important to note that in principle, both the kinetic energy (E_{ke}) and Hartree (E_H)) terms are known. While the exchange-correlation term is only known for a few simple systems, its definition is crucial to DFT research and is discussed in Section 2.4.3 below.

Taking the assumption behind the Kohn-Sham energy functional and combining it with the Hohenberg-Kohn theorems leads to the Schroedinger-like Kohn-Sham equation [98], given

by:

$$\left[\frac{-\hbar^2}{2\mathbf{m_e}}\vec{\nabla}^2 + \mathrm{V_{eff}[r]}\right]\Phi_i(\mathrm{r}) = \varepsilon_i\Phi_i(\mathrm{r})\,, \mathrm{i} = 1, \ldots\ldots\ldots, \mathrm{N} \tag{2.9}$$

Where $\Phi_i(r)$ is the Kohn-Sham orbitals of non-interacting electrons, ε_i are the orbital energies and $V_{eff}[\mathbf{r}]$ is the effective potential of the system.

This equation can be simplified to derive a stationary solution of the Schrödinger equation (Equation 2.10), subject to assumptions. Here $\boldsymbol{V_{ext}}(r)$ and $V_{xc}[\mathbf{r}]$ denote the external potential and the exchange-correlation potential, respectively. $V_{xc}[\mathbf{r}]$ is related to the exchange-correlation energy by Equation 2.11.

$$\mathrm{V_{eff}[r]} = \mathbf{V_{ext}}(\mathrm{r}) + \int \frac{\boldsymbol{\rho}(\mathbf{r}')\mathbf{dr}'}{|\mathbf{r}-\mathbf{r}'|}\mathbf{dr}' + \mathrm{V_{xc}[r]} \tag{2.10}$$

$$\mathrm{V_{xc}[r]} = \frac{\boldsymbol{\delta}\mathrm{E_{xc}[\rho]}}{\boldsymbol{\delta\rho(r)}} \tag{2.11}$$

This method allows DFT to find the solutions to the Schrödinger's equation through a self-consistent iterative approach. An initial 'best guess' is made for the electron density, typically by superimposing all the single electron densities. This is used to calculate an initial effective potential (V_{eff}) which is subsequently used to generate the Kohn-Sham orbitals of the system, using Equation 2.9. The orbitals can then estimate an improved electron density for the system through Equation 2.12.

$$\boldsymbol{\rho(r)} = \sum_{\boldsymbol{i=1}}^{N_e} |\Phi_i(r)|^2 \tag{2.12}$$

The improved estimate of the electron density is then used to update $V_{eff}(r)$ in an iterative process until a converged value of the electron density is obtained. This electron density (which corresponds to the ground state energy) allows all ground state properties to be defined, as stated in the second of the Hohenberg-Kohn theorems. It is important to note that in order to generate an accurate value of V_{eff} at each step, a suitable exchange-correlation function ($V_{xc}[\mathbf{r}]$) needs to be specified. Since the exact form of this term is unknown, defining a valid approximation to this term is crucial to the accuracy of the ground state electron

density thus calculated.

2.4.3 Exchange-correlation functionals

In the Kohn-Sham DFT framework, the main uncertainty is the exact nature of the exchange-correlation energy functional ($E_{xc}[\boldsymbol{\rho}(\mathbf{r})]$) term which is unknown for the vast majority of systems. This term has been calculated for a homogeneous electron gas, where the exchange energy is known analytically and Monte Carlo methods have been used to accurately calculate the correlation energy. However, for almost every other system the nature of exchange-correlation energy functional ($E_{xc}[\boldsymbol{\rho}(\mathbf{r})]$) remains unknown. Thus, an approximation is required [99].

The approximation of this term is considered a significant source of error for current DFT calculations. Therefore, the accuracy of the whole DFT technique depends on finding a good approximation of this quantity. There are a large number of exchange-correlation functions available for typical DFT calculations, which vary in terms of suitability, accuracy and computational cost. These are derived either semi-empirically or purely theoretically, although there are differing opinions on the best approach and it depends on the exact calculations to be made. The most common functionals used include those based on the Local Density Approximation (LDA), its expansion the Generalised Gradient Approximation (GGA) and their Hubbard U corrected versions (LDA+U/GGA+U); these will be discussed in further detail below.

Local Density Approximation

The local density approximation (LDA) is based on the assumption that the exchange-correlation terms depend only on the local value of $\boldsymbol{\rho}(\mathbf{r})$; i.e., it treats a non-homogeneous system as locally homogeneous [100]. Therefore, the exchange-correlation energy is expressed as follows:

$$E_{xc}^{LDA}[\rho] = \int \rho(r)\, \varepsilon_{xc}[\rho(r)] d^3r \tag{2.13}$$

Where $\varepsilon_{xc}[\rho]$ is the exchange-correlation energy density of a uniform electron gas system having density ρ. In the case of magnetic systems, the LDA must be extended to the Local Spin Density Approximation (LSDA), where the exchange energy and Correlation is a functional of the two spin contributions (up) and (down):

$$E_{xc}^{LDA}[\rho_{\uparrow}.\rho_{\downarrow}] = \int \rho(r)\,\varepsilon_{xc}[\rho_{\uparrow}(r),\rho_{\downarrow}(r)]d^3r \qquad (2.14)$$

This approximation works well to reproduce ground state properties such as bond lengths, crystal structure, and phonon frequencies with a high degree of accuracy in many materials. Nevertheless, there are significant shortcomings to the LDA approach. Notably, LDA overestimates the binding energies, generally underestimates the band gaps of the materials and incorrectly predicts some structures of electronic ground states. When these properties are of importance, theories of higher order are required, commonly the Generalised Gradient Approximation (GGA).

The generalized gradient approximation

One approach to improve the LDA is to make the exchange-correlation functional not only dependent on the local density, but also on the gradient of the density. This approximation is called the generalized gradient approximation (GGA). In this formalism, the exchange-correlation functional (Eq. 2.13) is written as

$$E_{xc}^{GGA}[\rho] = \int \rho(r) f[\rho(r), \nabla\rho(r)]\; d^3r \qquad (2.15)$$

The GGA approach has been able to more accurately reproduce properties such as crystal structure and binding energies than LDA. Although the GGA was able to produce a more realistic model for the band gap of materials than LDA, it still tends to underestimate band gap energies [101]. This is particularly problematic when it comes to materials with partially filled d- and f -orbitals, such as transition metals and rare earth elements. The so-called hybrid functionals or the Hubbard U corrections are often applied to overcome this problem. Since I have used this latter correction in this work, it deserves to be described in more detail below.

Method DFT + U

Systems containing strongly correlated electrons are often poorly represented by a standard LDA/GGA approach for the exchange-correlation functional [101, 102]. This involves materials containing elements with partially filled d and f orbitals, such as transition metals and rare earths. These are particularly relevant to the positive electrode materials considered in this work since they all contain transition metal elements.

Using an LDA exchange-correlation functional on systems containing transition metals or rare

earths allows the prediction of partially filled d-bands, with metallic type electronic structures with itinerant d electrons. However, it is experimentally known that transition metal and rare earth compounds exhibit localized d and f electrons, leading to distinct and separate occupied and unoccupied d electron bands [103]. Accordingly, to match the theory to the experiment, the exchange-correlation functional is modified to take into account the strong on-site correlation of d- and f- electrons. This is achieved by separating the treatment of s and p electrons from d and f electrons, with their Coulombic interaction accounted for by a Hartree-Fock mean-field approximation.

The strength of the correction made to the exchange-correlation functional is governed by the Hubbard Coefficient (U), which results in LDA+U and GGA+U approaches [104]. The value of U directly impacts the energy gap between the occupied and unoccupied bands in the system and must be chosen wisely to correctly represent the system of interest.

2.4.4 Applying DFT to Solids

Finding a solution to the Schrödinger equation so that certain properties of a given material can be calculated could be a very complex and costly task; especially where solid-state systems are concerned. For such solid-state systems, we normally consider the given system to contain an infinite number of ions and electrons, which would demand the wave function to be determined for all electrons. Moreover, since the wave function of each electron extends over the entire lattice, it would take an infinite number of basis functions to describe. Luckily, the periodic nature of solid-state systems implies that the inherent symmetry (periodic boundary conditions) reduces the requirement to consider such infinite quantities making the problem solvable.

Periodic Boundary Conditions

Periodic boundary conditions are considered crucial to successfully model large solid-state systems because they are able to decrease the amount of computational time required. Due to the symmetry of crystalline solids, they can be divided into unit cells, which consist of a relatively small number of atoms, ions, or molecules. Therefore, Unit cells can be repeated continuously in all three dimensions.

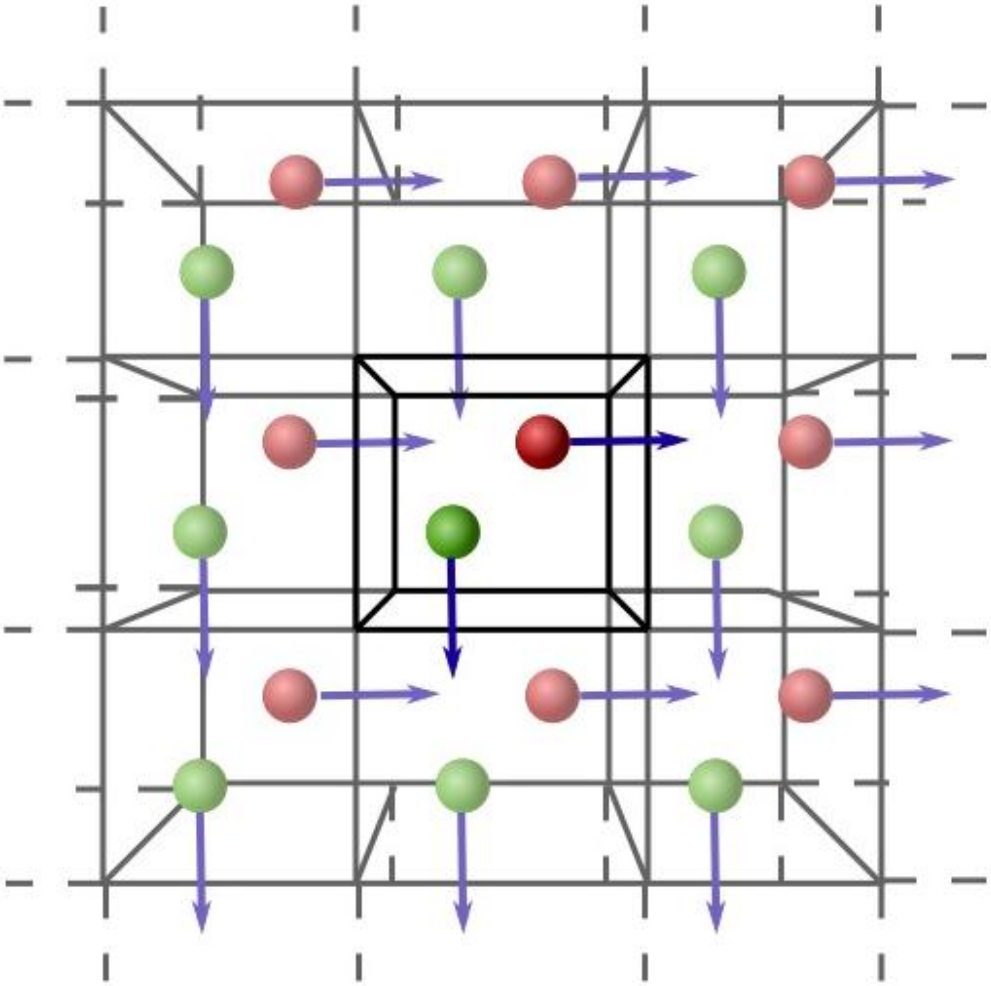

Figure 2.1: Example of periodic boundary conditions [105].

Using periodic boundary conditions means that during a simulation, the unit cell of interest is surrounded in all directions by identical images of itself (Figure 2.1). These images allow the ions contained within the unit cell to interact with each other, as well as with the other ions contained in the images. The ions contained in the images interact only with the ions contained in the unit cell. Consequently, periodic boundary conditions are essentially used to make a simulation cell 'feel' as if it is part of a large extended solid-state system.

Reciprocal Lattice

Although crystal systems are conventionally described in real space, computational techniques may require the lattice properties to be defined using reciprocal space, or k-space. A real-space description in terms of lattice parameters a, b, and c can be projected into a k-space description in terms of $a*$, $b*$, and $c*$ using the relationships,

$$a^* = 2\pi \frac{b \times c}{a.\, b \times c} \tag{2.16}$$

$$b^* = 2\pi \frac{a \times c}{b.\, a \times c} \tag{2.17}$$

$$c^* = 2\pi \frac{a \times b}{c.\, a \times b} \tag{2.18}$$

In real space, a unit cell with lattice vectors a, b and c, is employed to describe the infinitely repeating lattice of a crystal system. Likewise, in reciprocal space, this primitive cell can be defined as the Brillouin Zone. This is a fundamental concept for the description of periodic systems as within its volume a complete description of the wave-function can be provided. This concept is neatly explained in Blochl's theorem [103].

Blochl's Theorem

Blochl's Theorem [104] states that the wave function of an electron (i), within a periodic field, can be written as a product of two components; a wave-like term and a term with the same periodicity of the external field (the periodicity of the unit cell) as shown in Equation (2.19)

$$\Phi_i(r) = e^{ikr} f_i(r) \tag{2.19}$$

where k is the wave-vector in the Brillouin zone and controls the frequency and direction of the wave-like term, and r is used to describe the position vector. The periodic component of the wave-function can be constructed through a combination of a basis set of discrete plane waves (e^{iGr}), with all translations to symmetrically identical lattice points represented by the wave-vectors (G). In this approach $\boldsymbol{f_i(r)}$ becomes:

$$f_i(r) = \sum_G c_{iG}\, e^{iGr} \tag{2.20}$$

Combining equation 2.19 with equation 2.20 leads to a plane wave description of the wave function given by

$$\Phi_i(r) = \sum_G c_{i,k+G}\, e^{i(k+Gr)} \tag{2.21}$$

The solution is defined by the coefficient $\mathbf{c_{i,k+G}}$. This summation should be performed using a suitable value of $\mathbf{G}$, to ensure the system is adequately represented.

Plane waves

The choice of the plane wave basis set is critical to providing accurate results with a reasonable computational expense. Two approximations are employed to reduce the complexity of the problem. Firstly, higher-order plane waves with a larger |G| will have higher kinetic energy and therefore will contribute less to the ground state wave-function. Consequently, a |G| (or energy) cutoff is applied to the summation in equation 2.21; above this value, plane waves are not considered to contribute significantly to $\Phi_{\mathbf{i}}(\mathbf{r})$ and are not evaluated. Secondly, as Φ is a continuous function of *k*, small changes in the value of k will result in a minimal impact on Φ [104]. Therefore, a suitable description of k-space can be achieved by sampling a finite number of points in *k*-space. The set of "*k*-points" to be sampled can generally be made smaller than the sampling points that would be required for a real space projection of the wave-function. The symmetry of most solid-state systems means that often many k-points sample equivalent points in the Brillouin zone. Since double sampling is redundant, the number of k points can be further reduced through symmetry operations. This is usually accomplished using either a Gamma point-centered k-point mesh ((0, 0, 0) in the Brillouin zone) or one chosen through the Monkhurst-Pack method [106].

For practical applications, it is essential to check the validity of these approximations in a process known as "convergence testing". This requires the variation of the plane-wave cutoff and the k-point mesh, and the resulting effect on the ground-state properties of the system to be recorded. Convergence is deemed to be achieved when the property of interest no longer varies with further change in the k-point mesh or the plane wave cutoff. The lowest plane wave cutoff and the coarsest k-point mesh that satisfy the convergence are generally chosen in order to minimize the computational cost.

Pseudopotentials

Near the nuclei of an atom, there is a significant variation in the electron wave-function. A large number of plane waves would be required to provide an adequate representation of the fine spatial details associated with the wave function at small distances from the nuclei. This would lead to reduced calculation speed and therefore increased computational cost. However, since the core electrons are not typically involved in chemical bonding, they can be

considered effectively constant. Therefore, a common approximation is to separate the treatment of the core and valence electrons of an atom into two distinct regions by using pseudopotentials [107].

The pseudopotential is a smooth function which is used to describe the core potential and can be represented by a reduced set of plane waves, reducing the overall computational expense of the calculation. Typically, the distinction between the core and valence electrons is made by using a cutoff radius. Within this radius, a pseudopotential description is applied that can accurately describe the original core potential. By applying this approximation, the generated wave function will only provide a reliable representation of the valence electrons of the system, so the core electrons can no longer be considered. This approximation uses an accurate representation only for the valence electrons. However, if the cutoff radius has been correctly chosen, it is considered acceptable for many ground-state properties of real systems.

The `softness' of a pseudopotential describes both the smoothness of the function and the size of the cut-off radius from the nuclei. Smoother pseudopotentials can be described using fewer basis functions. However, a very soft potential does not transfer well between systems as it requires a large cutoff radius and can lead to an inaccurate representation of the atom. An ideal pseudopotential will accurately reproduce the wave-function of an atom across a wide range of chemical systems [104].

In this thesis, the PAW (Projector Augmented Wave) method has been used. The PAW approach embodies a particularly smooth pseudopotential in combination with local auxiliary functions allowing it to represent the complete wave function of all electrons.

2.5 Software used

Quantum ESPRESSO (QE) is an integrated suite of Open-Source computer codes for electronic-structure calculations and materials modeling at the nanoscale. It is based on density-functional theory, plane waves, and pseudopotentials. QE was used for all DFT calculations [108]. The visualization software VESTA and XCrySDen were used to visualize structures and also for plotting k-paths across the Brillouin zone [106]. Origin Software was used for data analysis and plotting [109].

Relaxation algorithms in DFT

Two main relaxation algorithms exist in QUANTUM ESPRESSO [108], the «vc-relax»

(where «vc» means variable cell) and the «relax» algorithms. To use these algorithms, one must first define lattice vectors and atomic positions of the crystal in the beginning. The «vc-relax» algorithm tunes all atomic positions and lattice vectors in order to minimize the energy. Each step of the algorithm leads to a change in the parameters, after which a self-consistent computation (see SCF section) is performed. If the newly calculated energy is lower than the previous energy, the calculation is repeated with new parameters. This operation is continued until the differences in energy and forces between two successive runs are less than the convergence threshold set by the user. Similar operations are performed by the "relax" algorithm, which simply adjusts the atomic positions, without changing the lattice vectors. The ‘vc-relax’ algorithm in QUANTUM ESPRESSO was used for all the calculations in this thesis, sometimes in combination with ‘relax’ to further check for any changes that could be made to the atomic positions to get a more stable state.

Self-consistent field (SCF) calculation

Self-consistent field (SCF) methods include Hartree-Fock (HF) theory and Kohn-Sham (KS) density functional theory (DFT). An SCF calculation in QUANTUM ESPRESSO [108] is done by specifying 'SCF' in the input file. This must be done at the beginning of any DFT calculation. The self-consistent field method is an iterative method that involves making an initial estimate of the charge density and then solving the Kohn-Sham equation to calculate the charge density [95]. This operation is repeated until the charge density converges. The algorithm of Figure 2.2 is followed, which is the basis of all DFT calculations [110].

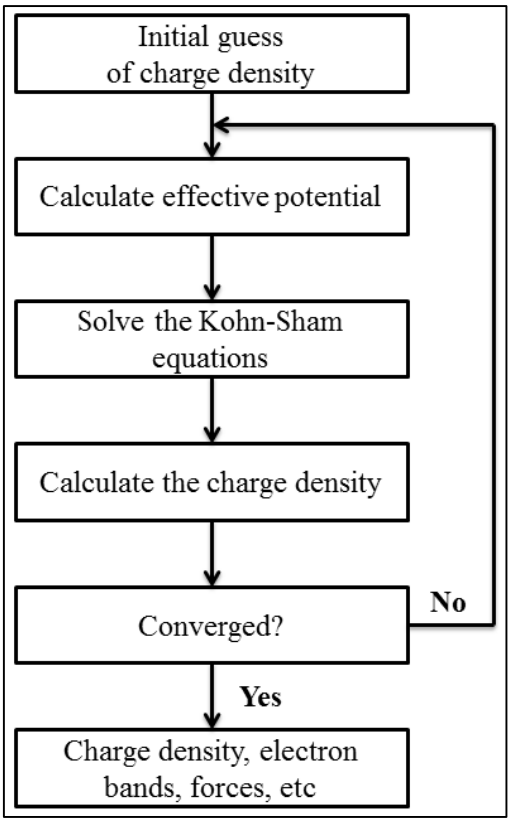

Figure 2.2: Self-consistent field algorithm.

Non self-consistent calculations

After carrying out an SCF calculation, a non-self-consistent field (NSCF) calculation is performed to compute properties such as band energies and density of states (DOS). In QUANTUM ESPRESSO, an NSCF calculation is done with the k-point grid and the number of bands required is specified by the user (if the latter is not indicated, only occupied bands will be calculated). NSCF calculation starts from the potential obtained by SCF previously. Therefore, a calculation with a denser grid than SCF may be performed at a higher speed. Nevertheless, since the computation is non-self-consistent, the previous SCF run must be sufficiently convergent to obtain accurate results. In addition, if the user is only interested in the Kohn Sham states for a given set of k points, a "band" calculation can be performed, which is also a non-self-consistent calculation.

2.6 Finding Transition States

As well as finding energy minima, it is also useful to be able to locate saddle-points in the potential energy surface, as the energy barrier (difference between lowest energy minimum and saddle-point) determines the frequency of certain chemical events. In the case of this

work, the Li-ion energy barrier can give us many insights into the performance of olivine as cathode material for lithium-ion batteries. In this work, the technique used to locate the transition state and extract the Li-ion migration barrier is nudged elastic band method.

Nudged Elastic Band (NEB)

The nudged elastic band (NEB) is a method for finding saddle points and minimum energy pathways between two stable structures (minima). In the Nudged Elastic Band (NEB) method, a chain of images of the system is constructed by linear interpolation between the initial and final states. Then, these images are linked together by elastic bands in such a way that they form a discrete representation of a path between the initial and the final state. The image chain can be denoted [R_0, R_1, R_2,...R_N], where R_0 and R_N are the initial and final states, respectively. N-1 images are adjusted by the optimization algorithm [111].

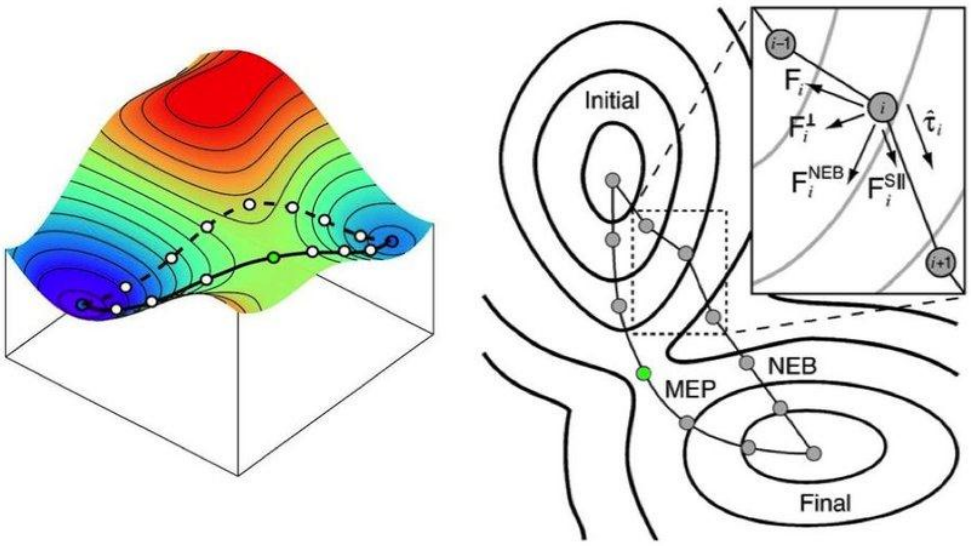

Figure 2.3: Principle of NEB calculation method. The dashed line indicates the path of the initial assumption. After applying the NEB method, the configurations are located along the minimum energy path (continuous line). The green dot represents the transition state (saddle point) [112].

In the NEB method, the total force acting on an image is the sum of the spring force along the tangent and the true force perpendicular to the tangent [111].

$$F_i = F_i^s|_{||} - \nabla E(R_i)|_{\perp} \qquad (2.22)$$

Where the true force is defined by

$$\nabla E(R_i)|_{\perp} = \nabla E(R_i)|_{\perp} - \nabla E(R_i)|_{\perp}.\hat{\tau_i} \qquad (2.23)$$

$E(R_i)$ is the energy of the system at image R_i and $\hat{\tau_i}$ is the normalized local tangent at image i. The spring force is given by

$$F_i^s|_{||} = k(|R_{i+1} - R_i| - |R_i - R_{i-1}|)\,\hat{\tau_i} \qquad (2.24)$$

where k is the spring constant. An optimization algorithm is then employed to move the images according to the force in equation (2.22) to the "Minimum Energy Pathway" MEP, as shown in Figure 2.3.

The NEB method is particularly useful for finding migration barriers within materials with low symmetry crystal structures, where the migration pathways are not parallel to the cartesian axes. NEB is subject to periodic boundary conditions, so it is important to ensure that the simulation cell is large enough to prevent interactions between replicas in neighboring periodic images from becoming significant. For instance, in this thesis, 1× 2 × 2 supercells containing 16 formula units up to 112 atoms were selected to minimize the interaction between the periodic images of the diffused Li-ion [56].

Chapter 3

Nickel and iron single doped $LiMnPO_4$ as cathode materials for Li-Ion Batteries

3.1 Background

As discussed in **Chapter 1**, the spinel and layered oxides cathode materials cannot be used at high temperatures due to chemical instability of highly oxidized species such as Co^{4+}, Ni^{4+} and Mn^{4+} [110]. Because of these limitations, the olivine $LiFePO_4$ (LFP) has been used as the most suitable alternative to $LiCoO_2$ as a cathode material for LIBs, due to its series of advantages like excellent cycle stability (because reactivity of LFP with electrolyte is very low) [113], environmental friendliness, high theoretical capacity, and low cost. In addition, LFP is more stable at high temperatures than layered oxides mentioned before [11][114]. Nevertheless, LFP has a low energy density beside its low operating voltage (3.4 V vs. Li/Li^+) which limits their application in high-energy devices [12, 13]. For this purpose, LIBs research has been focused on developing other olivine phosphate based materials. Among them, $LiMnPO_4$ (LMP) one of the most promising cathode material, $LiNiPO_4$ (LNP) and $LiCoPO_4$ (LCP) which have showed good stability, low cost, environmental friendliness and a high energy density (700 $Wh.kg^{-1}$) [17, 18]. More importantly, LMP has a voltage platform of 4.1 V vs Li/Li^+ which is compatible with conventional electrolyte windows [15, 16]. Unlike, LNP and LCP have high potentials (4.8 and 5.2 V vs. Li/Li^+, respectively) above 4.5 V [14], which exceeds the electrochemical stability window of most commercial liquid electrolytes [115, 116]. Even though its advantages, LMP cathode material has low electronic and ionic conductivities which reduces its efficiency [19, 117]. To overcome these problem, several methods have been applied such as coating LMP with carbon (C) [118], reducing its crystal size [119] and cation doping [23].

Cation doping has been shown to be the most successful methods to improve the electrochemical performance of LMP as shown by several studies, for example Bakenov et al. prepared $LiMg_xMn_{1-x}PO_4$ (x = 0, 0.02, 0.04, 0.12) by a combination of spray pyrolysis and wet ball-milling with heat-treatment and concluded that the $LiMg_{0.04}Mn_{0.96}PO_4$ cathode exhibits an excellent electrochemical performance [120]. Wang et al. synthesized

$LiMn_{0.9}M_{0.1}PO_4$ (M= Mn, Mg, Fe, Ni and Zn) by the solid-state reaction method and found that the $LiMn_{0.9}Fe_{0.1}PO_4$ compound shows higher intrinsic capacity and conductivity than pristine LMP [121]. Wu et al. synthesized $LiMn_{1-x}Cr_xPO_4/C$ composite by a sol–gel combined ball milling method. They revealed that 3% Cr-doped sample exhibits the best electrochemical behavior [122]. In addition, Fang et al. synthesized pure and Zn-doped LMP by solid-state reaction method and showed that a small amount of Zn doping is very beneficial for the performance of LMP due to the increase of Li-ion diffusion and the decrease of charge transfer resistance [123].

Besides the above experimental investigations, LMP cathode have been investigated in several theoretical studies [124, 125]. For instance, Alfaruqi et al. investigated the effect of Ni substitution on structural, electronic and kinetic properties of LMP [27] and Nie et al. presented the first principle study of Jahn Teller effect of Li_xMnPO_4 and also its structural and electronic properties [126] In addition, structural and electronic properties of $LiMnPO_4$ with the substitution of Mn by Co, Cr, Cu, Fe and Ni atoms were reported by Sukkabot et al [74].

In this context, the present study aims to optimize the electronic and ionic conductivities in LMP, as a function of Ni and Fe doping which will improve the performance of LMP. In this work, a detailed study of the geometry, the electrochemical potential, the capacity and electronic structure of lithiated /delithiated phases of $LiMn_{1-x}M_xPO_4$ (M= Ni, Fe; x=0, 0.25, 0.5, 0.75, 1) were investigated.

3.2 Computational details

In this work, all calculations were performed using density function theory (DFT) within the projector augmented wave (PAW) method as implemented in Quantum Espresso code [108, 104]. The Perdew−Burke−Ernzerhof adapted version for solid state systems (PBEsol) with the generalized gradient approximation (GGA) were used to account for the exchange correlation interactions. In order to treat the strong correlation of d-electron orbitals in transition metals, we applied Hubbard correction (U) [127, 128]. The used U values for Mn, Ni and Fe are 4.5, 5.5 and 3.5 eV, respectively. An energy cutoff of 88 Ry (1197.30 eV) was selected to determine the sufficient size of plane waves to expand the Khon Sham orbitals and the Monkhorste-Pack scheme for 4×5×6 k-mesh grids sampling were chosen to discretize the irreducible Brillouin zone. In addition, all the atomic positions were relaxed, with Broyden-Fletcher-Goldfarb-Shanno (BFGS) algorithm [129], and a Gaussian smearing method with

0.01 eV width, until the total convergence of energy, stress and forces became less than 1×10^{-6} Ry, 0.01 kbar and 10^{-4} Ry/Bohr, respectively.

During diffusion calculation a $1 \times 2 \times 2$ supercell, containing 16 formula units with atoms number up to 112, was used to minimize the interaction between periodic images. The nudged elastic band (NEB) method was used to calculate the Li migration barrier [130]. All crystal structures was drawn using VESTA software [109]. The theoretical capacity was calculated by the following expression [131]:

$$C(mAhg^{-1}) = \frac{(n \times F)}{(3600 \times M_w)} \tag{3.1}$$

where n, F and M_w are the number of Li in $LiMn_{1-x}M_xPO_4$, the Faraday constant and the molecular weight of the compounds ($LiMn_{1-x}M'_xPO_4$ (x=0, 0.25, 0.5, 0.75, 1) respectively.

$LiMPO_4$ (M=Mn, Fe, Ni) has no spin ordering at room temperature and are anti-ferromagnetic below their Néel temperatures [132]. In this work a ferromagnetic (FM) ordering was used during all calculation for all lithiated/delithiated materials because the energetic differences between the anti-ferromagnetic and ferromagnetic states are small, these materials are used at temperatures greater than the room temperature. This approach was previously used in [133, 134].

3.3 Results and Discussions

3.3.1 Crystal Structure

The structure of pure $LiMnPO_4$ was initially optimized based on the experimental crystal structure. $LiMnPO_4$ unit cell contains four different Mn-sites which can be occupied by either Ni or Fe leading to various concentrations (0.25, 0.5, 0.75 and 1). The so obtained mixing olivines ($LiMn_{1-x}M_xPO_4$ (with M= Ni, Fe; x=0.25, 0.5, 0.75 and 1)) are relaxed once further. We note that where a variety of cation distributions were possible within the unit cell, the different possibilities were built and optimized and the configuration with the lowest energy was selected.

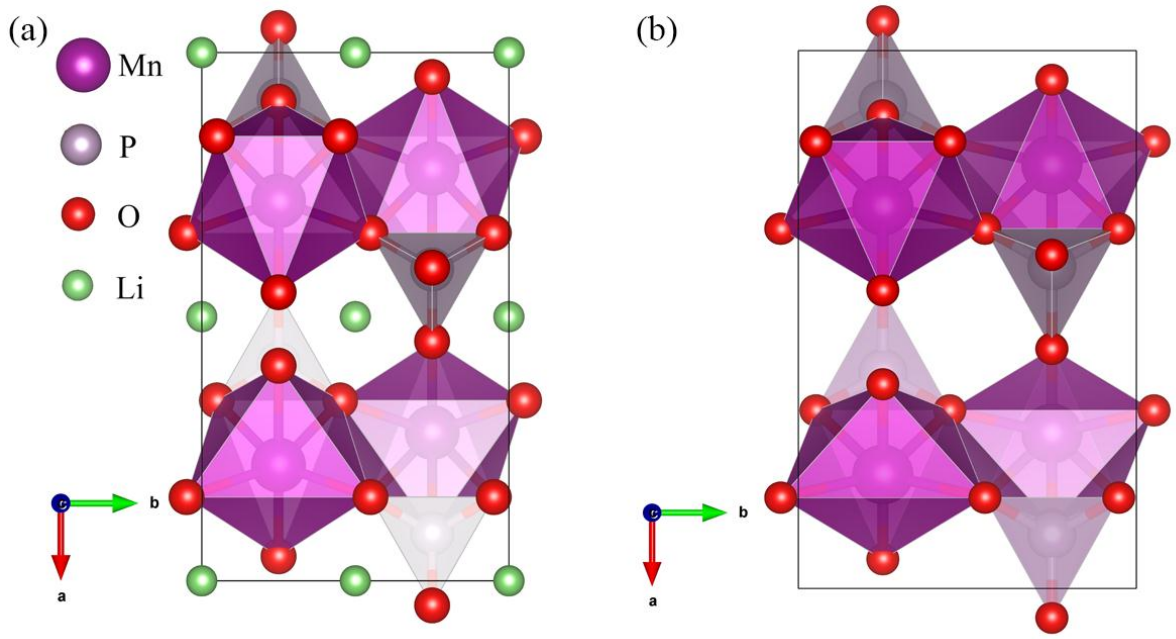

Figure 3.1: Crystallographic structures of (a) $LiMnPO_4$, (b) $MnPO_4$. Purple is MnO_6 octahedral unit.

$LMP/MnPO_4$, $LNP/NiPO_4$ and $LFP/FePO_4$ have orthorhombic unit cells with four formula units and a symmetry group Pnma (number 62). All structures are constructed from M'O6 octahedral (M'=Mn, Ni and Fe) and PO_4 tetrahedral, this construction creates canals along the b-axis which are allow to store and diffuse Li ions. The relaxed structures of LMP and $MnPO_4$ are shown in Figure 3.1a, b. The calculated lattice parameters and unit cell volumes of these compounds are listed in Tables 3.1 and 3.2. These results show that our findings are in good agreement with experimental measurements [6, 135, 136] and previous DFT results [136, 137]. For instance, the deviations of the cell volumes from experimental values are only 0.08%, 1.13% and 2% for LNP, LMP and LFP, respectively. These results indicate that using the (DFT+U) method with the chosen parameters is reasonable for the studied materials.

The mixed olivine structures $LiMn_{1-x}M_xPO_4/Mn_{1-x}M_xPO_4$ (M=Ni, Fe; x=0.5, 0.25, 0.75) were relaxed and the results are presented in Figure A.1 (Supporting Information). Tables 3.1 and 3.2 present the relaxed lattice parameters and primitive cell volumes of these mixed structures. These results agree well with theoretical and some available experimental results (see Table 3.1 and 3.2). The variations in cell parameters and volumes of the Ni and Fe doped LMP structures with different percentages (0%, 25%, 50%, 75% and 100%) are drawn in Figure A.2. The unit cell parameters and cell volume decrease when the amount of substituting Ni^{2+} increases (as shown in Figure A.2 (a).

Table 3.1: Optimized lattice parameters for $LiMn_{1-x}Ni_xPO_4$ and $Mn_{1-x}Ni_xPO_4$ (x=0, 0.25, 0.5, 0.75, 1) compounds.

Compounds	a(Å)	b(Å)	c(Å)	V(Å^3)	*Angles*
$LiMnPO_4$					
Our Work	**10.54**	**6.14**	**4.74**	**306.75**	
Cal.[137]	**10.55**	**6.13**	**4.78**	**309.13**	
Exp.[10]	**10.45**	**6.11**	**4.75**	**303.28**	$\boldsymbol{\alpha = 90}$ $\boldsymbol{\beta = 90}$ $\boldsymbol{\gamma = 90}$
$MnPO_4$					
Our Work.	**9.85**	**6.05**	**4.90**	**292.00**	
Cal.[14]	**9.90**	**6.06**	**4.93**	**295.77**	
Exp.[138]	**9.69**	**5.93**	**4.78**	**274.67**	
$LiMn_{0.75}Ni_{0.25}PO_4$					
Our Work.	**10.46**	**6.08**	**4.73**	**300.81**	
Cal.[134]	**10.42**	**6.07**	**4.73**	**299.16**	$\boldsymbol{\alpha = 90}$ $\boldsymbol{\beta = 90}$ $\boldsymbol{\gamma = 90}$
$Mn_{0.75}Ni_{0.25}PO_4$					
Our Work.	**9.78**	**5.91**	**4.83**	**279.17**	
Cal.[134]	**9.79**	**5.98**	**4.88**	**285.33**	
$LiMn_{0.5}Ni_{0.5}PO_4$					
Our Work	**10.35**	**6.00**	**4.71**	**292.49**	$\boldsymbol{\alpha = 90}$ $\boldsymbol{\beta = 90}$ $\boldsymbol{\gamma = 90}$
$Mn_{0.5}Ni_{0.5}PO_4$					
Our Work	**9.77**	**5.84**	**4.80**	**273.87**	
$LiMn_{0.25}Ni_{0.75}PO_4$					
Our Work	**10.21**	**5.94**	**4.70**	**285.04**	$\boldsymbol{\alpha = 90}$ $\boldsymbol{\beta = 90}$ $\boldsymbol{\gamma = 90}$
$Mn_{0.25}Ni_{0.75}PO_4$					
Our Work	**9.76**	**5.72**	**4.76**	**265.73**	
$LiNiPO_4$					
Our Work	**10.07**	**5.86**	**4.67**	**275.57**	
Exp.[135]	**10.04**	**5.87**	**4.68**	**275.81**	$\boldsymbol{\alpha = 90}$ $\boldsymbol{\beta = 90}$ $\boldsymbol{\gamma = 90}$
$NiPO_4$ Our Work	**9.76**	**5.65**	**4.74**	**261.38**	
Cal.[14]	**9.97**	**5.77**	**4.82**	**277.27**	

Table 3.2: Optimized lattice parameters for $LiMn_{1-x}Fe_xPO_4$ and $Mn_{1-x}Fe_xPO_4$ (x=0, 0.25, 0.5, 0.75, 1) compounds.

Compound	a(Å)	b(Å)	c(Å)	V(Å^3)	***Angles***
$LiMn_{0.75}Fe_{0.25}PO_4$					
Our Work	**10.55**	**6.12**	**4.74**	**306.04**	α =90
Exp.[139]	**10.431**	**6.077**	**4.734**	**300.08**	$\beta = 90$
					$\gamma = 90$
$Mn_{0.75}Fe_{0.25}PO_4$					
Our Work	**9.77**	**5.90**	**4.81**	**277.26**	α =90
					$\beta = 91.3$
					$\gamma = 90$
$LiMn_{0.5}Fe_{0.5}PO_4$					α =90
Our Work	**10.52**	**6.09**	**4.74**	**303.67**	$\beta = 89.89$
Exp.[139]	**10.401**	**6.054**	**4.727**	**297.64**	$\gamma = 90$
$Mn_{0.5}Fe_{0.5}PO_4$					
Our Work	**9.86**	**5.94**	**4.87**	**285.22**	α =90
					$\beta = 89.29$
					$\gamma = 90$
$LiMn_{0.25}Fe_{0.75}PO_4$					
Our Work	**10.43**	**6.05**	**4.72**	**297.83**	α =90
					$\beta = 89.89$
					$\gamma = 90$
$Mn_{0.25}Fe_{0.75}PO_4$					
Our Work	**9.90**	**5.92**	**4.87**	**285.42**	α =90
					$\beta = 89.48$
					$\gamma = 90$
$LiFePO_4$					
Our Work	**10.41**	**6.04**	**4.73**	**297.40**	α =90
Cal.[136]	**10.638**	**5.963**	**4.528**	**294.528**	$\beta = 90$
Exp.[136]	**10.332**	**6.011**	**4.692**	**291.400**	$\gamma = 90$
$FePO_4$					
Our Work	**9.94**	**5.88**	**4.86**	**284.05**	α =90
Cal.[137]	**9.99**	**5.88**	**4.87**	**286.07**	$\beta = 90$
Exp.[11]	**9.821**	**5.792**	**4.788**	**272.357**	$\gamma = 90$

A similar behavior has been observed experimentally by Othman et al. [140]. Figure A.2 (b) presents the variation of the cell volume as a function of Fe content in LMP, which shows a decreasing behavior. Similar effects were found experimentally by Ting-Feng Y et al. [141]. We note however that the angles α and γ are not affected by (Ni, Fe)-substitution in LMP, while, β has been found to undergo a slight change by small amount up to 0.12°. The symmetry of LMP is preserved during the substitution of Mn with various concentrations of Ni since $a \neq b \neq c$, $\alpha = \beta = \gamma = 90°$. Meanwhile, the case of Fe substitutions, there is a slight distortion in the angle β. As a result, this is an indication of symmetry breaking during

Fe substitutions. The mentioned drop in the cell parameters and volumes may be explained by the difference in ionic radius of doping cations 0.83, 0.69 and 0.78 Å for Mn^{2+}, Ni^{2+} and Fe^{2+} [142]. Experimentally, Seo et al. [63] observed that the lattice parameters a, b and c, and the unit cell volume decrease with increasing the amount of Fe^{2+} in $LiMn_{1-x}Fe_xPO_4$. Furthermore, the same behavior has been observed with Co substitution in $LiMn_{1-y}Co_yPO_4$ [62] using DFT method.

This correlation between the doping amount and the cell parameters can be attributed to the metal-oxygen bond and environment. For a better understanding of the interaction between transition ion metal (M' = Mn, Ni and Fe) and oxygen (O), the average bond lengths (M'-O) in MO_6 octahedral of both the pure and mixing olivine structures were investigated and the results are presented in Table A.1, which shows that all the bond lengths have small values in Comparison with Mn-O in LMP pure structure which can indicate a stronger attraction occurs between transition ion metal (Fe, Ni) and O in mixing olivine structure compared to pure LMP. This signifies a good improvement in structural stability of the doped LMP structures.

The calculated unit cell volume change during the extraction of the Li ions was about 4.56%, 7.19%, 6.3%, 6.7%, 5.1%, 9.4 %, 6%, 4.1% and 4.4% for LMP, $LiMn_{0.75}Ni_{0.25}PO_4$, LMNP, LNP, $LiMn_{0.75}Fe_{0.25}PO_4$, LMFP, $LiMn_{0.25}Fe_{0.75}PO_4$, LFP, respectively. The small amount of the volume shrinking (less than 10%) implies generally a structural stability of all compounds which ensures good reversibility, long life cycle and safety upon Li insertion/extraction [126].

In both lithiated/delithiate structures, an $M'O_6$ octahedral has four different type of bonds; two are axial (M'-O_1, M'-O_2) and two in the same equatorial plane (two of M'-O_3 and M'-O_4). The averaged calculated bond lengths (M'−O) in both structures $LiMn_{1-x}M_xPO_4/Mn_{1-x}M_xPO_4$ are listed in Table A.2 a,b. It is clear that all M'-O bond lengths are contracted due to the transition that occurs in the transition metals oxidation state (M'^{2+}/ M'^{3+}), except for M'-O_3 bond length that has been expanded because of the Jahn-Teller distortion [62].

3.3.2 Electronic properties

In this section we will investigate the electronic properties of pure and mixed compounds, which are among the most important factors for cathode materials in LIBs. Electronic properties of all materials were evaluated through the calculation of density of states (DOS).

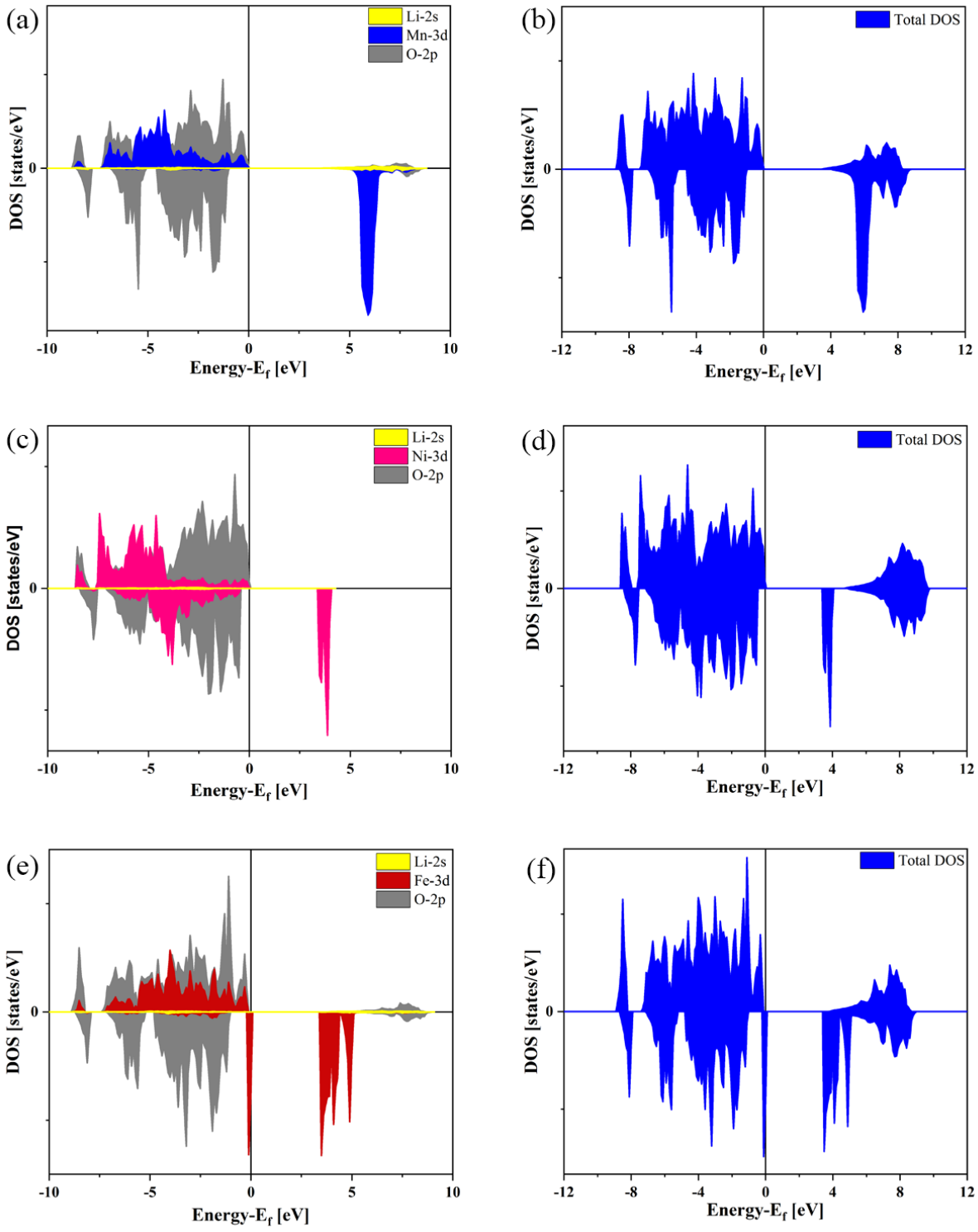

Figure 3.2: Projected DOS of (a) $LiMnPO_4$, (c) $LiNiPO_4$ and (e) $LiFePO_4$ and total DOS of (b) $LiMnPO_4$, (d) $LiNiPO_4$ and (f) $LiFePO_4$.

Figure 3.2 shows the total and partial density of states (TDOS, PDOS) of LMP, LNP and LFP. The calculated band gaps (E_g) for these materials are estimated to be 3.62, 3.45 and 3.44 eV for LMP, LNP and LFP, respectively. These results are in good agreement with previous

reported studies, so that the calculated band gap of LMP is very close to the value (3.75 eV) previously reported by Lethole et al. [62]. The E_g value of LNP found in the present work is close to that previously reported by Galakhov et al. (3.5 eV) [143], while the E_g value of LFP found here is slightly lower than the value reported by Zhou et al. (3.7 eV) [124]. For LMP, there are different values of E_g that have been reported in several DFT studies, for example, Alfaruqi et al. reported 3.08 eV using a Hubbard correction of U=3.9 eV [27], Zhang et al. obtained 3.94 eV for U = 4.5 eV [12] and Kellerman et al. found 3.11 eV for U= 2 eV [144]. This difference in the gap value of LMP can be attributed to the different used Hubbard correction values.

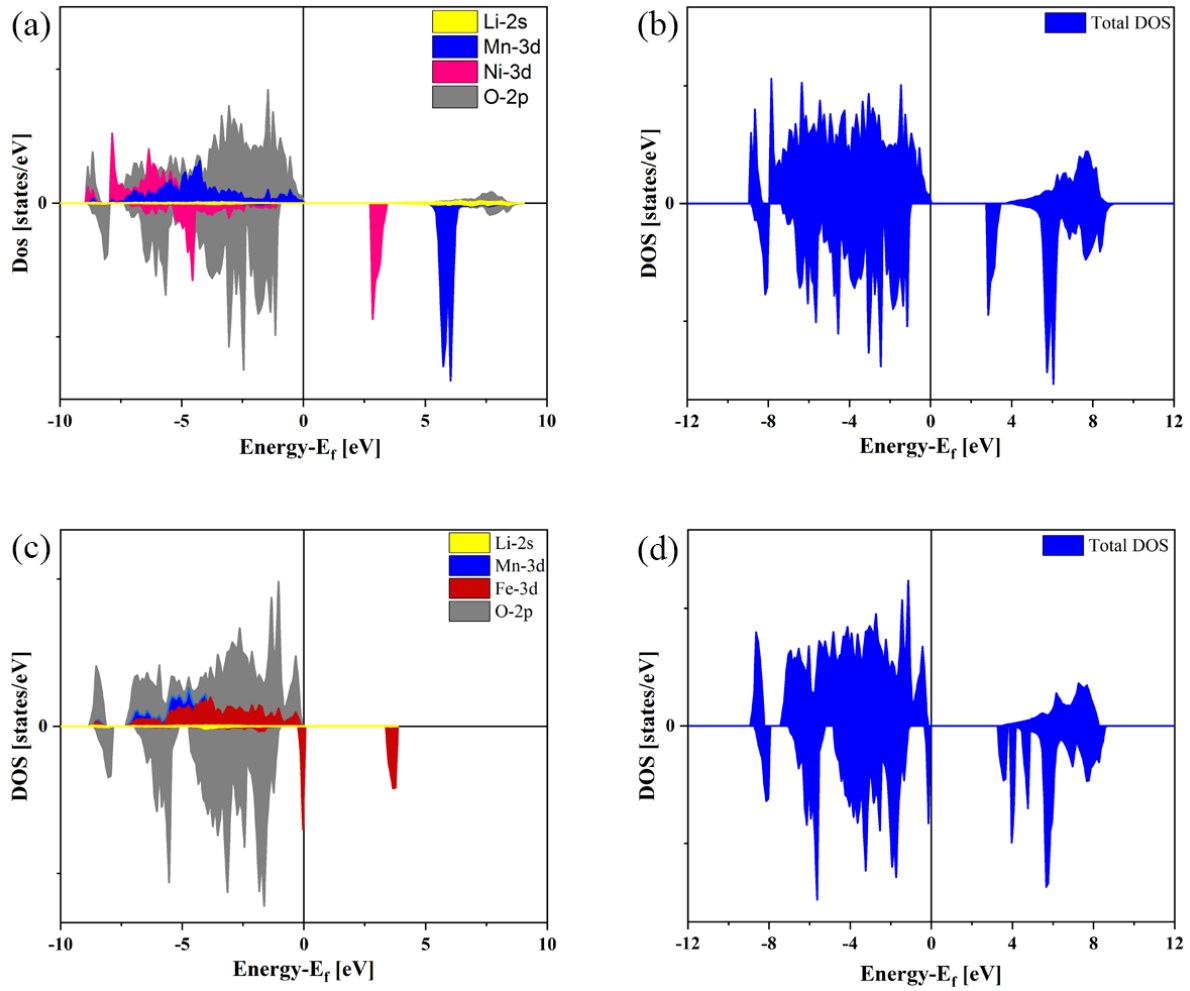

Figure 3.3: Projected DOS of (a) $LiMn_{0.5}Ni_{0.5}PO_4$, (c) $LiMn_{0.5}Fe_{0.5}PO_4$ and total DOS of (b) $LiMn_{0.5}Ni_{0.5}PO_4$ and (d) $LiMn_{0.5}Fe_{0.5}PO_4$.

Based on the PDOS curves, the valence band of LMP is found to be composed of 2*s*, 2*p* and 3*d* orbitals of Li, O and Mn, respectively. Furthermore, the hybridization of Mn and O orbitals has a main contribution in the valence band compared to *s* orbital of Li, whereas the

conduction band is mainly composed of spin-down of the 3*d* orbital. The same behavior has also been observed in the PDOS of LNP and LFP but with both up and down spins contributions in the valance band, this can be explained by the difference in number of electrons in the *d* orbital between Mn, Fe and Ni.

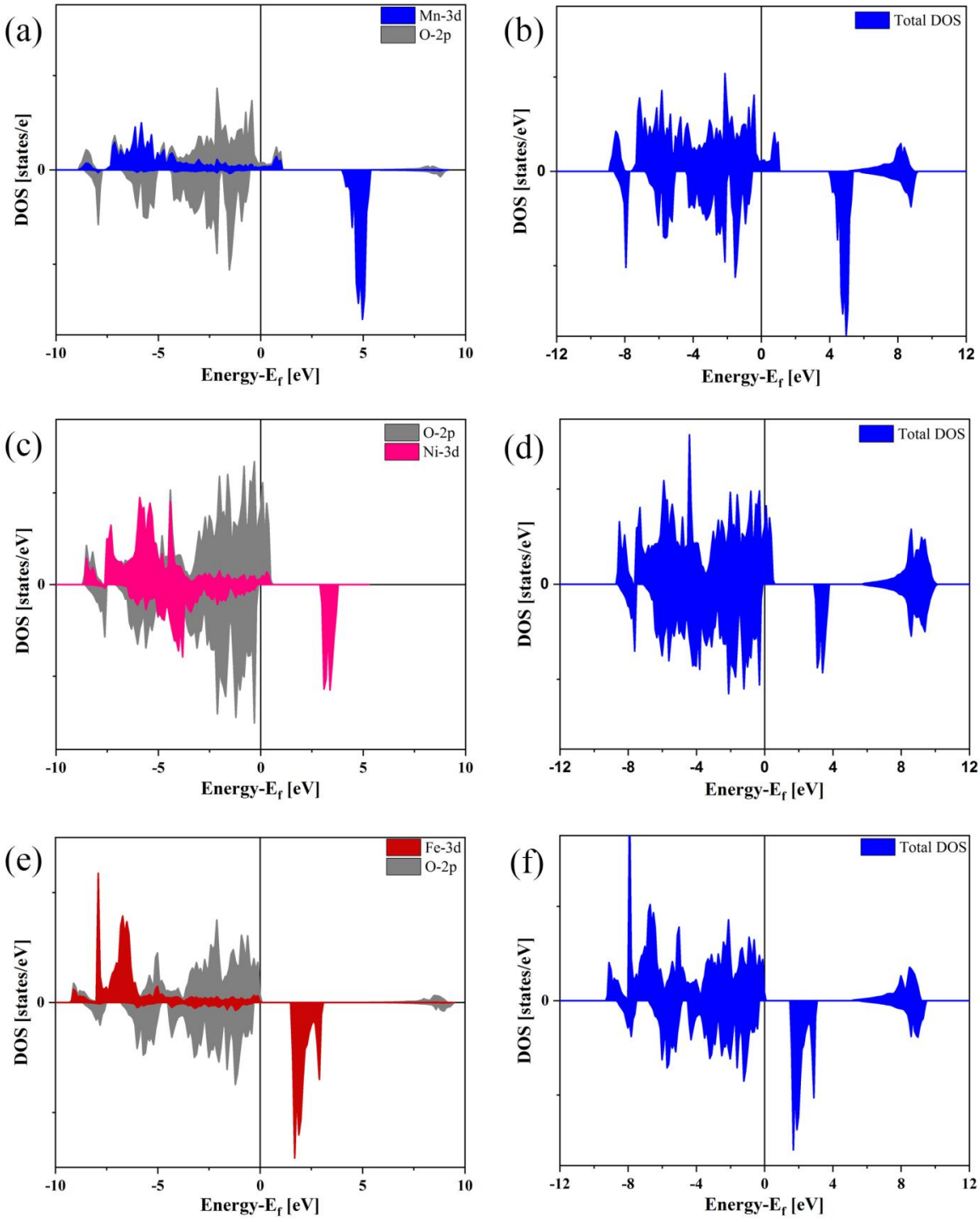

Figure 3.4: Projected DOS of (a) $MnPO_4$, (c) $NiPO_4$ and (e) $FePO_4$ and total DOS of (b) $MnPO_4$, (d) $NiPO_4$ and (f) $FePO_4$.

The TDOS and PDOS of the mixed olivine structures $LiMn_{1-x}M_xPO_4$ are presented in Figure 3.3 (for x=0.5) and Figure A.3 (for x=0.25, 0.75). As observed form these figures, the Ni and Fe substitution leads to the formation of new electronic states derived from Ni and Fe *d*-orbitals in the band gap. So that, the band gap of LMP is reduced from 3.62 to 2.77 eV for LMNP and from 3.62 to 3.35 eV for LMFP, furthermore the band gap of these materials (LMNP and LMFP) is smaller than that of LFP (3.44 eV). In the remaining cases of substitution with Ni and Fe, band gaps less than the pure LMP were observed (see Figure 3.8a below). Substitution of Mn by Ni/Fe in LMP leads to a good improvement in the electronic conductivity, especially for the structures with 50% of Ni (LMNP) and 50% of Fe (LMFP). From these results, it is clearly deduced that all the studied materials have a semiconductor behavior with a band gap that varies according to the amount and nature of the substitution/dopant. Zou et al [134]. and Hu et al [145]. reported also in their experimental measurements that LMP doped with 50% of iron (LMFP) exhibited high performance than pure LMP.

Contrary to all lithiated structures that have a semiconducting state, the delithiated phases exhibit a metallic behavior due to shifting of the Fermi energy level to the valence band as presented in Figure 3.4,5 (for $Mn_{1-x}M_xPO_4$; M= Ni, Fe; x= 0, 0.5, 1) and Figure A.4 (for $Mn_{1-x}M_xPO_4$; M= Ni, Fe; x= 0.25, 0.75). We observe the appearance of contributions of 2p and 3d orbitals of O and M' respectively, near the Fermi level, expect for FPO which that shows a semiconducting character with small gap around 1.3 eV. This value is in good agreement with 1.46 eV reported by Lethole et al. using the DFT+U, with U=5.5 eV [146].

Besides the electronic property, the electrical conductivity of LMP, LMNP and LMFP has been calculated using the Boltztrap code, which is based on the resolution of the Boltzmann transport equation (BTE), with constant scattering time approximation [145]. The electrical conductivity of LMP, LMNP and LMFP are plotted in Figure 3.6 for both spins up and down as a function of chemical potential at room temperature.

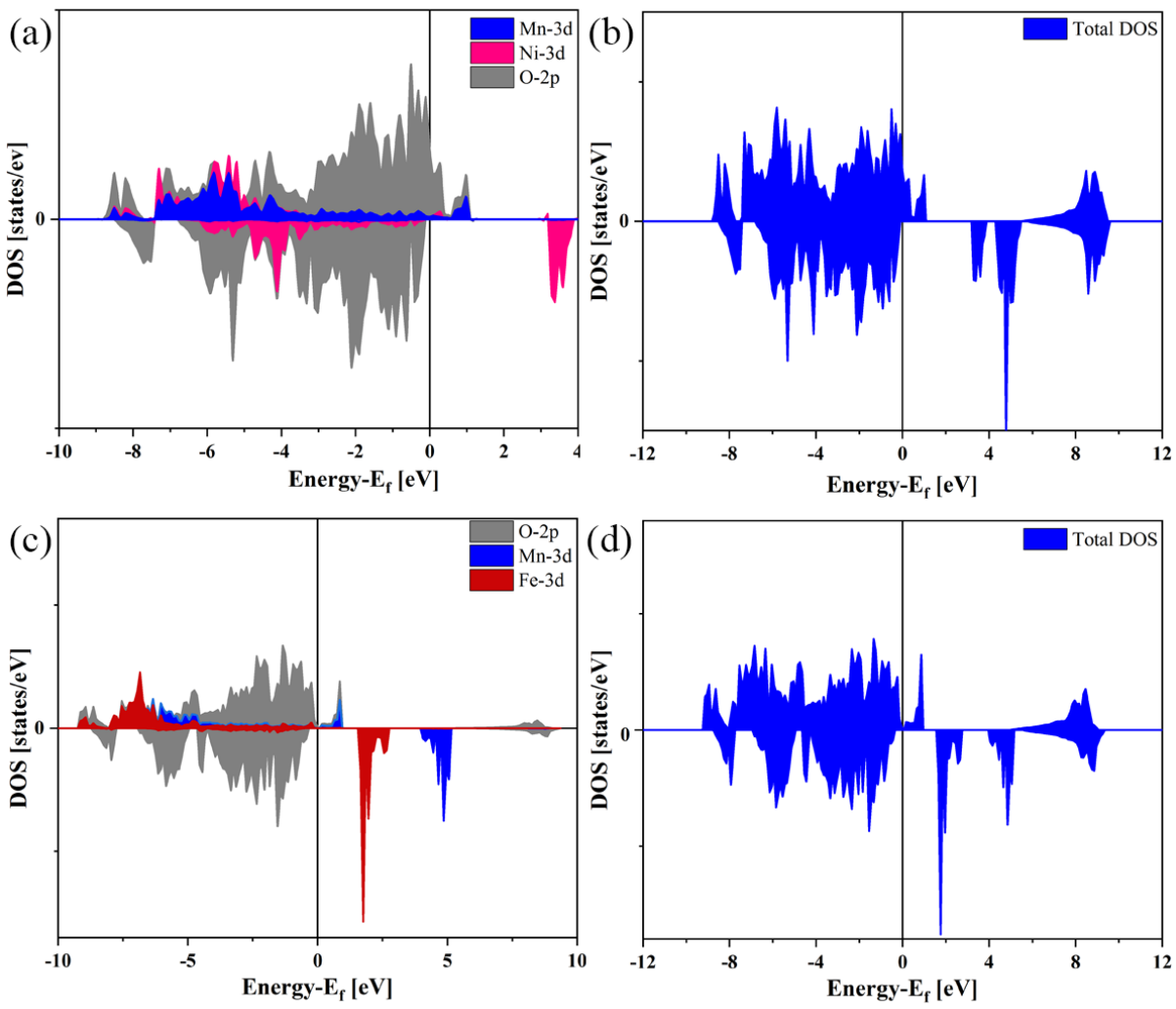

Figure 3.5: Projected DOS of (a) $Mn_{0.5}Ni_{0.5}PO_4$ (MNP), (c) $Mn_{0.5}Fe_{0.5}PO_4$ (MFP) and total DOS of (b) $Mn_{0.5}Ni_{0.5}PO_4$ and (d) $Mn_{0.5}Fe_{0.5}PO_4$.

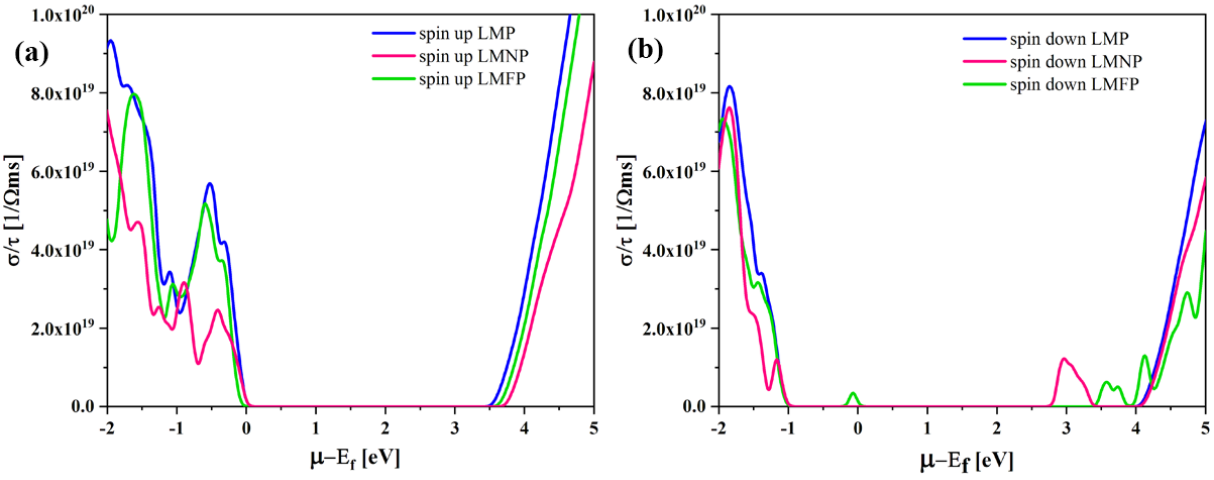

Figure 3.6: The electrical conductivity of LMP, LMNP and LMFP for both spins (a) up and (b) down.

From Figure 3.6, it can be seen that the electrical conductivity in the p-type region (negative chemical potential) and n-type region (positive chemical potential) is mainly due to spin up for LMP, LMNP and LMFP. while the spin down of LMNP and LMFP contributes to the electrical conductivity at low chemical potential (at 2.9 and 3.4 eV for LMNP and LMFP, respectively). Moreover, the spin down peaks of conductivity in the n-type region at low values of chemical potential with Ni/Fe substitution could be explained by the decreasing of band gap from 3.62 to 2.77 eV (3.35 eV) for LMNP (LMFP). The appearance of electrical conductivity in the low chemical potentials for LMNP and LMFP can be beneficial for cathode materials of Li-ion batteries.

During the substitution of Mn by Ni and Fe in LMP structure, the total magnetization decreases from 20 to 8 μ_b and from 20 to 16 μ_b with increasing the amount of Ni and Fe substitutions, respectively as shown in Figure 3.7. This decrease can be explained by the atomic magnetic moments of Ni and Fe being smaller compared to that of Mn. (magnetic moments of Mn is 4.26 μ_b > 3.45 μ_b for Fe > 1.73 μ_b for Ni).

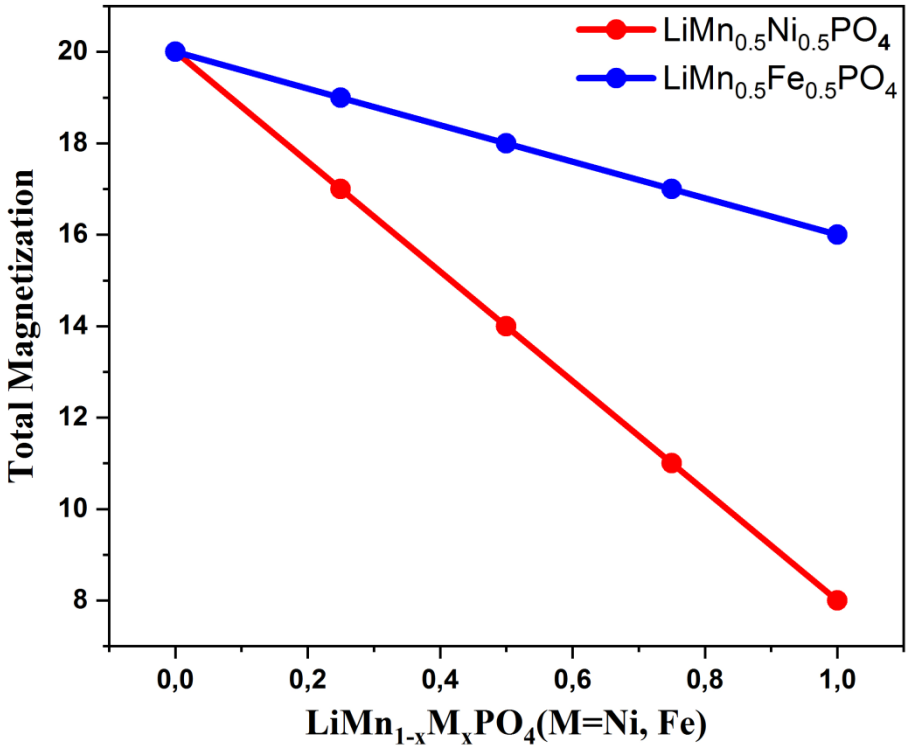

Figure 3.7: Total magnetization of $LiMn_{1-x}M_xPO_4$ (M=Ni, Fe).

3.3.3 Specific capacity and Li intercalation voltage

The Li intercalation voltage and the theoretical specific capacity are among the characteristic

quantities that determine the performance of the LIBs. In this context, we calculated the open circuit voltage (OCV) and the theoretical capacity of $LiMn_{1-x}M_xPO_4$ (M=Ni, Fe; x=0, 0.25, 0.5, 0.75, 1). To calculate the Li intercalation voltage for these materials, we used the following expression [12, 147]

$$V = -\frac{E(LiMn_{1-x}M_xPO_4) - E(Mn_{1-x}M_xPO_4) - E(Li)}{e} \quad (3.2)$$

Where $E(LiMn_{1-x}M_xPO_4)$ and $E(Mn_{1-x}M_xPO_4)$ represent the total energy of the lithiated and delithiated states, respectively. E(Li) denotes the energy of Li in the bcc structure and *e* stands for the absolute electron charge.

As shown in Figure 3.8b (red curve), the open circuit voltage (OCV) of $LiMn_{1-x}Ni_xPO_4$ exhibits a slight increase compared to that of the pristine LMP, so that the OCV of $LiMn_{1-x}Ni_xPO_4$ increased from 4.39 V (for LMP) to 4.41 V (for $LiMn_{0.25}Ni_{0.75}PO_4$). The same effect of Ni on LMP was reported in the experimental study of Ottmann et al. [140].

On the other hand, it can be observed that the OCV decreases from 4.39 V (for LMP) to 3.57 V (for $LiMn_{0.75}Fe_{0.25}PO_4$) and then remains constant for $LiMn_{0.5}Fe_{0.5}PO_4$, $LiMn_{0.25}Fe_{0.75}PO_4$ and LFP as shown in Figure 3.8b (blue curve). This behavior suggests that Fe^{2+} reduces the polarization of $LiMnPO_4$ during cycling as pointed out by Ting-Feng Yi et al. in their experimental results [141]. In addition, T. Muraliganth and A. Manthiram have showed experimentally that there is a systematic shift in the redox potential (OCV) of Mn^{2+}/Mn^{3+} couples in $LiM_{1-y}M_yPO_4$ (Mn, Fe and Co) compared to the pristine LMP [148]. They suggested that, the difference in electronegativity between the transition metals is the crucial factor that governs this behavior of OCV.

In order to calculate the theoretical capacity, we used the Eq. 3.1. The theoretical capacity of $LiMn_{1-x}M_xPO_4$ (M=Ni, Fe; x=0, 0.25, 0.5, 0.75, 1) is plotted in Figure 3.8c. We can observe from this figure that the theoretical capacity slightly decreases with increasing both Ni and Fe concentrations, indicating that the capacity is not strongly altered by the substitution of Mn by Ni or Fe. For example, the relative change of capacity is 1.80% between pure LMP and $LiMn_{0.25}Ni_{0.75}PO_4$ and 0.50 % (0.08%) between LMP (LFP) and $LiMn_{0.25}Fe_{0.75}PO_4$.

The capacity behavior can be attributed to the difference in molar mass of each compounds, for instance M (LMP) = 156.85 g/mol < M (LMNP) = 158.73 g/mol, and M (LMP) = 156.85

g/mol <M ($LiMn_{0.75}Fe_{0.25}PO_4$) = 157.07 g/mol < M (LMFP) = 157.30 g/mol < M ($LiMn_{0.25}Fe_{0.75}PO_4$) = 157.53 g/mol < M (LFP) = 157.76 g/mol.

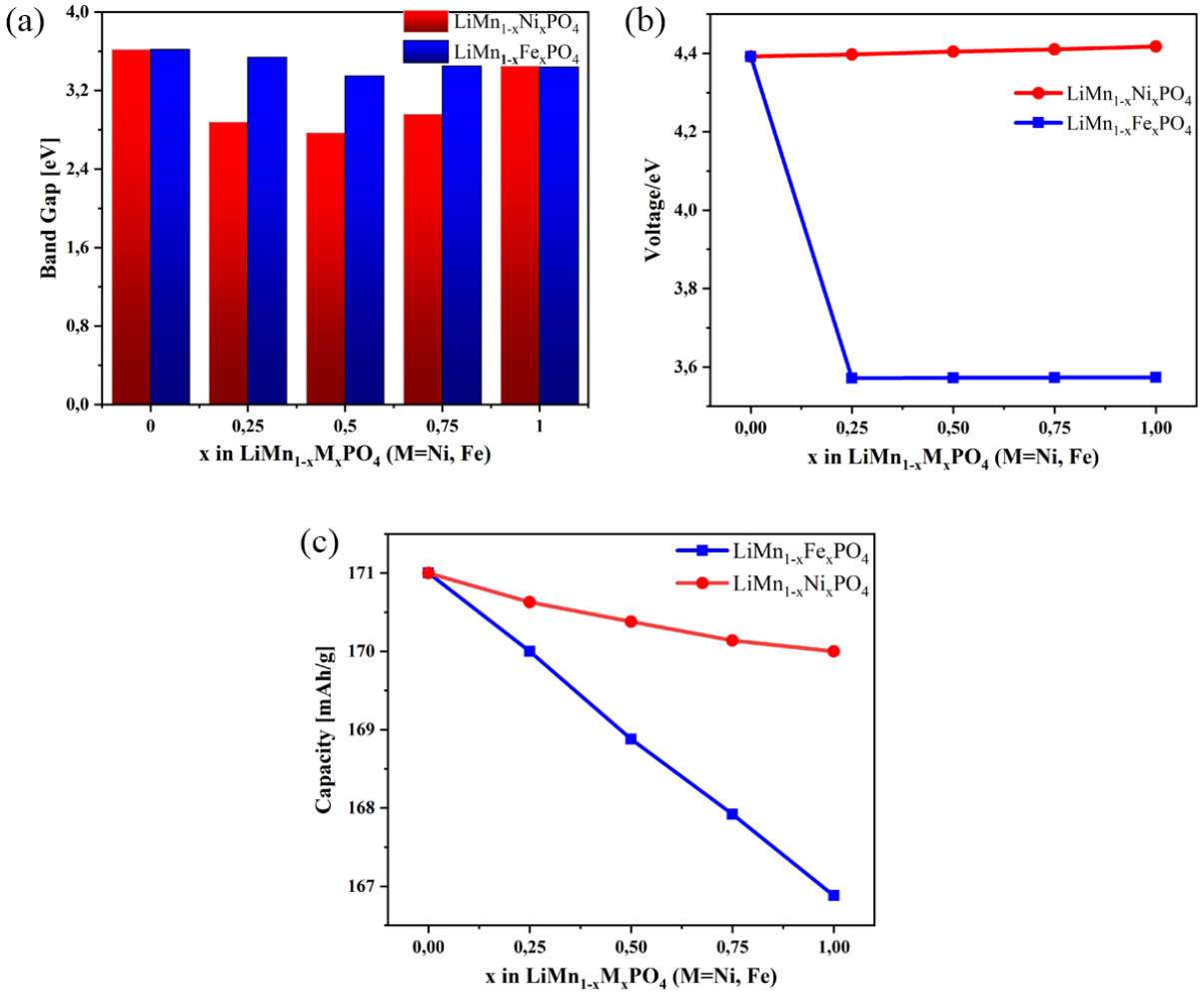

Figure 3.8: (a) Band Gap, (b) voltage and (c) capacity of $LiMn_{1-x}Ni_xPO_4$ (red curve) and $LiMn_{1-x}Fe_xPO_4$ (blue curve).

3.3.4 Li-ion diffusion barrier

Diffusion of Li-ion in electrode materials is one of the crucial factors that can define the electrochemical performance of rechargeable LIBs. In order to understand the effect of ion doping on the kinetic properties of pure LMP, Li^+-diffusion in $MnPO_4$, $Mn_{0.5}Ni_{0.5}PO_4$ and $Mn_{0.5}Fe_{0.5}PO_4$ and the corresponding activation energies were investigated using the nudged elastic band (NEB) method. A single Li-ion was introduced in $MnPO_4$, $Mn_{0.5}Ni_{0.5}PO_4$ and $Mn_{0.5}Fe_{0.5}PO_4$ supercells, and seven images were built to interpolate the diffusion path.

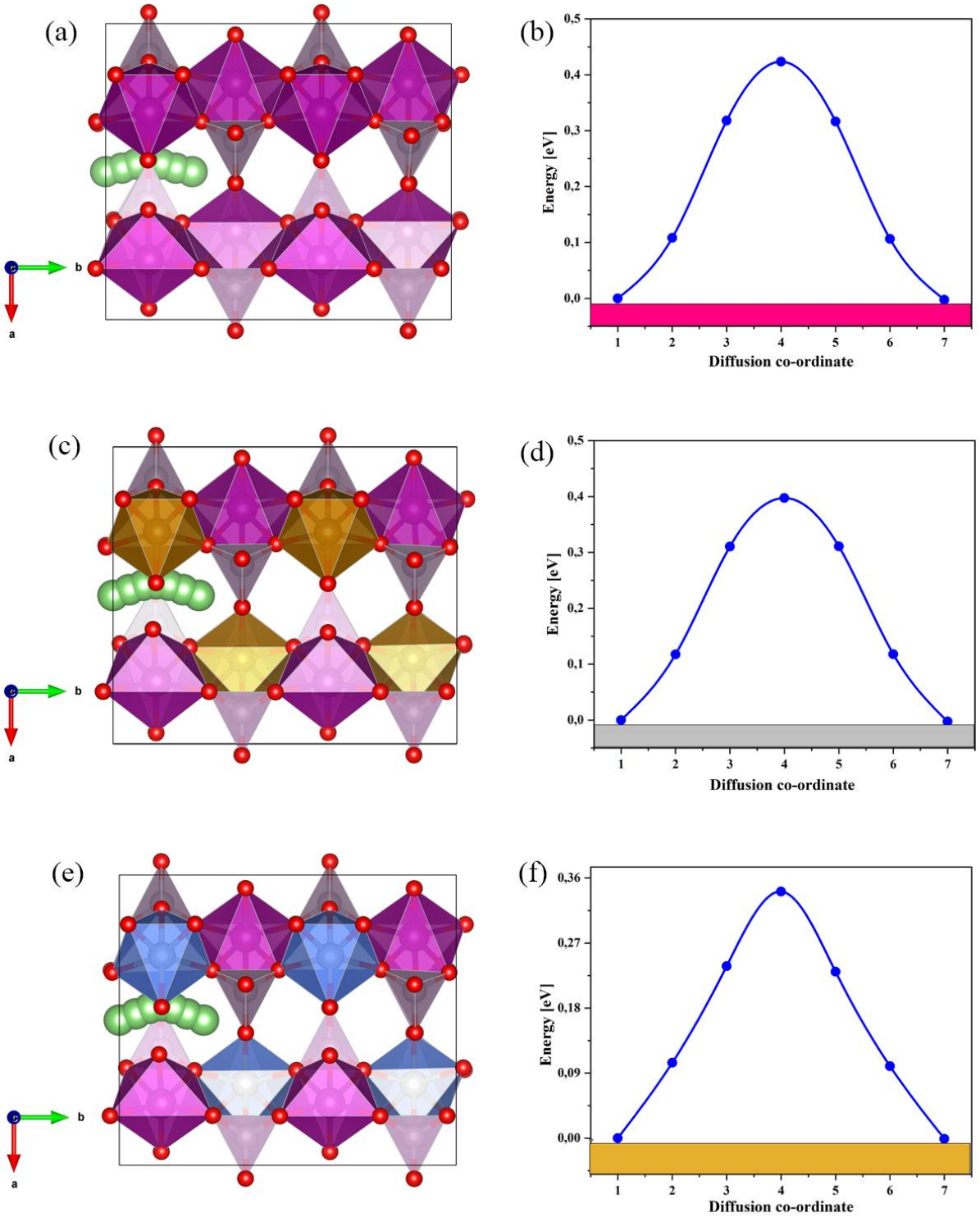

Figure 3.9: Li-ion migration paths in (a) $MnPO_4$, (c) $Mn_{0.5}Fe_{0.5}PO_4$ and (e) $Mn_{0.5}Ni_{0.5}PO_4$. The energy profiles of lithium ion diffusion in (b) $MnPO_4$, (d) $Mn_{0.5}Fe_{0.5}PO_4$ and (f) $Mn_{0.5}Ni_{0.5}PO_4$.

It is well-know that Li^+ diffusion pathway is located in the 1D channel along the b-axis in the olivine structures [149]. Figure 3.9b, d and f show the energy profiles in $MnPO_4$, $Mn_{0.5}Fe_{0.5}PO_4$ and $Mn_{0.5}Ni_{0.5}PO_4$ and their Li^+ diffusion pathways in Figure 3.9a, c and e

respectively. It can be observed that the diffusion barrier of Li-ion in $MnPO_4$ is 0.42 eV, this value is very close to those values reported by previous studies for example 0.429 eV [27] and 0.44 eV [134], and the diffusion barrier of Li^+ in $Mn_{0.5}Ni_{0.5}PO_4$ and $Mn_{0.5}Fe_{0.5}PO_4$ are 0.34 eV and 0.39 eV, respectively. These values indicate that the diffusion barrier of Li-ion in $MnPO_4$ is higher than that in $Mn_{0.5}Ni_{0.5}PO_4$ and $Mn_{0.5}Fe_{0.5}PO_4$.

From these energies profiles it can be deduced that substituting 50% of Mn in LMP with Ni or Fe is beneficial to improve the ionic conductivity of $MnPO_4$ to some extent, and then to improve the kinetic properties of LMP as cathode material in LIBs. To better understand this improvement, the diffusion coefficients were estimated using the Arrhenius equation [150]:

$$D \sim e^{\frac{-E_a}{K_B T}} \tag{3.3}$$

Where, E_a, K_B and T are the barrier energy, Boltzmann constant and the standard temperature, respectively.

The diffusion coefficients of MNP and MFP are respectively 3 and 8 times higher than that of MP, indicating that Li^+ could diffuse more easily in MNP and MFP compared to pristine MP. This decrease in the barrier energy value for $Mn_{0.5}Ni_{0.5}PO_4$ and $Mn_{0.5}Fe_{0.5}PO_4$ can be attributed to the various repulsive Li-M (M = Mn, Fe) and M-M interactions [151].

3.4 Chapter Summary

Density functional theory (DFT) calculations were used to investigate the structural, electronic, magnetic (total magnetization), electrochemical potential and kinetic properties of lithiated/delithiated ($LiMn_{1-x}M_xPO_4$ / $Mn_{1-x}M_xPO_4$ (M= Ni, Fe; x=0, 0.25, 0.5, 0.75, 1)) phases. The main results can be summarized as follows:

1. The results suggest that $LiMnPO_4$ (LMP) volume is decreased with increasing concentrations of Ni and Fe in Mn sites. Moreover, the band gap (E_g) of LMP (3.62 eV) is reduced with substitutions of Mn sites by Ni and Fe, especially for the compounds $LiMn_{0.5}Ni_{0.5}PO_4$ (LMNP) (2.77 eV) and $LiMn_{0.5}Fe_{0.5}PO_4$ (LMFP) (3.35 eV) and then the electronic conductivity is increased.
2. The diffusion barrier of Li-ion in $Mn_{0.5}Ni_{0.5}PO_4$ and $Mn_{0.5}Fe_{0.5}PO_4$ was calculated to be 0.34 eV and 0.39 eV respectively which is lower than pristine $MnPO_4$ (0.42 eV).

Indicating that 50% of Ni and Fe are beneficial to improve the kinetic properties in LMP.

3. The calculations revealed that Fe and Ni form a stronger bond length with O than Mn, which signifies a good improvement in the structural stability of the doped LMP structures.

Overall this study suggests that LMNP and LMFP could be great alternatives for $LiMnPO_4$ (LMP), $LiNiPO_4$ (LNP) and $LiFePO_4$ (LFP) as cathode materials of LIBs due to their good performances and abilities to overcome the main problems of olivines materials (ionic and electronic conductivity).

Chapter 4

Ni-Fe co-doping to enhance the performance of $LiMnPO_4$ as cathode materials for Li-Ion Batteries

4.1 Background

LiMnPO4 (LMP) has attracted significant attention as a potential cathode material for Li-ion rechargeable batteries due to its series of advantages such as good stability, environmental friendliness, low cost and maximum energy density (700 Wh.kg-1) [17, 18], which suggests that LMP is a promising candidate cathode material for LIBs. However, LMP suffers from low electronic and ionic conductivities which reduces its efficiency as a cathode material [19, 20]. To overcome these constraints, numerous methods such as coating LMP with carbon (C) [21], reducing its crystal size [22], and cation doping have been used [152].

Recently, the substitution of Mn-atoms in the LMP structure with other transition metals has been considered to be an effective method to enhance the electrochemical performance of LMP as shown by several experimental and theoretical studies, as presented in **chapter 3**.
Although the significance of single-doping to enhance the electrochemical activity of LMP, co-doping can further enhance the electrochemical performance of LMP as reported by several studies: Yi et al. synthesized $LiMn_{0.9}Fe_{0.1-x}Zn_xPO_4/C$ (x=0, 0.05, and 0.1) composites by a solid-state process, and they concluded that the Fe-Zn-co-doped ($LiMn_{0.9}(FeZn)_{0.05}PO_4/C$) exhibits a better rate capability and a higher discharge capacity compared to Fe/Zn single-doped material [80]. Huang et al. prepared LMP/C, $LiMn_{0.85}Fe_{0.15}PO_4/C$, $LiMn_{0.92}Ti_{0.08}PO_4/C$ and $Li(Mn_{0.85}Fe_{0.15})_{0.92}Ti_{0.08}PO_4/C$ by a solid-state reaction route and characterized them by X-ray diffraction, X-ray photoelectron spectroscopy, scanning electron microscopy, and electrochemical tests, and they revealed that Ti^{4+} and Fe^{2+} co-doping at the Mn site is a successful method to ameliorate the electrochemical properties of LMP [153]. Ramar and Balaya reported that co-doped ($LiMn_{0.9}Fe_{0.05}Mg_{0.05}PO_4/C$) exhibited a better lithium-storage capacity (159 $mAh.g^{-1}$) compared to the single-doped $LiMn_{0.9}Fe_{0.1}PO_4/C$ (136.8 $mAh.g^{-1}$) and $LiMn_{0.95}Mg_{0.05}PO_4/C$ (128.4 $mAh.g^{-1}$) at 0.1 °C, respectively [154].

To the best of our knowledge, the effect of Ni–Fe co-doping on the pristine LMP has not been studied yet in the literature. Therefore, the present study aims to investigate the structural, electronic, magnetic, Li intercalation voltage and kinetic properties of Ni-Fe co-doping in lithiated/delithiated pristine phases ($LMn_{0.5}Ni_{0.25}Fe_{0.25}PO_4/Mn_{0.5}Ni_{0.25}Fe_{0.25}PO_4$) besides the thermodynamic stability, theoretical capacity, charge transfer, average M–O bond lengths and electrical conductivity based on density functional theory (DFT) calculations.

4.2 Computational details

The structural and electronic calculations were carried out using DFT within the projector augmented wave method as implemented in the Quantum Espresso code [108, 104, 155]. The exchange-correlation energies were described using the generalized gradient approximation (GGA) with the Perdew–Burke–Ernzerhof functional that is the adapted version for solid-state systems (PBEsol) [155]. The lattice parameters and atomic positions were relaxed with the Broyden_Fletcher-Goldfarb-Shanno (BFGS) algorithm [129], until the forces, total energy and stress became smaller than 10^{-4} Ry/Bohr, 1×10^{-6} Ry and 0.01 kbar, respectively. A cutoff energy of 88 Ry was selected to determine the sufficient size of plane waves to expand the Kohn-Sham orbitals. The Brillouin zone was sampled using a 4 × 5× 6 k-point. The Marzari-Vanderbilt-smearing method was used for the density of states (DOS) calculation with a degauss of 0.01 Ry [156]. Moreover, the Hubbard (U) correction was optimized to be U = 4.5, 5.5 and 3.5 eV for Mn, Ni and Fe, respectively to treat the strong correlation of d-electron orbitals in transition metals [128]. The electrical conductivity was calculated by BoltzTrap code that is based on the resolution of the Boltzmann transport equation [145].

For evaluating the theoretical capacity of the olivine structure, we have used the following equation [131]:

$$C(mAhg^{-1}) = \frac{n \times F}{M_w} \tag{4.1}$$

where n, M_w, and F are the number of Li in the lithiated phase, the molecular weight of the compound, and the Faraday constant, respectively. The Li average binding energy and Li intercalation voltage can be calculated by the following equations [12, 147].

$$E_b = -\frac{E\left(Li_{x_2}Y\right) - E\left(Li_{x_1}Y\right) - (x_2 - x_1)E(Li)}{(x_2 - x_1)} \quad (4.2)$$

$$V = -\frac{E\left(Li_{x_2}Y\right) - E\left(Li_{x_1}Y\right) - (x_2 - x_1)E(Li)}{(x_2 - x_1)e} \quad (4.3)$$

Wherein, $E\left(Li_{x_2}Y\right)$ and $E\left(Li_{x_1}Y\right)$ represent the total energy of the system with x_2 and x_1 Li-concentration, respectively, E(Li) represents the energy of Li in the bcc structure and e stands for the absolute electron charge.

Besides, the thermal stability of lithiated and delithiated phases (LMNFP/MNFP) was examined using ab-initio molecular-dynamics (AIMD) simulations with a simulation time of 4000 steps of 0.5 fs at standard temperature within the canonical ensemble (NVT). In order to locate the transition state and extract the Li-ion migration barrier, we performed the nudged elastic band (NEB) method, as implemented within the Quantum Espresso code [130]. 1 × 2 × 2 supercells containing 16 formula units up to 112 atoms were selected for minimizing the interaction between the periodic images of the diffused Li-ion.

In addition to theoretical capacity and Li intercalation voltage, the diffusion coefficient (D) was also estimated using the transition state theory [157] through

$$D = l^2 \vartheta_0 exp(-\frac{E_{act}}{k_B T}) \quad (4.4)$$

where l is the hopping length, while ϑ_0 is the vibrational frequency of the Li atom in the lattice, which is $\vartheta_0 \sim 10^{12}$ Hz [158]. E_{act}, k_B and T are the barrier energy, Boltzmann constant and standard temperature, respectively.

Since the energy difference between ferromagnetic (FM) and antiferromagnetic states of olivine structures are negligible [132], we performed all calculations with a ferromagnetic (FM) order. This approach was previously used in several studies [63, 134]. All visualizations were performed using VESTA software [109].

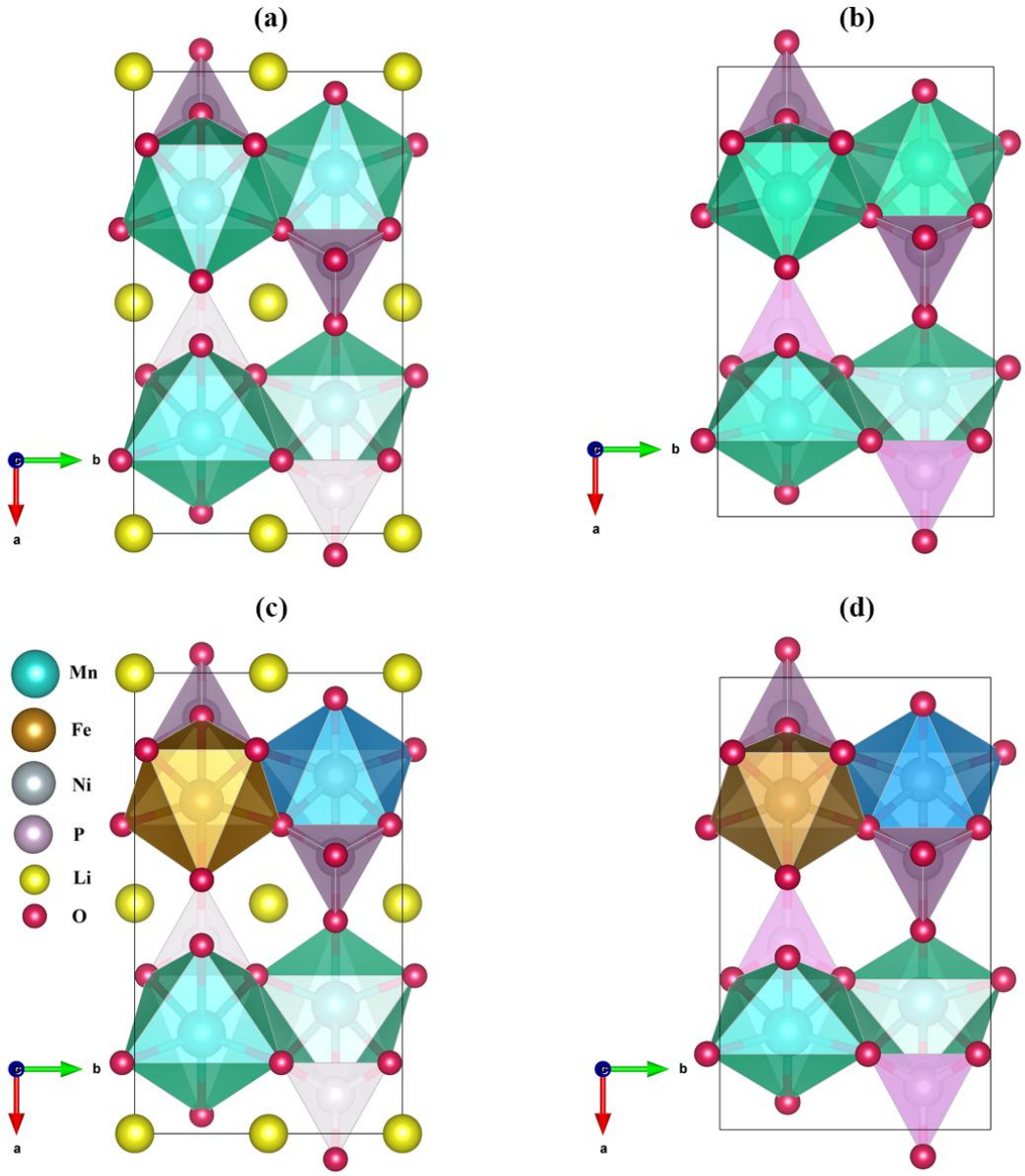

.**Figure 4.1:** Crystallographic structures of (a) LMP, (b) MP, (c) LMNFP and (d) MNFP. Green, brown and blue colors stand for MnO_6, FeO_6 and NiO_6 octahedral units, respectively.

4.3 Results and Discussion

4.3.1 Crystal Structure

Olivine-type structure LMP/$MnPO_4$ (lithiated/delithiated phase) has an orthorhombic unit cell containing four units with a space group of *Pnma* (number 62). The relaxed structure of LMP, $MnPO_4$ (MP), LMNFP, and $Mn_{0.5}Ni_{0.25}Fe_{0.25}PO_4$ (MNFP) are shown in Figure 4.1a–d respectively. The oxygen atoms form an octahedral arrangement around each M-atom (MO_6) (wherein M= Mn, Ni, and Fe), this octahedral state has four categories of bonds (M–Oi; I = 1, 2, 3, and 3′), where M–O1, M–O2 and M–O3, M–O3′ are in the axial and equatorial plane.

On the other hand, each P-atom is surrounded by O-atoms with a tetragonal arrangement (PO_4). This construction creates channels along the b-axis which allows the diffusion and storage of Li-ions. The relaxed lattice parameters and unit cell volumes of lithiated/delithiated phases of pristine (LMP/MP), Ni single-doping [LMNP/$Mn_{0.5}Ni_{0.5}PO_4$(MNP)], Fe single doping [LMFP/$Mn_{0.5}Fe_{0.5}PO_4$(MFP)] and Ni–Fe codoping (LMNFP/MNFP) are listed in Table 4.1. The results are in agreement with available theoretical and experimental results, the differences between the calculated and the experimental volume are only 1.13 and 1.98% for LMP and LMFP, respectively, indicating the reliability of our computations with the DFT + U approach.

In Table 4.1, it can be observed that the unit cell volumes of pristine LMP and MP were reduced with Ni or Fe single doping and Ni–Fe codoping, this reduction can be attributed to the smaller ionic radius of Ni^{2+} (0.69 Å) and Fe^{2+} (0.78 Å) compared to Mn^{2+} (0.83 Å). A similar effect of Ni or Fe single doping on the unit cell volume of pristine LMP has been reported experimentally by Ottmann et al [140]. and Yi et al [141]. The calculated α and γ angles remain constant with single doping and codoping in LMP, while the β angles slightly changed from $90°$ to $89.89°, 89.90°, 89.29°$ and $89.98°$ for LMFP, LMNFP, MFP, and MNFP, respectively. These results indicate that the symmetry of LMP is conserved with Ni single doping, while Fe single-doping, and Ni–Fe codoping slightly affect the β angle. This may be attributed to the small distortion in the ac plane (perpendicular to the b-axis) caused by the radius mismatch between Mn and the solute atoms (Ni, and Fe).

The change in unit volume during Li-ion extraction is approximately 4.5, 6.3, 6, and 7.2% for LMP, LMNP, LMFP, and LMNFP, respectively [127, 159]. Such a small volume change (less than 7.3%) between lithiated/delithiated phases is generally required to obtain good cycling stability of these compounds leading to a long life cycle during Li insertion/extraction. For a better understanding of the volume change, we have investigated the metal–oxygen bond lengths in all structures (see Table 4.2); the majority of the M–Oi bond lengths tighten with oxidation of the metal ion (M^{2+}/M^{3+} for lithiated/delithiated) which reflects the shrinking volume in the delithiated phases, whereas Mn–O3 in LMP and LMFP and Ni–O3 in LMNFP were elongated due to Jahn-Teller distortions of MnO6 and NiO6 in these structures after Li-ion extraction [126, 160]. Most of the average Mn–O bond lengths of lithiated compounds are shortened to a certain extent compared to that of Mn–O in pure LMP, indicating that single doping and co-doping can build a stronger Mn–O bond. This strong bond can reduce the lattice distortion and improve the structural stability of LMP; as a result, Ni–Fe codoping can

enhance the structural stability and moderate the John–Teller effect of pristine LMP.

Table 4.1: Formation Energy and Optimized Lattice Parameters for LMP, LMNP, LMFP, and LMNFP and Their Delithiated Phases MP, MNP, MFP, and MNFP Respectively.

Compounds	a(Å)	b(Å)	c(Å)	V(Å^3)	Formation Energy (eV/atom)	Angles
MP	**9.85**	**6.05**	**4.90**	**292.00**	**-3.15**	
Cal.[14]	**9.90**	**6.06**	**4.93**	**295.77**		
Exp.[138]	**9.69**	**5.93**	**4.78**	**274.67**		$\boldsymbol{\alpha = 90}$ $\boldsymbol{\beta = 90}$ $\boldsymbol{\gamma = 90}$
LMP	**10.54**	**6.14**	**4.74**	**306.75**	**-3.34**	
Cal.[137]	**10.55**	**6.13**	**4.78**	**309.13**		
Exp.[10]	**10.45**	**6.11**	**4.75**	**303.28**		
MNP.[23]	**9.77**	**5.84**	**4.80**	**273.87**	**-2.67**	$\boldsymbol{\alpha = 90}$ $\boldsymbol{\beta = 90}$ $\boldsymbol{\gamma = 90}$
LMNP.[23]	**10.35**	**6.00**	**4.71**	**292.49**	**-2.99**	
MFP.[23]	**9.86**	**5.94**	**4.87**	**285.22**	**-2.96**	$\boldsymbol{\alpha = 90}$ $\boldsymbol{\beta = 89.29}$ $\boldsymbol{\gamma = 90}$
LMFP.[23]	**10.52**	**6.09**	**4.74**	**303.67**	**-3.13**	
Exp.[139]	**10.401**	**6.054**	**4.727**	**297.64**		$\boldsymbol{\alpha = 90}$ $\boldsymbol{\beta = 89.89}$
MNFP	**9.77**	**5.85**	**4.80**	**274.34**	**-2.82**	$\boldsymbol{\alpha = 90}$ $\boldsymbol{\beta = 89.98}$ $\boldsymbol{\gamma = 90}$
LMNFP	**10.39**	**6.03**	**4.72**	**295.71**	**-3.02**	
						$\boldsymbol{\alpha = 90}$ $\boldsymbol{\beta}$

Table 4.2: Calculated Bond Lengths and Average (M–Oi) Distance in Structures of LMP, LMNP, LMFP, and LMNFP and in Their Delithiated Phases MP, MNP, MFP, and MNFP, Respectively.

Compounds		LMP	MP	LMNP	MNP	LMFP	MFP	LMNFP	MNFP
Mn–O	O1	**2.284**	**1.938**	**2.293**	**1.941**	**2.288**	**1.928**	**2.286**	**1.909**
	O2	**2.173**	**1.933**	**2 .177**	**1.939**	**2 .171**	**1.905**	**2.170**	**1.906**
	O3	**2.296**	**2.354**	**2.285**	**2.235**	**2.306**	**2.349**	**2.279**	**2.242**
	O3	**2.296**	**2.354**	**2.285**	**2.235**	**2.306**	**2.349**	**2.279**	**2.242**
	O3′	**2.156**	**2.040**	**2.138**	**2.028**	**2.153**	**2.050**	**2.132**	**2.003**

	O3′	**2.156**	**2.040**	**2.138**	**2.028**	**2.153**	**2.050**	**2.132**	**2.003**
Average Mn–O distance		**2.226**	**2.109**	**2.219**	**2.067**	**2.229**	**2.105**	**2.213**	**2.050**
Ni–O	O1			**2.106**	**1.945**			**2.118**	**1.935**
	O2			**2.043**	**1.937**			**2.036**	**1.922**
	O3			**2.164**	**2.152**			**2.172**	**2.203**
	O3			**2.164**	**2.152**			**2.172**	**2.203**
	O3′			**2.088**	**2.060**			**2.090**	**2.072**
	O3′			**2.088**	**2.060**			**2.090**	**2.072**
Average Ni–O distance (Å)				**2.100**	**2.051**			**2.113**	**2.067**
Fe–O	O1					**2.253**	**1.956**	**2.187**	**1.936**
	O2					**2.139**	**1.935**	**2.110**	**1.926**
	O3					**2.254**	**2.158**	**2.239**	**2.115**
	O3					**2.254**	**2.158**	**2.239**	**2.115**
	O3′					**2.102**	**2.029**	**2.081**	**2.029**
	O3′					**2.102**	**2.029**	**2.081**	**2.029**
Average Fe–O distance (Å)						**2.184**	**2.044**	**2.156**	**2.025**

4.3.2 Charge transfer and stability

The charge density repartition plays a key role in shrinking the volume during Li-ion extraction. To this aim, charge density analysis was performed using Bader's topological partitioning scheme based on the charge densities generated by Quantum Espresso using the codes provided by Henkelman et al. [160, 111]. Table 4.3 shows the atomic charges of all atoms in both lithiated and delithiated phases. During the delithiation process in all compounds, the charge of oxygen atoms become less negative contrary to the cation atoms which become more positive. The loss of charge in O- and M-atoms indicates that the volumes of these ions decreased, which result in a shrinking behavior in the unit cell volume.

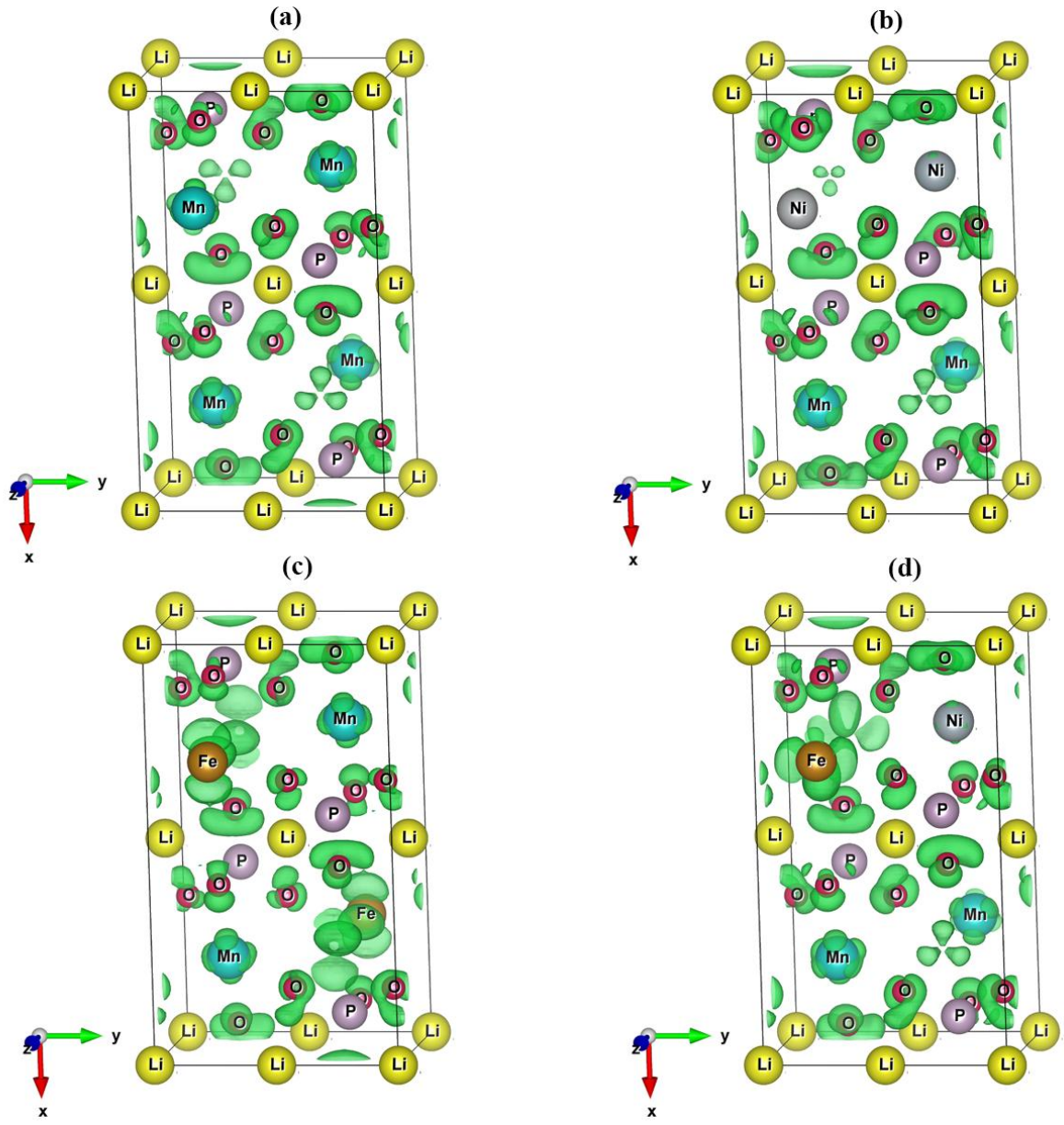

Figure 4.2: Three-dimensional plot of the charge density transfer during lithiation in (a) LMP, (b) LMNP, (c) LMFP, and (d) LMNFP with an isosurface of 0.006 e/Å3.

To better understand the charge transfer that occurs at the lithiation stage, the topological charge analysis was reported in Figure 4.2. A significant amount of charge density was observed around Mn, Fe, and O atoms, indicating a charge transfer from Li to Fe, Mn and O atoms, whereas Ni/P atoms gain an insignificant amount of charge. This observation is in line with Bader charge analysis, where Li has lost 0.89/0.89/0.90/0.89 e to Mn (0.23/0.24/0.24/0.26 e), Ni(—/0.05/—/0.04 e), Fe(—/—/0.43/0.42 e), P(0.05/0.00/0.01/0.00 e), O1(0.13/0.19/0.16/0.16 e), O2(0.21/0.22/0.16/0.18 e), and O3(0.14/0.17/0.12/0.15 e) for LMP/LMNP/LMFP/LMNFP, respectively. The charge transfers can be ascribed to the

electronegativity difference between Li and other elements. From these results, we confirm that the changes in cell volume with the extraction of lithium can be attributed also to charge-transfer processes mainly engrossing the oxygen atoms and metal ions (Mn and Fe) [134]. This charge transfer behavior between lithium and transition metal ion (Mn) in pristine LMP is in agreement with previously reported results by Mishima et al. and Osnis et al. [63, 161].

Table 4.3: Net Charges of Atoms in LMP, LMNP, LMFP, and LMNFP and Their Delithiated Phases MP, MNP, MFP, and MNFP, Respectively.

	net charge							
	Li	Mn	Ni	Fe	P	O1	O2	O3
LMP	**0.89**	**1.57**			**3.53**	**-1.48**	**-1.52**	**- 1.50**
MP		**1.80**			**3.58**	**-1.35**	**-1.31**	**- 1.36**
LMNP	**0.89**	**1.57**	**1.34**		**3.56**	**-1.49**	**- 1.49**	**-1.46**
MNP		**1.81**	**1.39**		**3.56**	**-1.30**	**- 1.27**	**-1.29**
LMFP	**0.90**	**1.57**		**1.47**	**3.57**	**-1.51**	**-1.50**	**- 1.49**
MFP		**1.81**		**1.90**	**3.58**	**-1.35**	**-1.34**	**- 1.37**
LMNFP	**0.89**	**1.57**	**1.34**	**1.47**	**3.56**	**-1.50**	**-1.48**	**-1.48**
MNFP		**1.83**	**1.38**	**1.89**	**3.56**	**-1.34**	**-1.30**	**-1.33**

In order to examine the thermodynamic stability, the formation energies of all compounds were calculated as [162]

$$E_f(X) = E_X - \sum_i n_i E_i \tag{4.5}$$

where, E_X refers to the total energies of lithiated/delithiated phases (LMP/MP, LMNP/MNP, LMFP/MFP and LMNFP/MNFP) and E_i are the total energies of different atoms (Li, Mn, Fe, Ni, P, and O) in their respective ground states, while n_i presents the number of each atom type in the unit cell. The formation energy of all compounds was calculated and is listed in Table 4.1. The results reveal that all structures possess negative formation energy, indicating their thermodynamic stability. It is worth noting also that the lithiated phases exhibit more negative formation energy compared to delithiated phases, which suggest good stability of

lithiated over the corresponding delithiated compounds. These results are in trend with several experimental studies which reported that LMP is thermodynamically stable above 400 °C or higher, and its delithated phase (MP) decomposes at a lower temperature ($\sim 200\ ^{\circ}C$) to release O_2 [163, 164] Moreover, in order to check the working of LMNFP as a cathode material at a standard temperature, the thermal stability of lithiated and delithiated phases is examined using AIMD. Figure 4.3 presents the total energy as a function of simulation time. It can be seen that the total energy of lithiated and delithiated phases fluctuates around 1 eV (35.71 meV/atom) validating the stability of these structures (LMNFP and MNFP). Furthermore, these structures exhibit good structural stability (without any bond breaking) with a small vibration of atoms around their equilibrium positions, which can be ascribed to the thermal agitation at 300 K. From these results, we can conclude the thermal stability of these phases at room temperature.

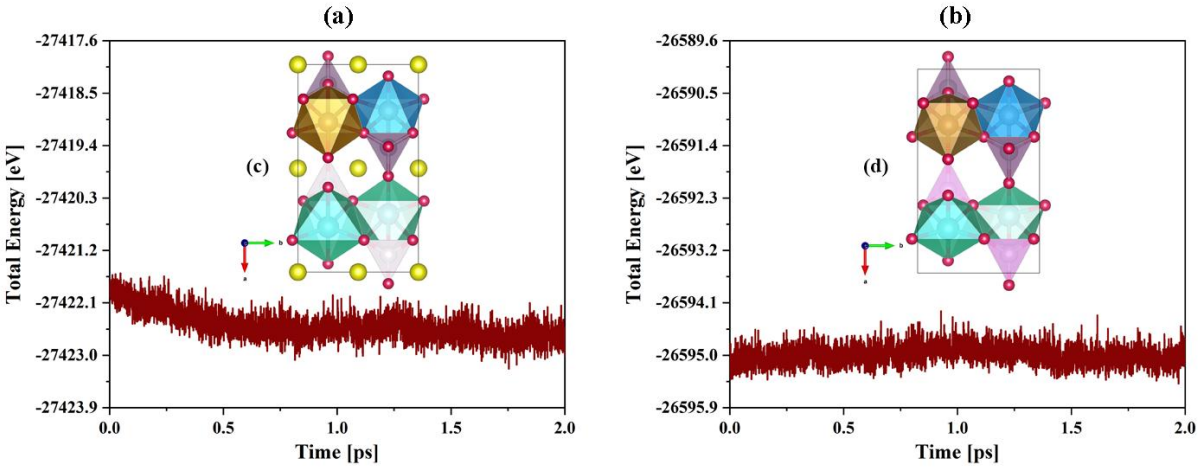

Figure 4.3: Total energy variation during a simulation of 2 ps at room temperature of (a) LMNFP and (b) MNFP. Snapshots of lithiated and delithiated structures of Ni–Fe co-doping at the end of MD simulation are inserted in both figures.

4.3.3 Electronic properties

The electronic property is a crucial factor for an efficient cathode material in LIBs. In this regard, the effect of Ni–Fe codoping on the electronic properties of LMP and MP structures was investigated through the DOS calculations. The total (TDOS) and partial DOS (PDOS) density of states for the pristine LMP have been plotted in Figure 4.4a,b. LMP shows a bandgap (E_g) of 3.62 eV; this value is in agreement with a previous study in the literature (3.75 eV) [62]. However, other studies have reported different Eg values. For example, Zhou et al. reported an Eg value of 3.8 eV using a Hubbard correction of U = 4.5 eV [124], while

Kellerman et al reported 3.11 eV for U= 2 eV [144]. This slight variation between these values can be attributed to the values of the Hubbard parameters (U) or to the used functional. Based on the PDOS curves, it can be seen that the valence band maximum is mainly composed of Mn-3d (spin-up) and O-2p (spins up and down) states and a small contribution of the Li-2s state. Meanwhile, the conduction band minimum (CBM) is mainly built from an unoccupied 3d-Mn (spin-down) state. Generally, the Mn ions are in a +2 oxidation state and a spin-up configuration, d-orbitals are full with spin-up electrons, generating a magnetic moment of $5\mu_B$. The magnetic moment value is in agreement with previous studies [125, 33].

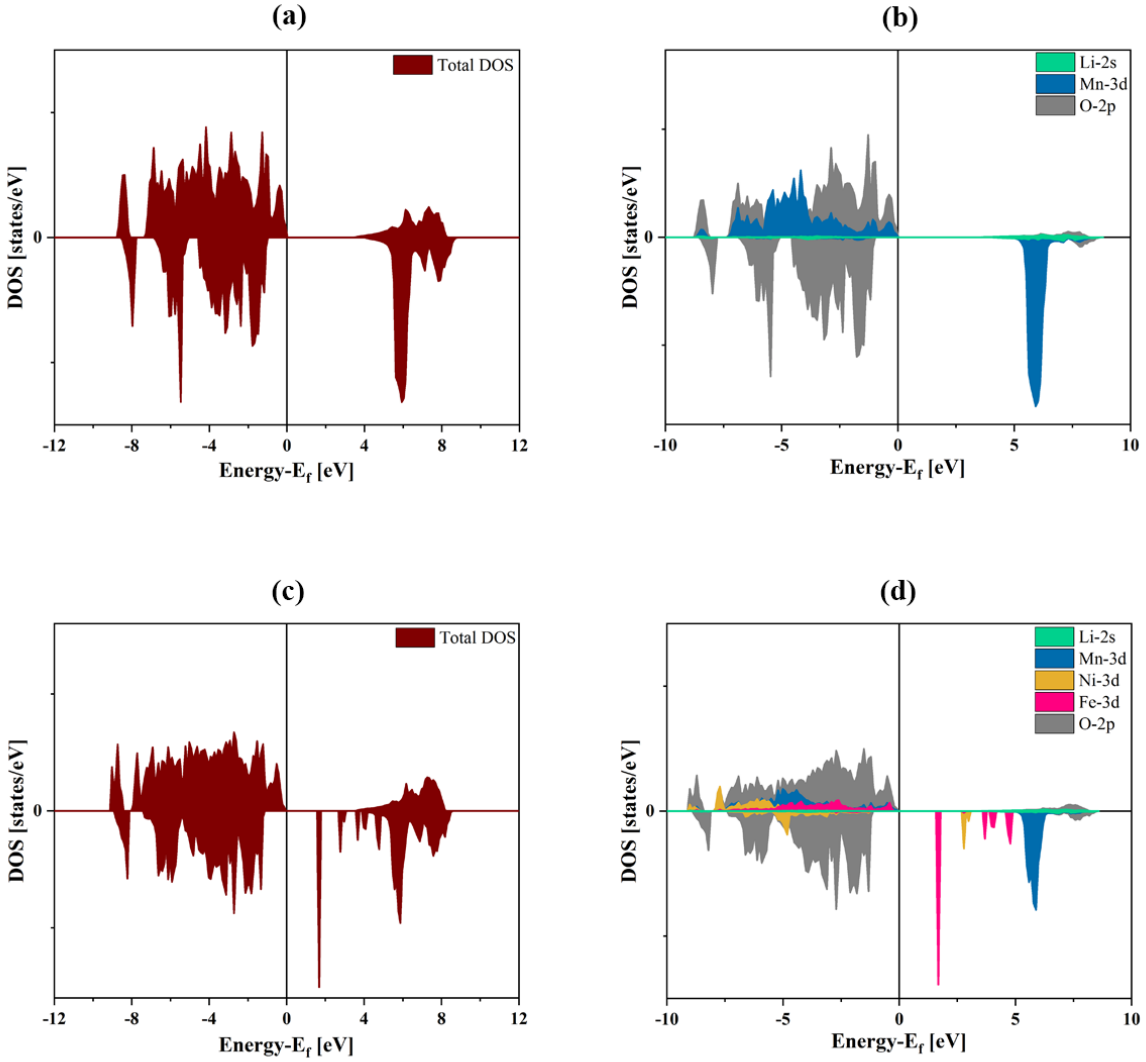

Figure4.4: Total DOS of (a) LMP and (c) LMNFP and projected DOS of (b) LMP and (d) LMNFP.

Figure 4.4c,d illustrates the TDOS and PDOS of Ni–Fe codoped LMP (LMNFP). It can be observed that Ni–Fe codoping generates a new electronic state derived from d-orbitals of the doping elements. The generated states reduce the band gap (E_g) of LMP from 3.62 to 1.55 eV

indicating that Ni–Fe co-doping can significantly improve the electronic conductivity of LMP compared to Ni/Fe single doping (E_g = 2.72/3.35 eV) (see Figure 4.5). Furthermore, LMNFP exhibits a semiconducting behavior, with a small bandgap compared to the commercial cathode material $LiFePO_4$ (Eg = 3.44 eV) [137]. The PDOS analysis disclosed that the VMB of LMNFP is mainly formed by O-2p and M-3d states. On the other hand, the CBM is mainly formed by M-3d states and a small contribution of O-2p states. Moreover, the spin-up states of transition metals are completely filled, while the spin-down states are empty except for those of Ni, which has spin-down states below the Fermi energy. The occupation behavior of M-3d states with spin-down electrons can be explained by the difference in electronic configuration between the different cations (5, 8 and 6 electrons for d-states of Mn^{2+}, Ni^{2+}, and Fe^{2+}, respectively).

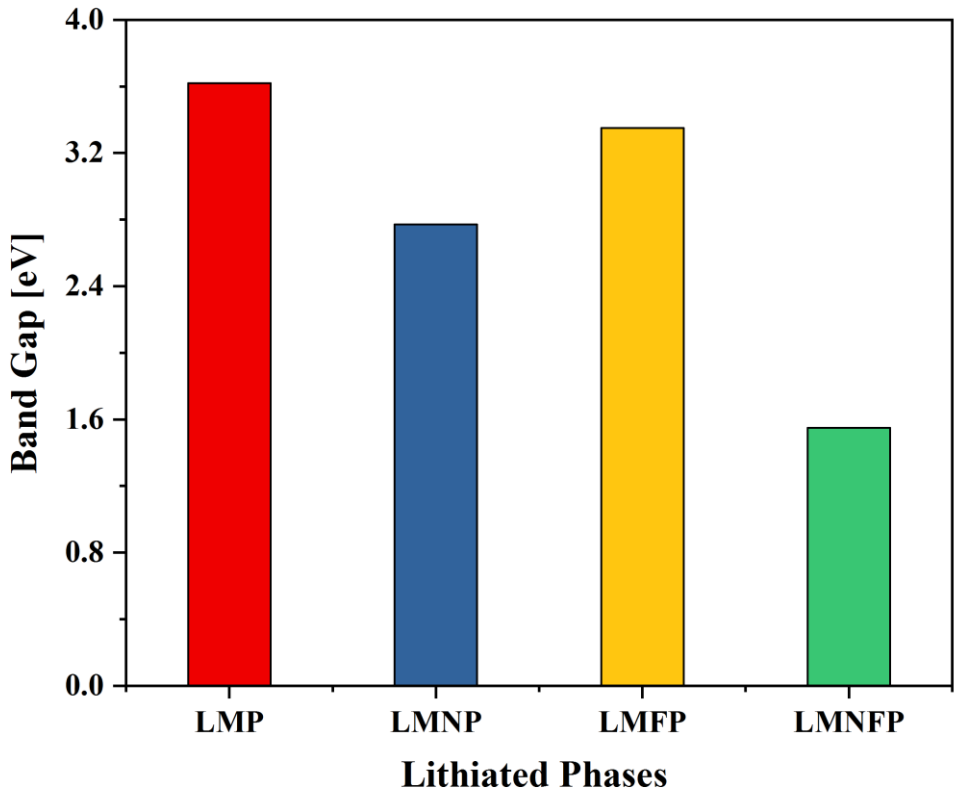

Figure 4.5: Band gap of LMNFP, LMNP, LMFP and LMP.

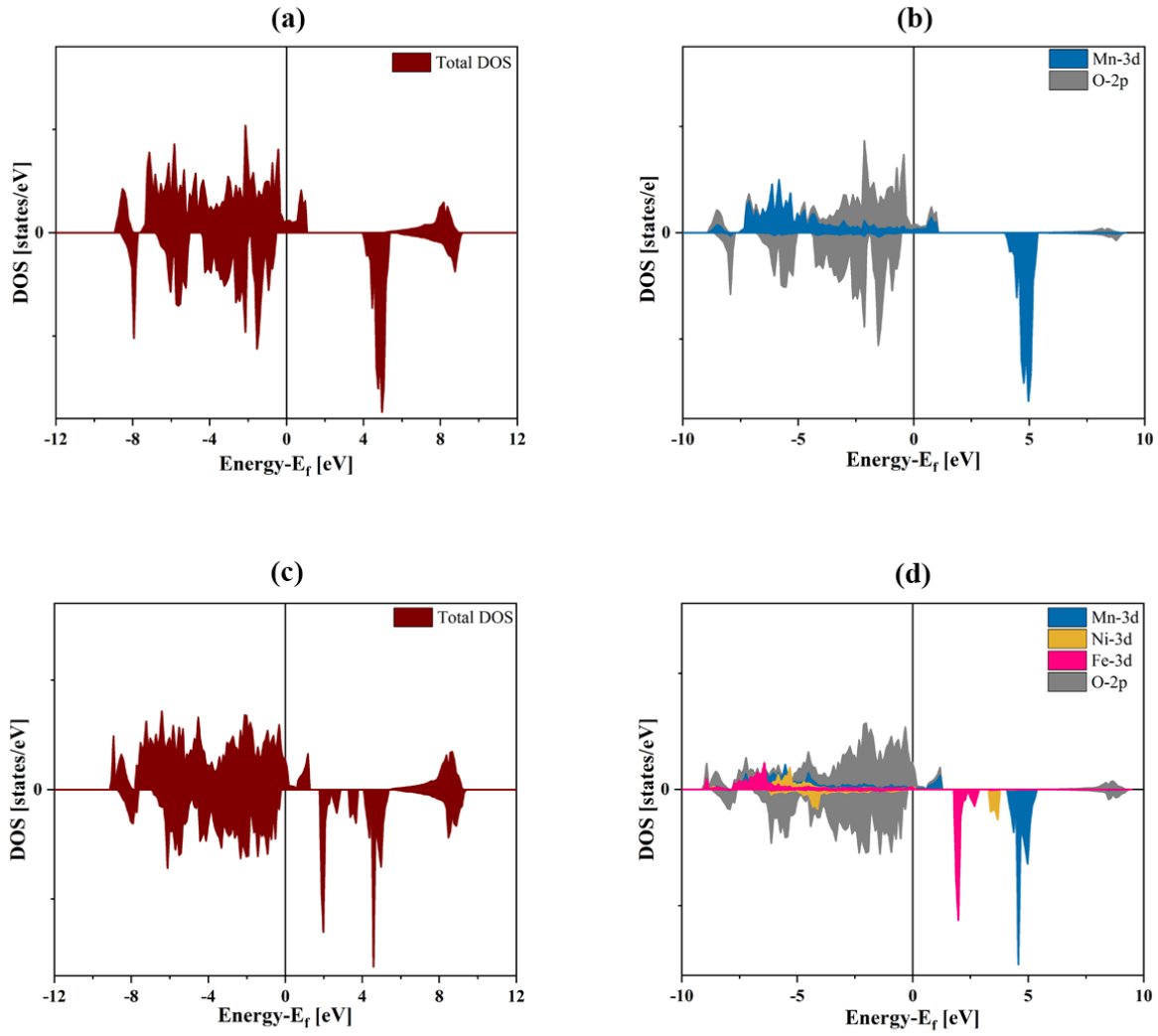

Figure 4.6: Total DOS of (a) MP and (c) MNFP and projected DOS of (b) MP and (d) MNFP.

Concerning the electronic properties of the delithiated phases (MP and MNFP), the PDOS and TDOS reveal a metallic behavior due to the shift of the Fermi energy level into the valence band, as shown in Figure 4.6a–d. This metallic behavior of the MP structure has been reported in other studies [27, 165]. For a better understanding of electronic mobility, we have investigated the electrical conductivity of all lithiated compounds as a function of chemical potential using the BoltzTrap code. The electrical conductivity of LMP, LMNP, LMFP and LMNFP as a function of chemical potential is plotted in Figure 4.7a,b. We can deduce that the spin-up is mainly responsible for the electrical conductivity in all materials, and spin-up states exhibit higher electrical conductivity compared to the spin-down states in both n-region (positive chemical potential) and p-region (negative chemical potential). The spin-down states of LMNFP, LMNP and LMFP contribute to the electrical conductivity at low chemical potentials, for example, the electrical conductivity could appear at 2.23 eV, 2.97 eV and 3.60

eV and reach $4.38 \times 10^{18}/\Omega ms$, $1.22 \times 10^{19}/\Omega ms$, and $6.25 \times 10^{18}/\Omega ms$ for LMNFP, LMNP, and LMFP, respectively. The shifting of conductivity region to a lower chemical potential value with Ni–Fe codoping and Ni/Fe single doping can be attributed to the decrease of the LMP band gap from 3.62 to 1.55, 2.72, and 3.35 eV for LMNFP, LMNP and LMFP, respectively [23, 166].

4.3.4 Specific capacity and Li intercalation voltage

In this section, we are going to investigate the effect of Ni–Fe co-doping on the theoretical capacity and open-circuit voltage of pure LMP, and we will compare its effect with the Ni and Fe single- doping that was already examined in [23]. Based on eq 4.1, the calculated capacity

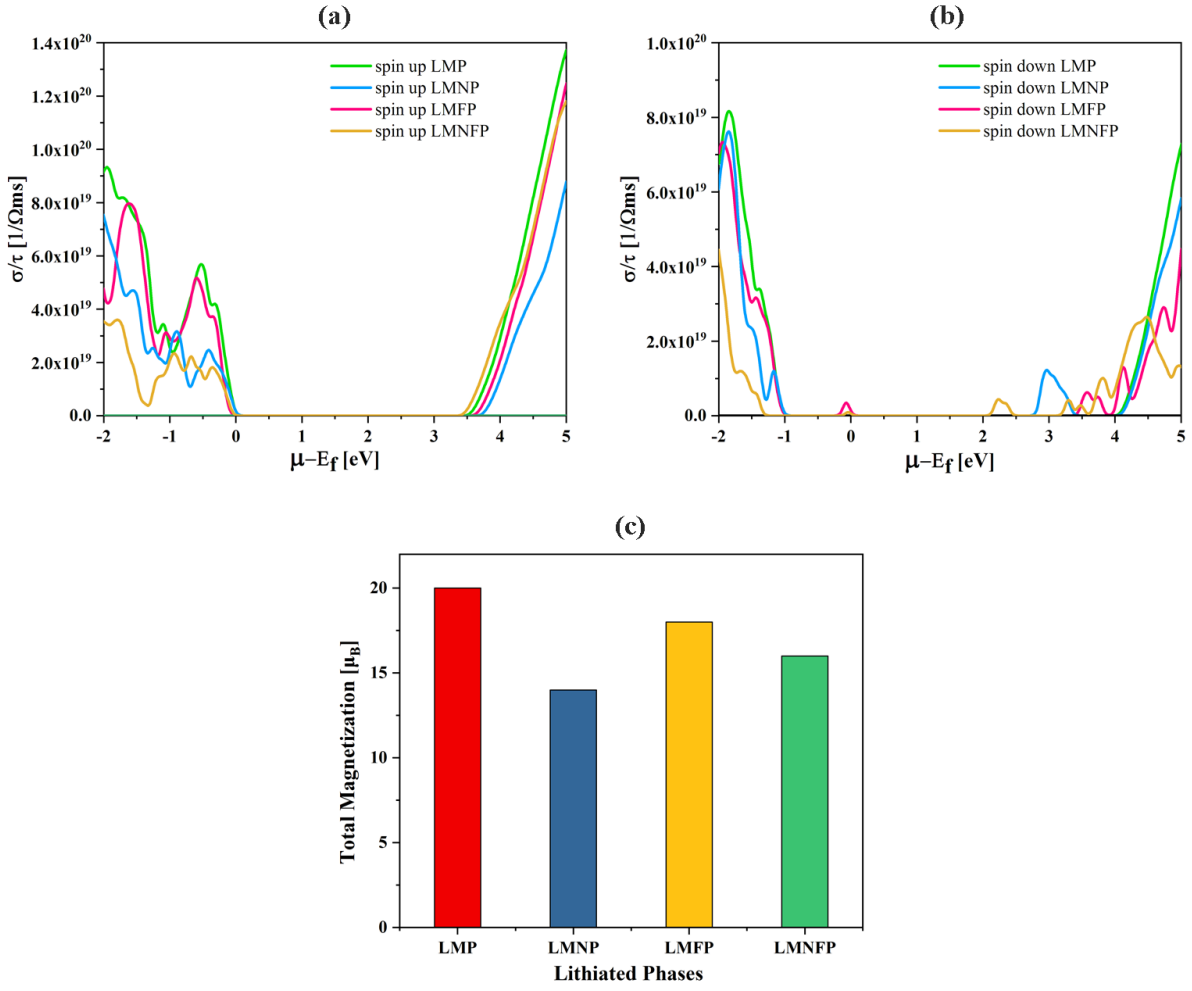

Figure 4.7: Electrical conductivity for both spins (a) up and (b) down and (c) total magnetization of LMNFP, LMNP, LMFP, and LMP.

for $LiMnPO_4$ and $LMn_{0.5}Ni_{0.25}Fe_{0.25}PO_4$ were found to be 170.87 and 169.61 $mAh.g^{-1}$, respectively. The relative change between the two capacities is 0.73% indicating that the

capacity of the pure structure is not strongly changed by Ni–Fe codoping. A similar effect was also noticed for the 50% substitution of Ni/Fe in Mn-sites of the bare structure ($LiMnPO_4$) [23]. The change in the theoretical capacity can be explained by the difference in the molar mass of each compound. Otherwise, the theoretical capacity of LMP is in agreement with the experimental investigation by Guohua et al. who found that the storage capacity of Li-ion reaches 171 mAh.g $^{-1}$ at the first cycling charge with a charge up to 4.8 V [16].

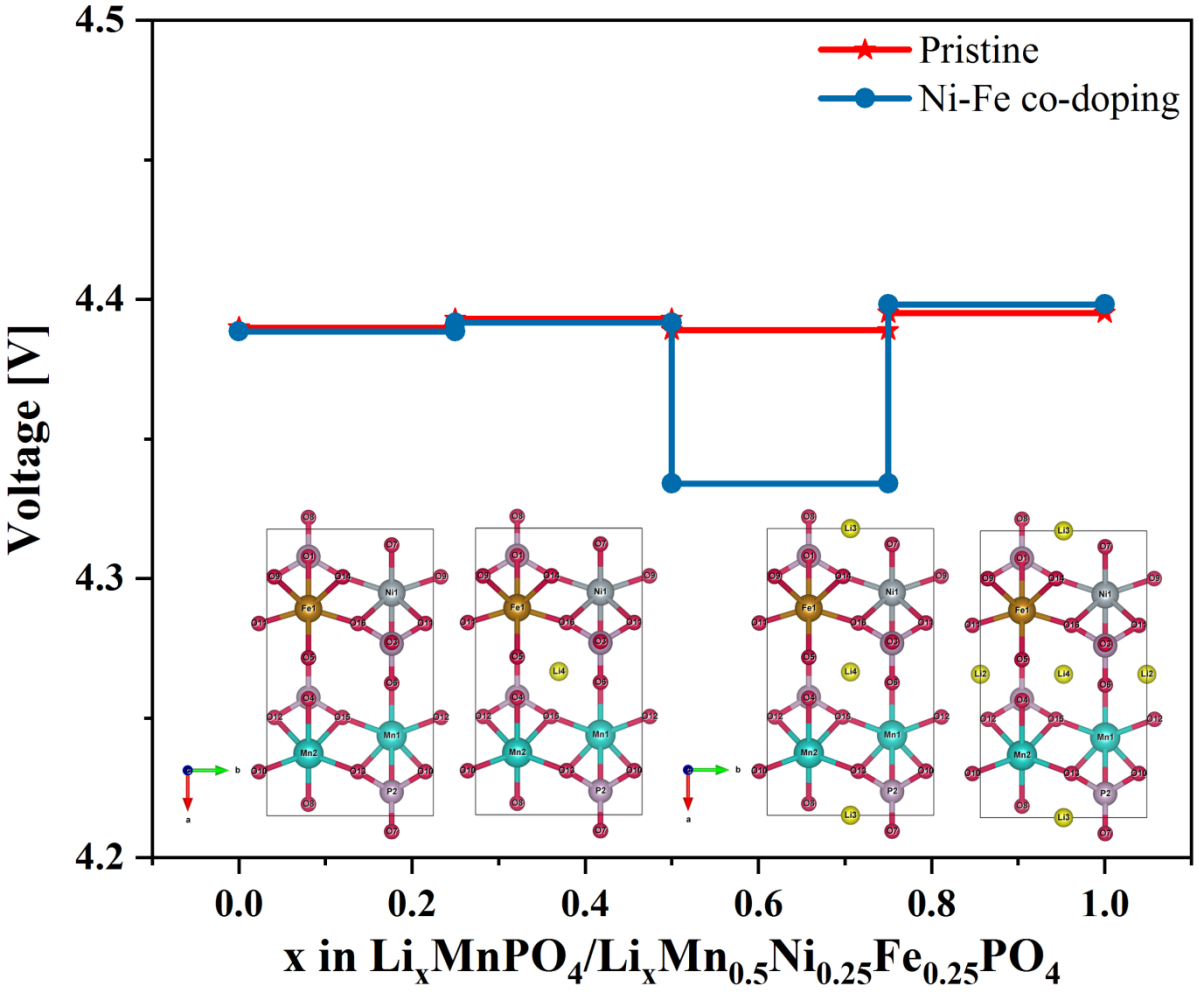

Figure 4.8: Voltage profile of $Li_xMnPO_4/Li_xMn_{0.5}Ni_{0.25}Fe_{0.25}PO_4$ with a representation of the optimised $Li_xMn_{0.5}Ni_{0.25}Fe_{0.25}PO_4$ structures.

Figure 4.7c reveals that the total magnetization of pristine LMP is affected by Ni–Fe codoping, and Ni/Fe single doping [23]. The magnetization of LMP is decreased from 20 to 14, 18 and 16 μ_B for LMNP, LMFP, and LMNFP, respectively. The reduction in the magnetization can be attributed to the small magnetic moment of Ni (1.73 μ_B) and Fe (3.45 μ_B) compared to that of Mn (5 μ_B).

The open-circuit voltage (OCV) was calculated using eq 4.3 for various lithium concentration ranges (x: 0–0.25, 0.25–0.5, 0.5–0.75, and 0.75–1) for Li_xMnPO_4 and $Li_xMnNiFePO_4$. The calculated values for these successive ranges were found to be 4.390/4.389, 4.393/4.392, 4.389/4.334, and 4.395/4.398 V for $Li_xMnNiFePO_4$/ Li_xMnPO_4 as depicted in Figure 4.8. From these values, we can see a fluctuation around the average (AOCV) of LMP (4.39 V) and LMNFP (4.37 V). A slight change in AOCV of LMP was noticed by Ni–Fe co-doping, where the change from 4.39 V (for LMP) to 4.37 V (for LMNFP) indicates the stability of the OCV by Ni-Fe co-doping of LMP and these voltages within the current electrolyte windows. Moreover, the AOCV value of the pristine LMP is in line with experimental and theoretical investigations [62, 166].

4.3.5 Li-Ion Migration

The kinetics of charging/discharging is an important factor for the performance of LIBs. To investigate the effect of Ni–Fe codoping in the kinetic property of LMP, the diffusion of a single Li-ion in MP and MNFP was evaluated using the NEB method with seven interpolating images along the diffusion path. Furthermore, for minimizing the interactions between the periodic images during the diffusion of Li-ions, we chose a 1 × 2 × 2 supercell.

As it is well known, the diffusion of Li in olivine structures is located in the 1D channel along the b-axis [167, 87, 168, 169]. Figure 4.9a,d shows the Li-ion diffusion pathway in MP and MNFP and the corresponding energy profile. The calculated energy barrier of Li-ion diffusion in MP and MNFP are 0.40 and 0.34 eV, respectively (see Table 4.4). The activation energy of Li-ion diffusion in MP is consistent with the previously reported value by Sgroi et al. (0.44 eV) [165]. Comparing the calculated energy barriers of Li-ion between MP and MNFP, it can be deduced that Ni-Fe co-doping reduces the barrier energy, indicating a faster diffusion of Li-ions in the MNFP compared to that in MP and MFP (0.39 eV [23]) structures. Moreover, the barrier energy of Li-ion in MNFP delithiated phase is between the barrier energy of lithiated $LiFePO_4$ (0.48 [10]) and delithiated $FePO_4$ (0.20 eV [170]) phases of the commercial cathode material for lithium ion batteries. This suggests that Ni–Fe codoped LMNFP possesses activation energy comparable to that of the commercial cathode material. In addition, LMNFP has good electronic conductivity than $LiFePO_4$ as mentioned above.

For a better understanding of this improvement in Li intercalation, the diffusion coefficient (D) of Li in MP and MNFP were calculated using eq 4.4 and are listed in Table 4.4. From this table, the calculated ratio $\frac{D2}{D1}$ is found to be 9.5 indicating that the Li-diffusion in MNFP could

be roughly 10 times faster than that in pure MP, indicating that the Ni–Fe codoping is beneficial for enhancing the ionic conductivity of pure MP. In the same context, there are some experimental studies that reported that co-doping could enhance the kinetics properties of Li-ion in pure LMP. For example, Hu et al. found that Fe–Mg codoping could improve the electrochemical kinetics of Li-ions in the pristine structure LMP [151]. The improvement of ionic conductivity of Li-ions by Ni–Fe co-doping is explained by the decrease of Pauli repulsion between Li ions and octahedral MO6, as suggested in the literature [141, 165, 151]. It is also ascribed to charge transfer from lithium to oxygen atoms because the diffusion of Li is through a 1D channel along the b-axis, which is surrounded by the octahedral oxygen. Therefore, upon Ni–Fe codoping, these oxygen atoms become less negative compared to the pristine MP (see Table 4.3). This charge depletion weakens the bond between the closed oxygen anions (O^{2-}) and the diffused Li^{+}, leading to easier Li migration in MNFP compared to pristine MP. On the other hand, this improvement in the kinetic property of MP by Ni–Fe co-doping is attributed also to the slight difference in the average binding energy of Li between pristine LMP and Ni–Fe co-doping LMNFP. For example, using eq 4.2, the calculated average binding energy of lithium in pure LMP and LMNFP was found to be 4.39 and 4.37 eV, respectively, indicating that the energy needed to insert Li into the host structure LMNFP is slightly lower than that of pristine MP. Therefore, the diffusion of Li-ion in LMNFP is easier to some extent than the diffusion of Li in pristine LMP.

Table 4.4: Hopping Lengths, Activation Barriers Energie, and Diffusion Coefficient for Li Diffusion Along the b-axis in MP and MNFP.

Compounds	Hopping lengths l [Å]	activation barrier $\mathbf{E_{act}}$ [eV]	Diffusion Coefficient D [cm^2/s]
Li –ion in MP	**3.49**	**0.40**	**2.109×10^{-10}**
Li–ion in MNFP	**3.35**	**0.34**	**2.008×10^{-9}**

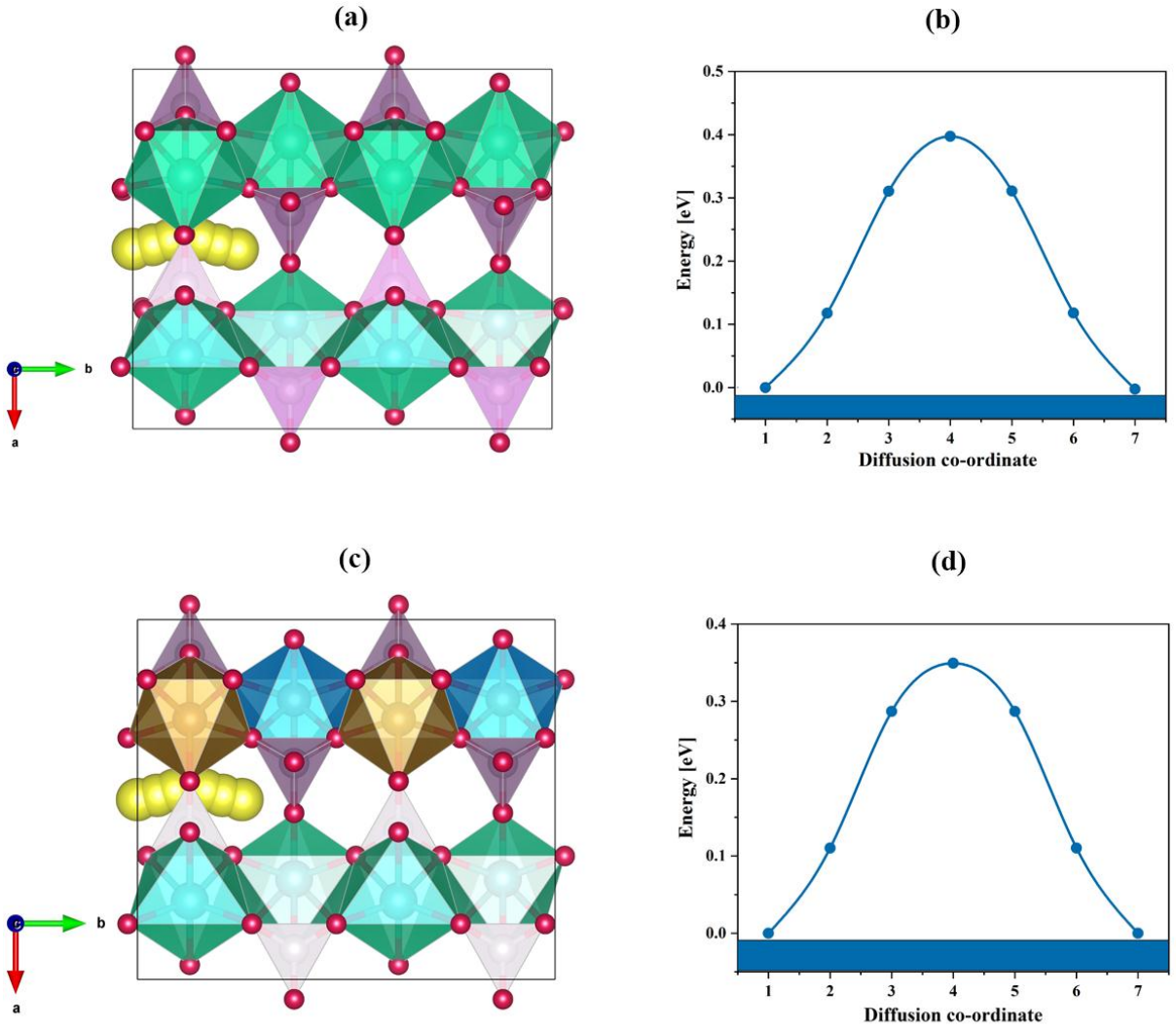

Figure 4.9: Migration paths of lithium ions in (a) MP and (c) MNFP. The energy profiles of lithium-ion diffusion in (b) MP and (d) MNFP.

4.4 Chapter Summary

DFT calculations were performed to investigate the effect of Ni–Fe codoping (i.e. $LiMn_{0.5}Ni_{0.25}Fe_{0.25}PO_4$) on the structural, electronic, magnetic, electrochemical potential and kinetic properties of Li-ions in pristine LMP, as well as on the thermodynamic stability, theoretical capacity, charge transfer, average M–O bond lengths, and electrical conductivity. We also examined the thermodynamic stability and charge transfer of Ni/Fe single doping in lithiated/delithiated ($LiMnPO_4/MnPO_4$) pristine phases, that is, LMNP/MNP ($LiMn_{0.5}Ni_{0.5}PO_4/Mn_{0.5}Ni_{0.5}PO_4$), and LMFP/MFP ($LMn_{0.5}Fe_{0.5}PO_4/Mn_{0.5}Fe_{0.5}PO_4$). The key results are summarized below.

1. The calculations indicated that all compounds are thermodynamically stable. In addition, a small change in unit cell volume between lithiated and delithiated phases for all structures was observed, indicating good reversibility during Li insertion/extraction.
2. Electronic property analysis revealed that Ni–Fe co-doping reduces the bandgap of LMP from 3.62 to 1.55 eV, implying that Ni–Fe co-doping can improve the electronic conductivity of LMP.
3. The theoretical capacity and intercalation voltage of Li-ions in pristine LMP are slightly affected by Ni–Fe co-doping.
4. The migration barrier energy of Li-ion in MNFP (0.34 eV) is lower than that in MP (0.40 eV), implying that Ni–Fe codoping is beneficial for improving the ionic conductivity of Li-ion pristine MP.

In general, the results presented here suggest that LMNFP could be a promising cathode material for high-performance lithium-ion batteries. Simultaneously, this study is crucial for better understanding the effect of Ni–Fe codoping on the performance of LMP as a cathode material for LIB batteries.

Chapter 5

Strain effects on the electrochemical performance of $LiMnPO_4$

5.1 Background

Recently, phosphor-olivine family $LiMPO_4$ (M=Fe, Mn, Ni, and Co) have attracted significant attention as cathode materials for LIBs due to their advantages such as high thermal stability, good rate performance, high capacity, and environmental compatibility [171]. Within this family, lithium manganese phosphate ($LiMnPO_4$ (LMP)) has attracted much attention as a suitable alternative to the toxic layered cathode material due to its series of advantages such as high intercalation potential of 4.1 V versus Li/Li^+ (compatible with the current liquid electrolytes), the low cost [61], high energy density (higher than that of $LiFePO_4$), environmental friendliness, good stability, and excellent theoretical capacity. However, LMP possesses low electronic and ionic conductivities, which reduces its performance as a cathode material for LIBs [172]. Hence, enormous efforts have been made to improve the intercalation properties of LMP by different strategies such as carbon coating [173], reducing the particle size [58, 174], and cation doping [172]. Nevertheless, the rate performance of LMP cathode materials still requires significant improvement to meet the rigorous requirements of high-energy devices [175].

In this context, it is worth noting that the rate performance of intercalation compounds is related to the ionic and electronic conductivities which are, in turn, dependent on structural and defect properties [176]. Lattice strain has attracted significant attention as an efficient strategy to improve the functional properties of different materials such as ionic conductivity, superconductivity, and ferroelectrics [177-182]. In particular, previous experimental studies have highlighted the positive effect of the lattice strain on the electrochemical performance of olivine cathode materials. For example, Shahid et al. reported an enhancement in the electronic conductivity of $LiFePO_4$ which is ascribed to the lattice strain associated with the reduction of particle size [183]. Furthermore, the produced mechanical strain at the interface of substrate/LiFePO4 thin film shows a positive effect on structural modification, film textural, and electrochemical stability upon cycling [38].

In parallel to experimental studies, theoretical investigations suggest that the electrochemical performances of olivine cathode materials can be improved by lattice strain. Using atomistic simulation methods, Tealdi et al. examined the effect of lattice strain on the ionic conductivity of olivine-type $LiFePO_4$ and $NaFePO_4$ [176] and demonstrated that the lattice strain can improve the ionic conductivity in cathode materials, thereby improving their charge/discharge rate performance at room temperature. They also showed that the tensile strain applied in the *ac* plane perpendicularly to the principal diffusion direction [010] can enhance the ionic transport compared to the *ab* and *bc* planes. Lee et al. reported that the biaxial strain ameliorates ionic and electronic conductivities by 15 and 50 times $LiFePO_4$ [184], respectively, at room temperature. It is worth emphasizing that the effects of mechanical strain on battery cathode materials have not been extensively investigated.

To the best of our knowledge, the effect of lattice strain on the pristine LMP has not been investigated previously in the literature so far. In addition, there are limited fundamental studies on the effect of the anti-site defects on the ionic conductivity of LMP as cathode material. Therefore, the current study seeks to provide insights into the effect of biaxial strain on the thermal and dynamic stability, structural, electronic, kinetic, and defect properties, as well as on the intercalation voltage. In addition, the effect of intrinsic defects on Li-ion migration in strained and unstrained LMP was discussed.

5.2 Computational details

All calculations were performed within the framework of DFT using the projector augmented wave method as implemented in Quantum Espresso (QE) code [108, 104]. The revised Perdew–Burke–Ernzerhof for solid-state systems (PBEsol) with the generalized gradient approximation was used to describe the exchange-correlation interactions [155]. In order to treat the strong correlation of d-orbitals in Mn transition metal, we used the Hubbard correction (U) of 4.5 eV [106, 127]. A plane wave basis set with an *88* Ry (1197.30 eV) cutoff was selected. The Brillouin zone was sampled with 4 × 5 × 6 and 12 × 15 × 18 Monkhorst–Pack k-point meshes [129] for structural optimization and electronic structure computations, respectively. The lattice parameters and atomic positions were relaxed using the Broyden–Fletcher–Goldfarb–Shanno algorithm [129] with energy, force, and stress convergence of 10^{-4} Ry/Bohr, 1×10^{-6} Ry and *0.01* kbar, respectively. Furthermore, the density of states (DOS) was calculated using the Marzari–Vanderbilt–smearing method with a degauss of 0.01 Ry. The visualization of crystal structures was drawn using VESTA software

[109]. The electrical conductivity was examined by the BoltzTrap code which is based on the resolution of the Boltzmann transport equation with constant scattering time approximation [145].

Olivine-type LMP unit cell was allowed to relax at zero pressure and zero applied strain. Subsequently, the biaxial compressive and tensile strains were applied in the *ac* plane, the equivalent ε_{xx} and ε_{zz} strain are applied along the directions [100] and [001] of x- and z-axes respectively, where the lattice parameters *a* and *c* of LMP are constrained to various values different from their equilibrium lattice parameters, a_0 and c_0, by fractions starting from -2.5% to +2.5% using a step size of 0.5 %, negative/positive values represent compressive/tensile strain. Furthermore, under each strain, the perpendicular lattice parameter *b* is obtained by relaxing all atomic positions to the lowest energy state. The biaxial strain ε is expressed by the following equation

$$\varepsilon_{XX}(\%) = \varepsilon_{ZZ}(\%) = \frac{a(c) - a_0(c_0)}{a_0(c_0)} \times 100 \tag{5.1}$$

where a/a_0 and c/c_0 denote the strained/unstrained lattice parameters.

In order to seek the influence of biaxial strain on the stability of the LMP compound, we conducted ab-initio molecular dynamics (AIMD) simulations within the framework of the canonical ensemble (NVT) at a standard temperature using a simulation time of 3 *ps* with a time step of 0.5 *fs*. Furthermore, we assessed the dynamic stability within the phonon-dispersion curve of the unstrained and strained LMP through the finite displacement method implemented in the PHONOPY program package [185].

Li-intercalation voltage of unstrained/strained LMP was evaluated by the following equation

$$V = -\frac{E(Li_{x2}MnPO_4) - E(Li_{x1}MnPO_4) - (x_2 - x_1)E(Li)}{(x_2 - x_1)e} \tag{5.2}$$

wherein, $E(Li_{x2}MnPO_4)$ and $E(Li_{x1}MnPO_4)$ refer to the total energy of the unstrained/strained LMP system with x_2 and x_1 Li-concentration, respectively, while E(Li) and *e* represent the energy of one Li-atom in the bcc structure and absolute electron charge, respectively. In addition to Li intercalation voltage, the kinetic properties of unstrained and strained LMP olivine were investigated using the nudged elastic band (NEB) method. Then,

we go a step further to evaluate lithium kinetics in these unstrained/strained structures with the presence of anti-site defects. For this purpose, 1 × 2 × 2 supercells were used to calculate Li activation energy and compute the diffusion coefficient (D) [157]through the transition state theory

$$D = a^2 \vartheta_0 exp\left(\frac{-E_{act}}{k_B T}\right) \tag{5.3}$$

where a, ϑ_0, E_{act}, k_B, and T are the hopping distance that is ~3 Å for all compounds, attempt frequency, activation energy, Boltzmann constant, and absolute temperature, respectively. In this regard, it is worth noting that ϑ_0 is an effective frequency associated with the vibration of the Li-ion in the direction of the saddle point. In this work, we have used $\vartheta_0 \sim 10^{12}$ Hz, which is the common value reported by several studies [186, 187].

5.3 Results and Discussions

5.3.1 Crystal Structure

Before starting our in-depth study, we first optimized the structural geometry of pristine LMP olivine material. Figure 5.1 shows the relaxed structure of LMP which has an orthorhombic unit cell with Pnma group (number 62) [171]. The cell is constructed from PO_4 tetrahedral and MnO_6 octahedral, this construction creates channels along the b-axis which enables the migration and storage of Li-ions. The lattice parameters *a*, *b*, and *c* were found to be 10.54, 6.14, and 4.74 Å, respectively. These lattice parameters are in excellent agreement with experimental measurements; 10.45, 6.11, and 4.75 Å [10], demonstrating the reliability of our calculations with the DFT+U approach.

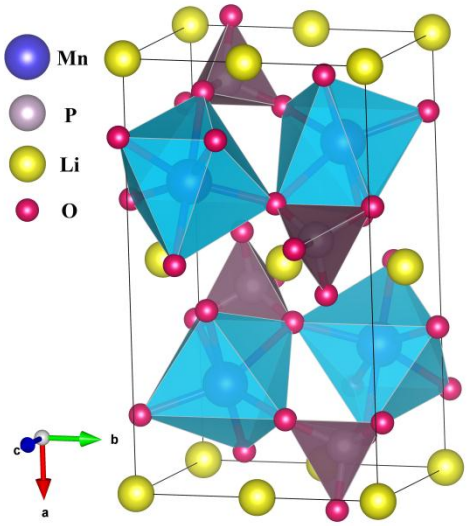

Figure 5.1: Crystallographic structure of LMP. Blue and purple colors represent octahedral MnO_6 and tetrahedral PO_4 units, respectively.

Once the LMP unit cell was optimized, the biaxial compressive and tensile strain were applied in the ac plane by constraining equivalently the lattice parameters *a* and *c*. Under each applied strain, the lattice parameter *b* is obtained by relaxing all atomic positions to the lowest energy state. Therefore, the lattice parameter *b* becomes the sole lattice parameter of the crystal structure for scaling behavior. Figure 5.2 shows the influence of biaxial strain on the evolution of the lattice parameter *b* and unit cell volume of olivine system LMP. From this Figure, it can be seen that the lattice parameter *b* ranges from 6.28 to 6.06 Å when the plane strain is applied from -2.5 % compressive to +2.5% tensile strain. The unit cell volume of LMP decreases and increases linearly with compressive and tensile strain, respectively. Similar behavior has been reported in previous studies such as Li_2MnSiO_4 compound [188], $LiFePO_4$, $NaFePO_4$ [176], lithium borohydride $LiBH_4$ [189], and $ZrNiH_3$ [190].

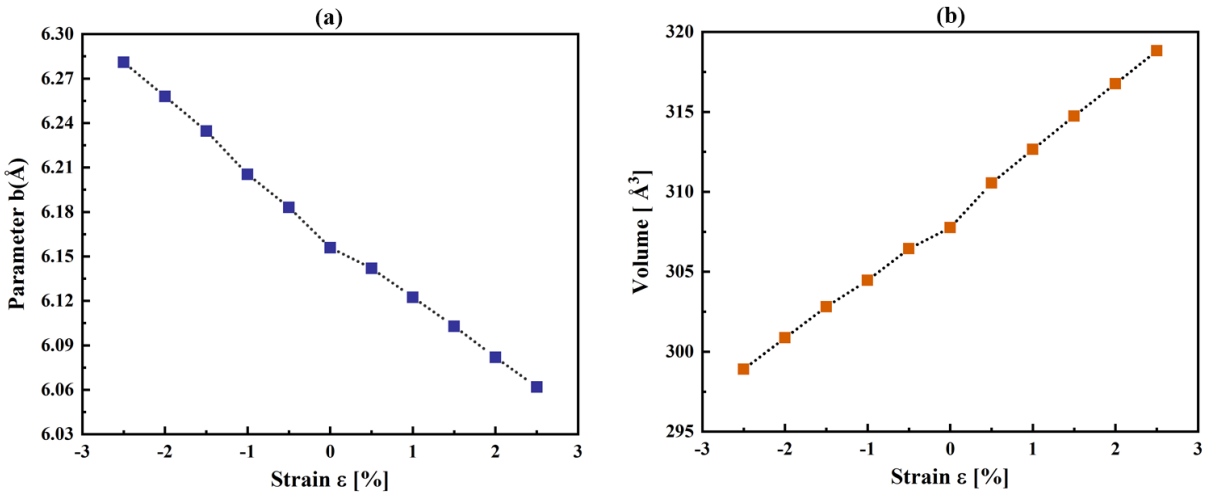

Figure 5.2: Optimized (a) lattice parameter b and (b) unite cell volume V after a biaxial strain in the ac plane.

To better understand the effect of the applied biaxial strain on the geometric structure of LMP, the average bond lengths of Li–O, Mn–O, and P–O were calculated and listed in Table 1. It is clearly shown that the Mn–O and Li–O bond lengths are slightly affected by the compressive/tensile strain, while the P–O bond length remains constant under strain at the value of 1.55 Å. For example, under biaxial tensile strain, the bond lengths of Li–O/Mn–O increase slightly from 2.15/2.22 to 2.19 Å/2.25 Å with increasing the tensile strain. On the other hand, the bond lengths of Li–O/Mn–O decrease from 2.15/2.22 to 2.12 Å/2.21 Å with increasing compressive strain. The calculated average bond lengths Li–O, Mn–O, and P–O of

the unstrained systems are excellent with experimental results [149, 191, 192].

From these results, it can be concluded that the slight change in unit cell volume under strain can be explained by the slight change in volumes of the LiO6 and MnO6 octahedral units. Furthermore, the unaffected P–O bond lengths indicate that PO_4 really plays a main role in the structural stability of the olivine system, thereby it helps to maintain the structure intact during the cycling process. This conclusion is in line with several experimental and theoretical studies, which reported that PO4 is the main responsible for the stability of the olivine structure [193, 194]. Moreover, to gain more insight into the effect of biaxial strain on the geometrical structure, we performed charge density analysis using Bader charge analysis [111]. Table B.1 shows the atomic charges of all atoms in both lithiated and delithiated phases of unstrained and strained compounds. It can be observed that the charge transfer is not affected by biaxial strain which ranges from -2.5 to +2% to some extent, indicating the structural stability of strained compounds.

Table 5.1: Average Bond Lengths (Li−O, Mn−O, and P−O) for Unstrained and Strained Systems.

Strain (%)	Li–O (Å)	Mn–O (Å)	P–O (Å)
-2.5%	2.122	2.217	1.548
-2%	2.129	2.220	1.549
-1.5%	2.135	2.222	1.550
-1%	2.141	2.224	1.550
-0.5%	2.148	2.227	1.551
0%	2.154	2.227	1.553
+0.5%	2.163	2.234	1.553
+1%	2.171	2.239	1.554
+1.5%	2.179	2.243	1.554
+2%	2.186	2.247	1.555
+2.5	2.194	2.252	1.556

5.3.2 Dynamic and thermal stabilities

In order to assess the dynamic stability of strained LMP, the phonon dispersion curve was plotted along the high symmetry directions in the first Brillouin zone as presented in Figures 3 and 4. It is obvious that there are no soft modes (negative frequencies) for strained

compounds starting from -2.5% to +2%, which suggest the dynamic stability of the structure in this strain range. While, for the tensile strain of +2.5%, the phonon dispersions curve exhibits imaginary frequencies along the high symmetry directions Γ–Z–U indicating the dynamical instability of LMP at this applied strain. Therefore, the +2.5% tensile strain won't be discussed any further.

To assess the thermal stability of the electrode materials during the charge/discharge process, we performed AIMD simulations within the NVT ensemble at room temperature during 3 *ps* for unstrained and strained LMP. Figure 5.5 and Figure S1 (Supporting Information) depicted the total energy as a function of simulation time. From snapshots of the resulting unstrained and strained compounds, it can be noticed that all systems preserve a similar geometrical arrangement without any structural distortion. Furthermore, the corresponding total energy fluctuates by 1.1 eV for the range -2.5 to 2% of applied strain which indicates that there is only a small variation in total energy as a function of simulation time suggesting excellent thermal stability of unstrained and strained systems at room temperature. From the stability results, it can be inferred that the unstrained and strained compounds are dynamically and thermally stable. These results are consistent with experimental studies that have already shown the thermal stability of LMP compounds. For instance, Martha et al. reported the excellent thermal stability of the LMP compound during aging at a high temperature of 60 °C and reaction with electrolyte solutions at temperatures above 150 °C [87]. In addition, Ying et al. revealed that both LMP and the common commercial $LiFePO_4$ have comparable thermal stability in their pristine and fully delithiated states, which are stable up to 400 °C [163]. Similarly, Kim et al. demonstrated that the LMP phase is highly stable at elevated temperatures up to 410 °C [164].

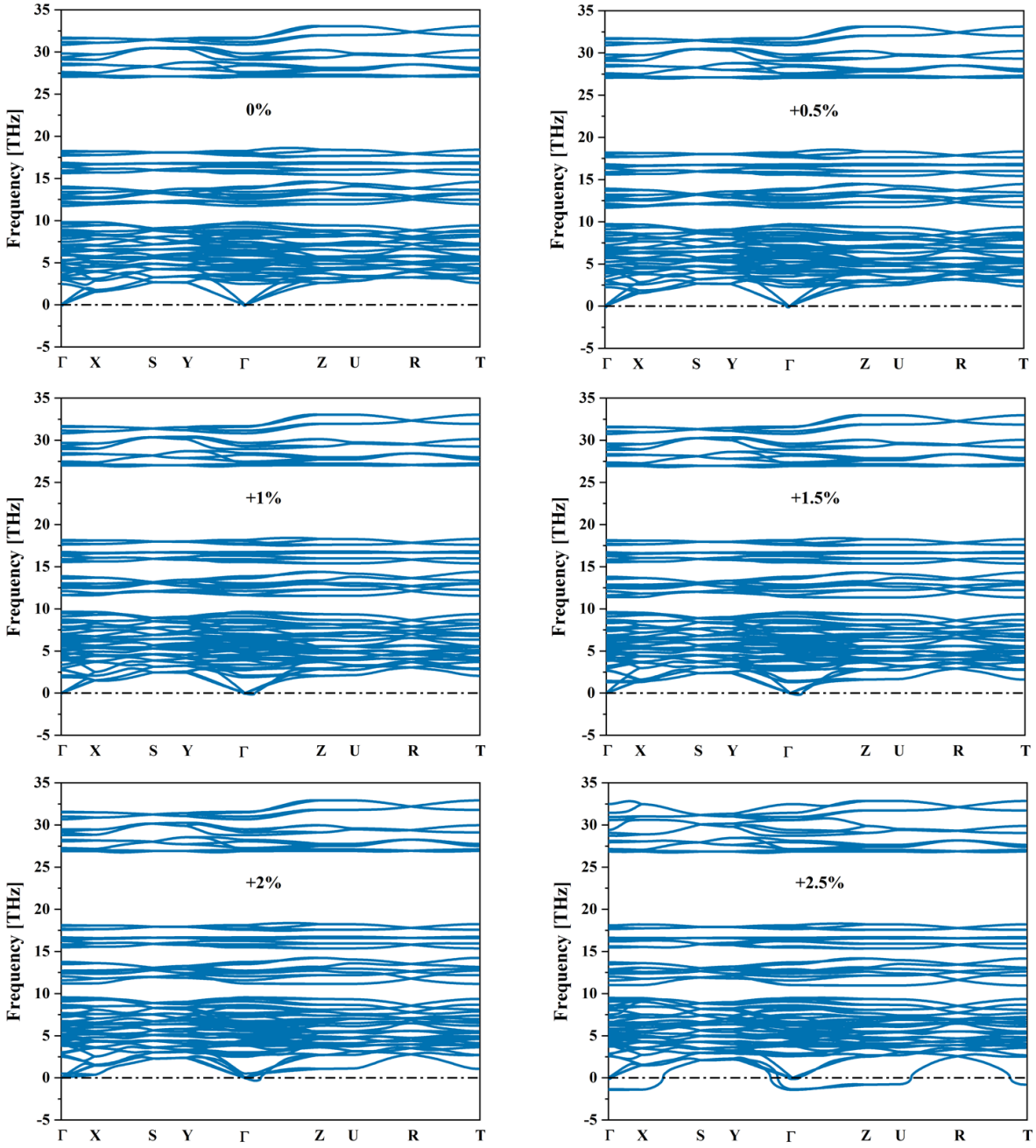

Figure 5.3: Phonon dispersion curves of LMP under biaxial tensile strain. Strain values are shown inside the plots.

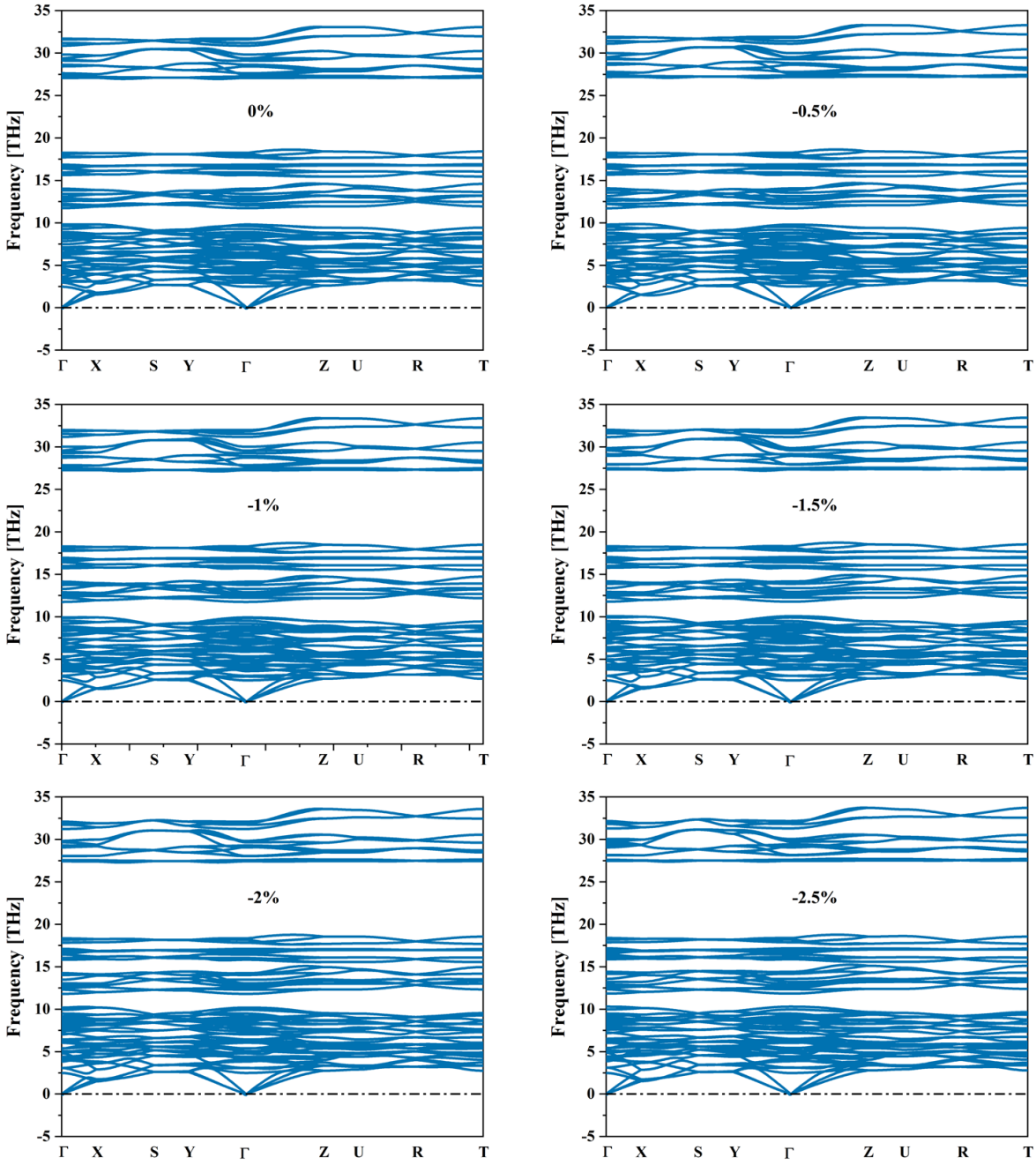

Figure 5.4: Phonon dispersion curves of LMP under biaxial compressive strain. Strain values are shown inside the plots.

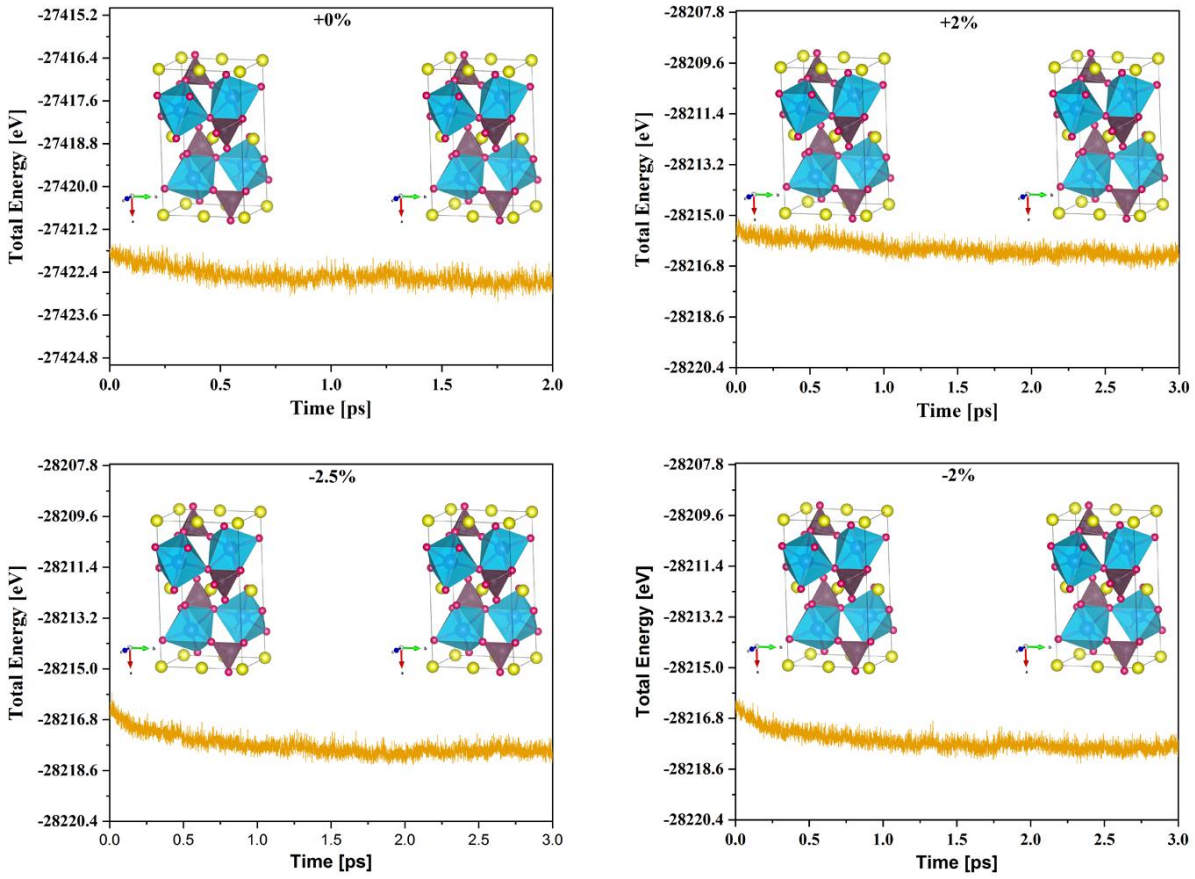

Figure 5.5: Total energy evolution during a simulation of 3 ps at room temperature of unstrained and strained LMP. Snapshots of unstrained and strained structures at the end of the MD simulation are inserted in the plots.

5.3.3 Electronic properties

The excellent electronic conductivity of cathode materials is a crucial benchmark that significantly governs the efficiency of Li-ion batteries. In this context, the electronic properties of unstrained and strained LMP compounds were examined through the DOS calculations. The total (TDOS) and partial DOS (PDOS) for unstrained and strained LMP have been plotted in Figures 5.6, 5.7, B.2, and B.3. We see from the results that the unstrained LMP exhibits a semiconducting behavior with a band gap (E_g) of 3.51 eV. This value is consistent with that previously reported by Lethole et al [62].

When we applied the strain, the band gap value was found to be 3.84, 3.74, 3.68, 3.61, 3.57, 3.51, 3.48, 3.48, 3.44, 3.41 eV for ε= -2.5%, ε= -2%, ε= -1.5%, ε= -1%, ε= -0.5%, ε= 0%, ε= +0.5%, ε= +1%, ε= +1.5%, ε= +2%, respectively. This shows that the strained LMP compounds preserve the same electronic behavior (semiconductor state) of unstrained LMP

with different band gap values. From the calculated band gap values, it can be observed that the band gap of strained LMP increases with increasing the compressive strain up to 3.84 eV at -2.5%, while it reduces with increasing the tensile strain to reach a minimum value of 3.41 eV at +2%, indicating that the electronic conductivity of LMP compound is significantly related to the type and severity of strain applied (compressive or tensile strain). Therefore, the tensile strain can be a good strategy for improving the electronic conductivity of LMP.

Based on these results, in addition to the Hubbard parameter values or the used functional [27], the slight difference in the band gap values reported in the previous studies can be attributed to the strain used in each work. This means that a slight difference in the lattice parameters between the different studies may result in both biaxial or uniaxial strain and thus a slight difference in the band gap values.

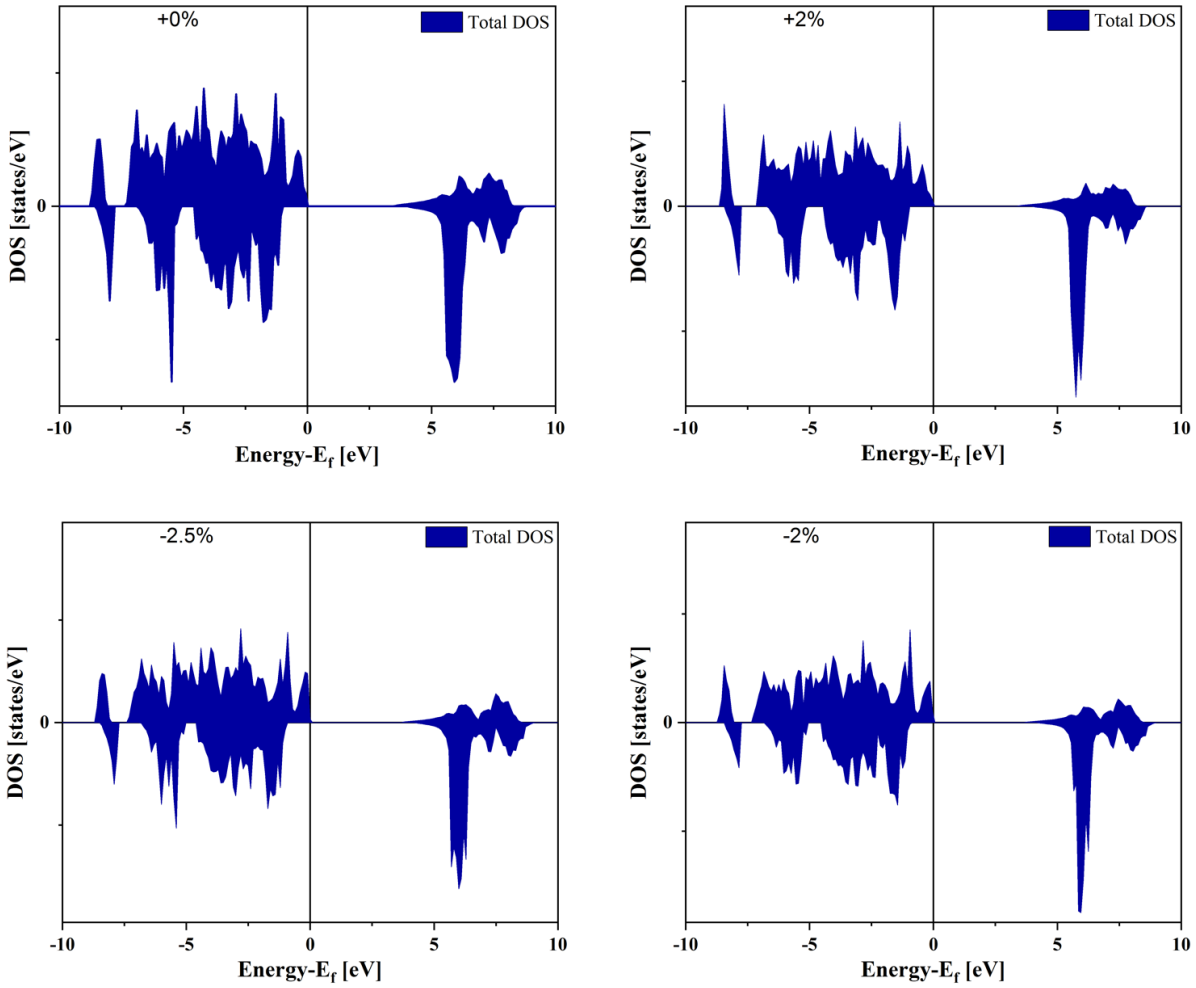

Figure 5.6: Total DOS of unstrained and strained LMP compounds for the different considered strain values as shown inside the plots.

The PDOS analysis disclosed that the valence band maximum (VBM) of unstrained and

strained LMP is mainly formed by the hybridization of Mn-3d (spin-up) and O-2p (spins up and down) orbitals. Meanwhile, the conduction band minimum (CBM) is mainly composed of unoccupied Mn-3d (spin-down) states and a small contribution of Li-2s states. These features are in good agreement with previous studies [27, 74, 165]. It can also be observed that the main responsible for the increases and decreases in the band gap value is the Li-2p spin-up states in CBM, where compressive and tensile strain make Li orbitals move to higher and lower energy, respectively. Moreover, the Mn ions in LMP are in a +2 oxidation state with a high spin configuration, in which spin-up states of Mn are fully filled, generating a magnetic moment of around 4.28 μB for all applied strains. The obtained magnetic moment value of unstrained LMP is in good agreement with previous studies [125, 126].

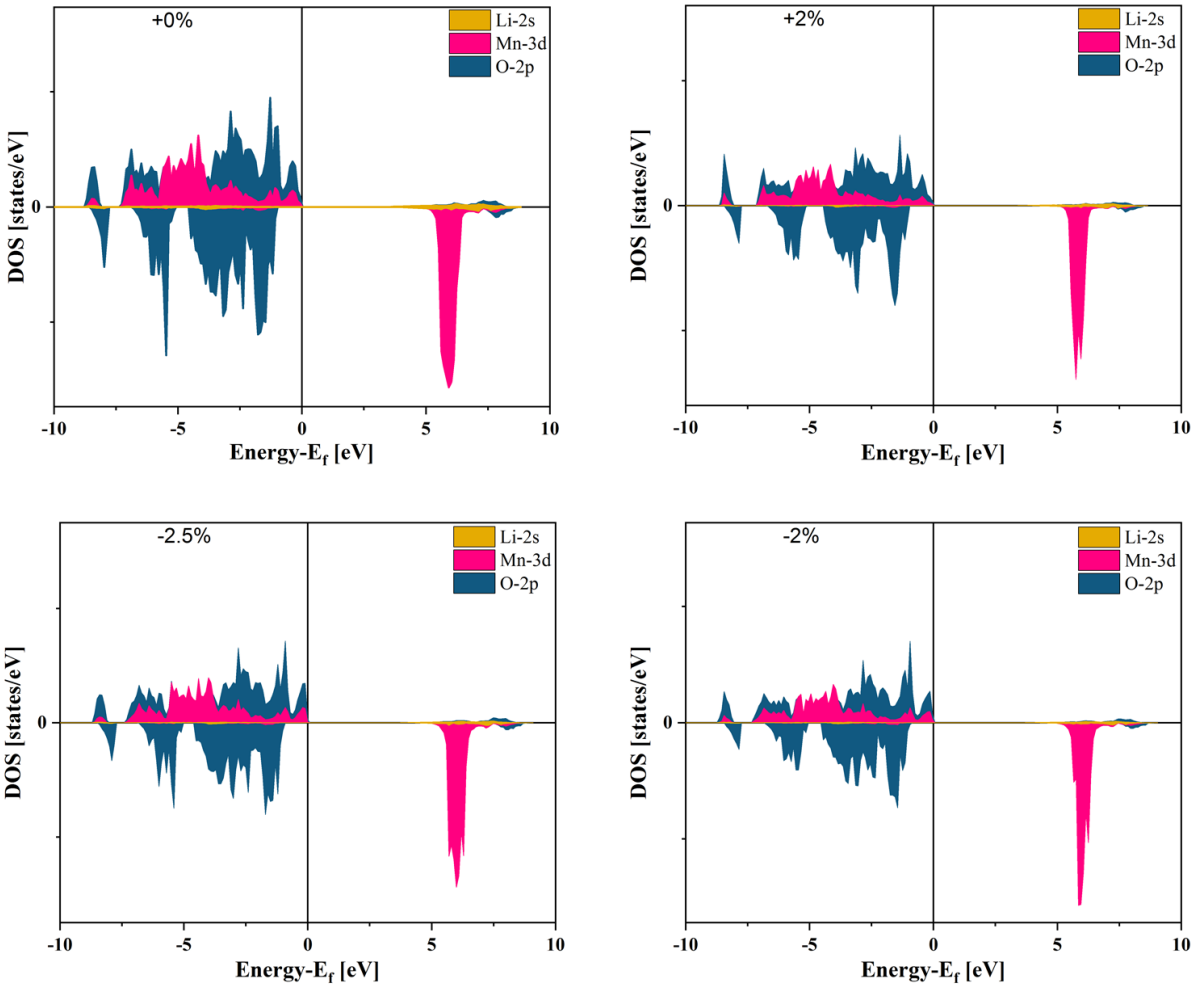

.

Figure 5.7: Projected DOS of unstrained and strained LMP compounds for the different considered strain values as shown inside the plots.

For a better understanding of the effect of biaxial strain on the electronic mobility of LMP cathode material, the electrical conductivity of unstrained and strained compounds as a

function of chemical potential was examined using the BoltzTrap code, as plotted in Figure 5.8. It is evident that spin-up states are the main contributors to the electrical conductivity in both unstrained and strained LMP. These observations are in accordance with PDOS curves (see Figure 5.7), where the spin-up states (Mn-3d and Li-2p) are the contributor to the VBM and the CBM. Furthermore, spin-up orbitals possess a higher electrical conductivity than the spin-down orbitals in both the p-region (negative chemical potential) and the n-region (positive chemical potential). Moreover, it can be observed that there is also a slight shifting of the conductivity region to the lower/higher chemical potential value compared to unstrained LMP with tensile/compressive strain. This shifting can be ascribed to the decrease/increase of the LMP band gap value upon applying the tensile/compressive strain.

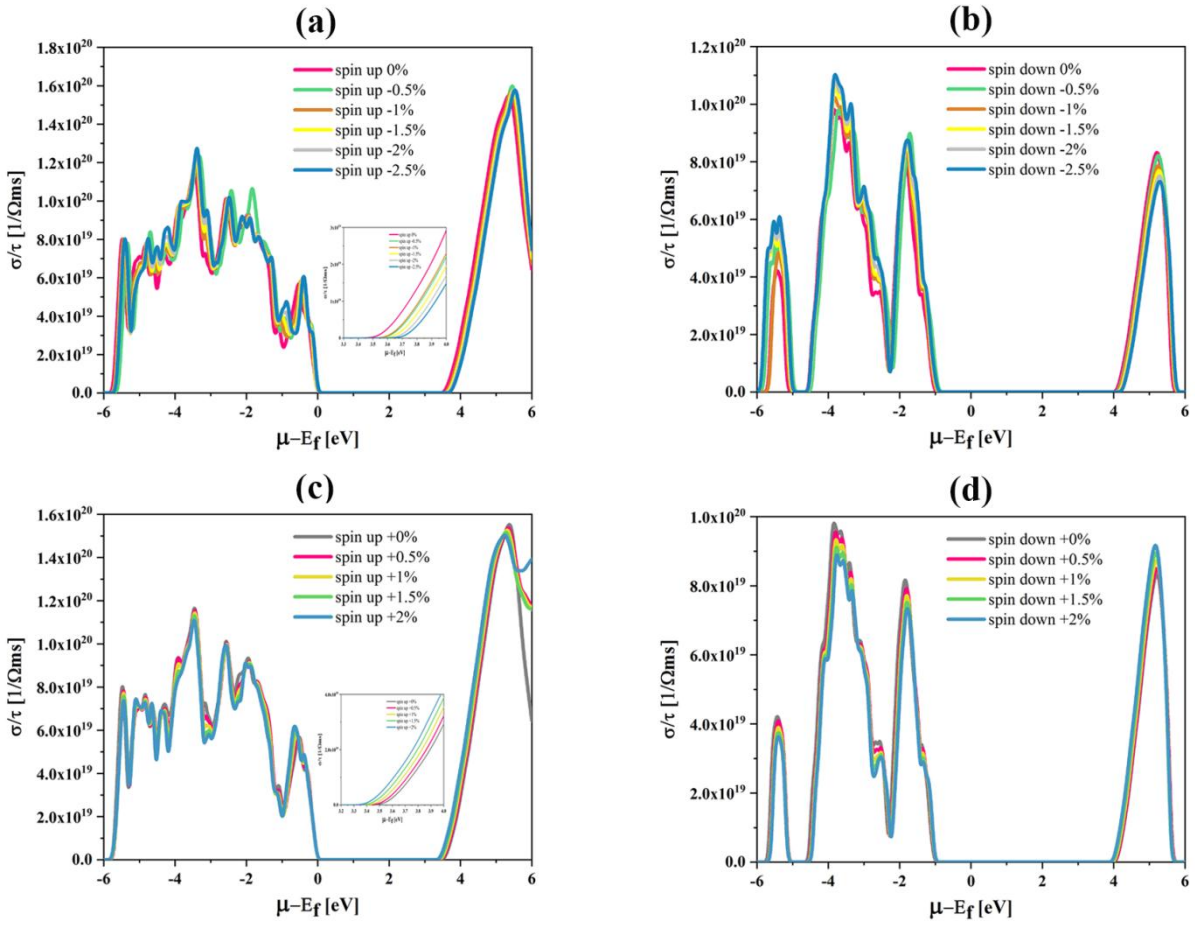

Figure 5.8: Electrical conductivity of spins (a) up and (b) down during tensile strain, and corresponding curves of spin (c) up and (d) down during compressive strain, for both unstrained and strained LMP.

5.3.4 Li intercalation voltage

Li intercalation voltage is a crucial parameter for evaluating cathode materials in LIBs. In this regard, the open circuit voltage of unstrained and strained L_xMP (x=0.25, 0.5, 0.75, and 1) was investigated using eq 2 and illustrated in Figure 5.9. The open circuit voltage for unstrained LMP fluctuates around an average OCV (AOCV) of 4.39V. Comparing the AOCV of LMP (4.39 V) and $LiFePO_4$ (3.57 V) reported in [23], it can be deduced that LMP gain of 0.8 V over $LiFePO_4$ suggests that LMP is an efficient cathode material with high voltage compared to $LiFePO_4$. Our findings are in agreement with experimental and theoretical investigations [15, 168, 195, 196]. For example, Martha et al. found that the voltage profiles of C-$LiMnPO_4$, at C/20 charge-discharge rate at 30 °C, clearly indicate a redox potential around 4.1 V [195], and they reported also that the open circuit voltage of $LiMnPO_4$ is higher than that of commercial $LiFePO_4$ cathode materials by 0.6–0.7 V.

The AOCV of L_xMP under strain is found to be 4.39 and 4.38 V for tensile and compressive strains, respectively. Comparing these values with those of the unstrained LMP, it can be seen that the compressive and tensile strain preserves the open circuit voltage of unstrained LMP to some extent. The OCV values fluctuate around 4.39 V and reach a maximum/ minimum value of 4.40/4.38 V for the applied strain with increasing the Li concentration. This slight increase and decrease of open circuit voltage with a concentration of Li may be explained by the repulsive interaction between Li ions into LMP compounds during Li insertion.

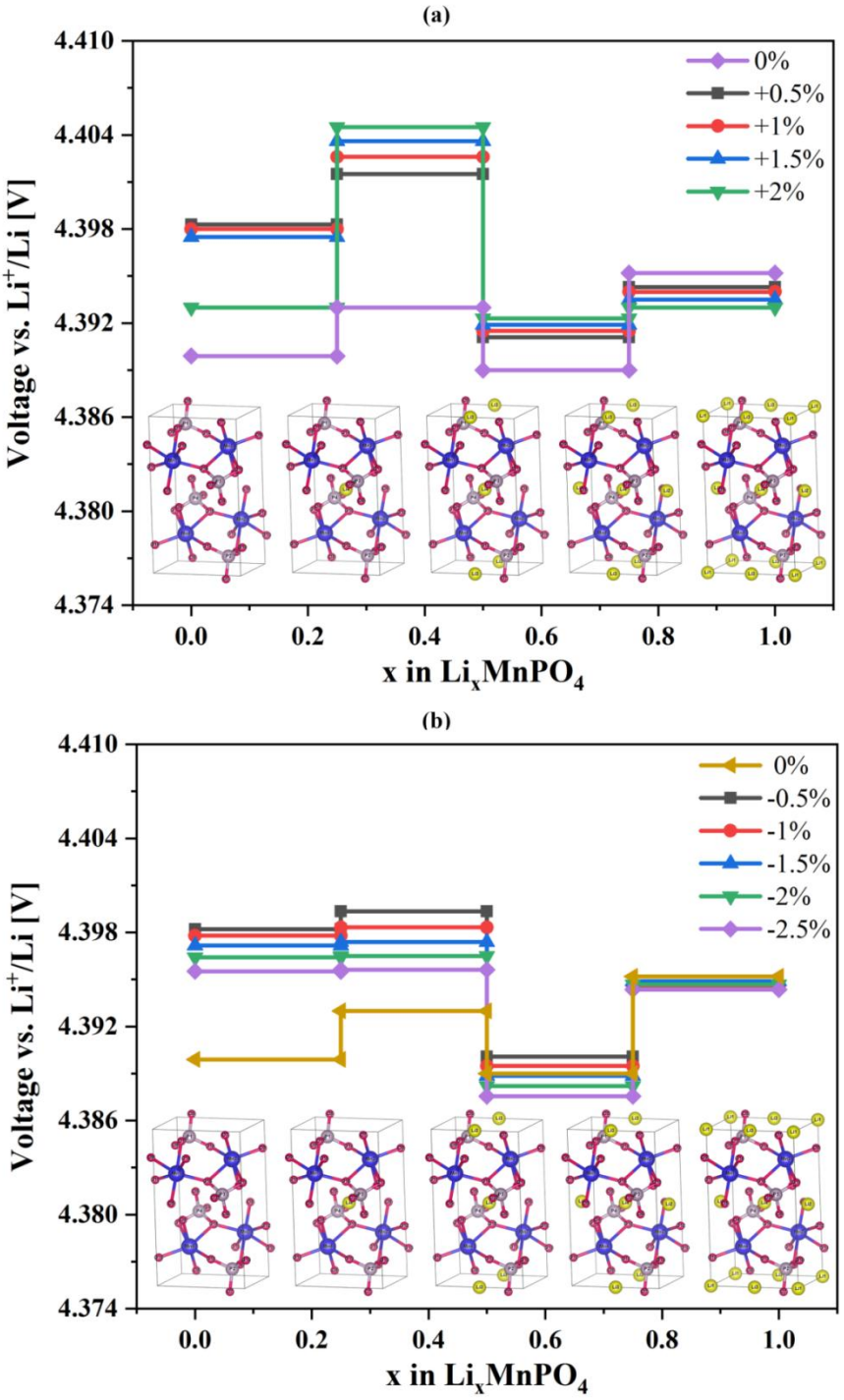

Figure 5.9: Voltage profile of unstrained and strained Li_xMnPO_4 with a representation of their optimized structures, for (a) compressive and (b) tensile strains.

5.3.5 Li-Ion Migration

Besides electronic conductivity and Li intercalation voltage, the ionic conductivity of cathode material plays a central role in the battery performances due to its relation to electrochemical properties such as cycling performance, rate capability, and structural stability. To investigate

the influence of biaxial strain on the kinetic properties of LMP compound, the Li-migration in strained MP was evaluated using the NEB method, in which seven interpolated images were constructed for evaluating Li diffusion paths. A 1 × 2 × 2 supercell was used to prevent the interaction between periodic images. For olivine structure, experimental and theoretical investigations reported that the most probable Li-ions diffusion pathway is located along the 1D channel in [010] direction [64, 1221, 170, 197]. Hence, in this work, Li-ion diffusion in the [010] direction was considered for all calculations.

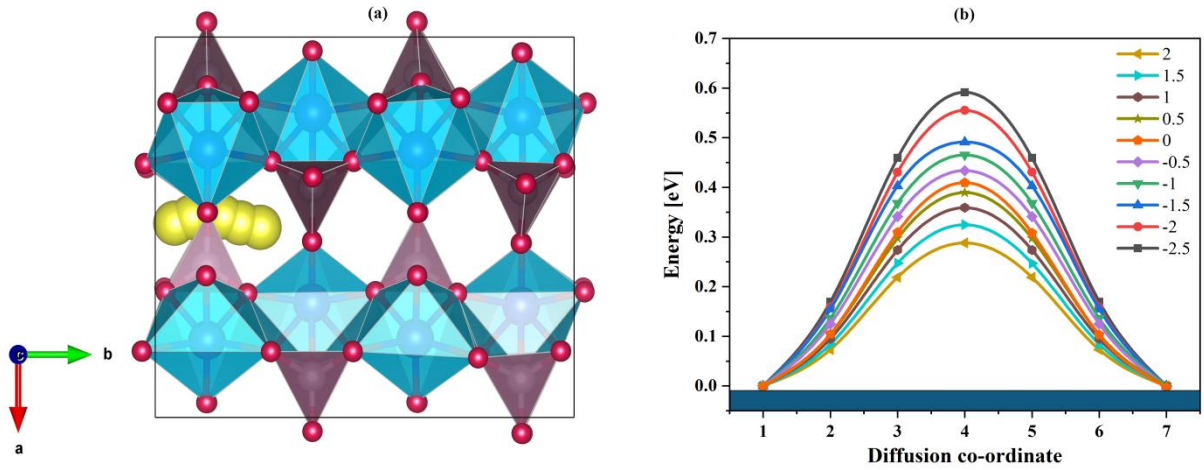

Figure 5.10: Migration paths of lithium ions in (a) unstrained and strained MP structures and (b) their corresponding energy profile.

Figure 5.10 shows the Li-ion diffusion pathway in unstrained and strained MP materials and their corresponding energy profiles. The energy barrier of Li-ion diffusion in unstrained MP structure is found to be 0.40 eV, which is in agreement with previously reported values [27, 165, 198]. This value increases and decreases with applied compressive and tensile strain, respectively. For instance, the activation barrier energy decreases from 0.59 to 0.28 eV when the applied strain changes from -2.5% to +2%, indicating a faster diffusion of Li-ion in MP compound with applied tensile strain compared to that of compressive strain. These findings show that lithium-ion diffusion can be enhanced substantially by applying tensile strain. This positive effect of tensile strain on the ionic conductivity has been observed also by Tealdi et al. on $LiFePO_4$ and $NaFePO_4$ olivines [176] and by Lee et al. for olivine $LiFePO_4$ [184]

To further understand the effect of biaxial strain on the ionic conductivity of LMP compound, the diffusion coefficients (D) of Li within unstrained and strained MP compounds were calculated using eq 3 and listed in Table 2. From this table, the calculated ratio of $\frac{Di}{D0\%}$ (with i= +0.5, +1, +1.5, or +2%) was found to be 2.1, 9, 22.5 or 107, respectively, which indicates

that the +2% biaxial tensile strain leads to 100 times increase in diffusion coefficients, ensuring that the tensile strain is beneficial for improving the ionic conductivity of LMP compound. This confirms that the application of tensile strain in the ac-plane perpendicular to the main diffusion path in olivine cathode materials is an efficient strategy to improve their ionic conductivity. The improvement of ionic conductivity under tensile strain can be attributed to the structural modifications. As discussed above, the volume gradually increases with increasing strain value, so this volume expansion leads to the increase of the structural space which allows the migration of Li-ion more easily. Furthermore, the average Li–O bond lengths are increased with increasing the tensile strain values (see Table1), suggesting that this tensile strain leads to weak bonding between Li and oxygen atoms. Consequently, the Li-ion migration barrier energy reduces with the applied tensile strain. Moreover, this enhancement in the ionic conductivity of Li-ions can be explained by the decrease in Pauli repulsion between Li-ions and octahedral MnO6, as reported in the literature [165].

Table 5.2: Activation Barrier Energies and Diffusion Coefficient for Li Diffusion Along the b-Axis in Unstrained and Strained MP Structures.

Compounds	activation barrier E_{act} [eV]	diffusion coefficient D [cm^2/s]
Li –ion in LMP (+2%)	**0.28**	**1.66×10^{-8}**
Li –ion in LMP (+1.5%)	**0.32**	**3.50×10^{-9}**
Li –ion in LMP (+1%)	**0.35**	**1.40×10^{-9}**
Li –ion in LMP (+0.5%)	**0.38**	**3.39×10^{-10}**
Li –ion in LMP (0%)	**0.40**	**1.55×10^{-10}**
Li –ion in LMP (-0.5%)	**0.43**	**4.84×10^{-11}**
Li –ion in LMP (-1%)	**0.46**	**1.50×10^{-11}**
Li –ion in LMP (-1.5%)	**0.49**	**4.69×10^{-12}**
Li –ion in LMP (-2%)	**0.55**	**4.53×10^{-13}**
Li –ion in LMP (-2.5%)	**0.59**	**9.56×10^{-14}**

5.3.6 Anti-Site Defects and Ion Migration

It is well-known that the most energetically favorable intrinsic defect in olivine-type structures is the intrinsic anti-site defects (eq 5.4 and Figure 5.11), in which a Li-ion (on 4a site) and a Mn ion (on 4c site) are interchanged [199, 200]

$$Li_{Li}^{\times} + Mn_{Mn}^{\times} \rightarrow Mn_{Li}^{\cdot} + Li_{Mn}^{\prime} \quad (5.4)$$

the formation of this defect has been observed experimentally. For instance, Guo et al. observed the presence of anti-site defects in olivine cathode materials by analysis of electron energy loss spectroscopy and high-angle annular dark-field [201]. This has been also noticed by using annular dark-field scanning transmission electron microscopy [202] and by synchrotron X-ray diffraction [203]. These types of defects are temperature dependent and therefore sensitive to the experimental synthesis conditions and particle size [199, 202, 204, 205].

Based on the experimental investigations, it can be concluded that the anti-site defects are intrinsic to olivine structures. Therefore, in order to examine the influence of Li/Mn intrinsic site-exchange defect in the charge/discharge processes of LMP compound, the diffusion of a single Li-ion in defective structure MP was evaluated. Figure 5.12 shows the Li-ion diffusion pathway in non-defective and defective MP structures, respectively. The calculated energy barrier of Li-ion diffusion in non-defective and defective MP structures is 0.40 and 1.12 eV, respectively. Comparing these values, we deduce that the anti-site defect increases drastically the barrier energy of Li-ion in the MP structure, implying that the presence of this defect in a channel of olivine structure severely impedes the lithium-ions diffusion and thereby affects the electrochemical performance of LMP as cathode material for LiBs. The obtained results are in trend with experimental and theoretical results, which also indicates that anti-site defects lead to a degradation of the electrochemical performance of the olivine cathode material [200, 202, 205, 206].

In addition to the influence of anti-site defect on the ionic conductivity of LMP, the effect of biaxial tensile strain on lithium kinetics in defective structure MP was also evaluated. The Li-ion diffusion in the defective-strained (+2%) MP structure was calculated and then compared with Li-ion migration in the defective-unstrained structure. The calculated migration barrier energy of Li-ions in unstrained/strained structures with the presence of anti-site defects is summarized in Table 3. It can be observed that the barrier energy increases from 0.40/0.28 to 1.12/0.37 eV for unstrained/strained (+2%) structures, suggesting the negative effect of the anti-site defect on Li-ion migration in unstrained MP compared to +2% strained MP. These results indicate that the biaxial tensile strain can mitigate the negative effect of anti-site defects on Li-ion migration. This reduction in the negative effect of the anti-site defect on the

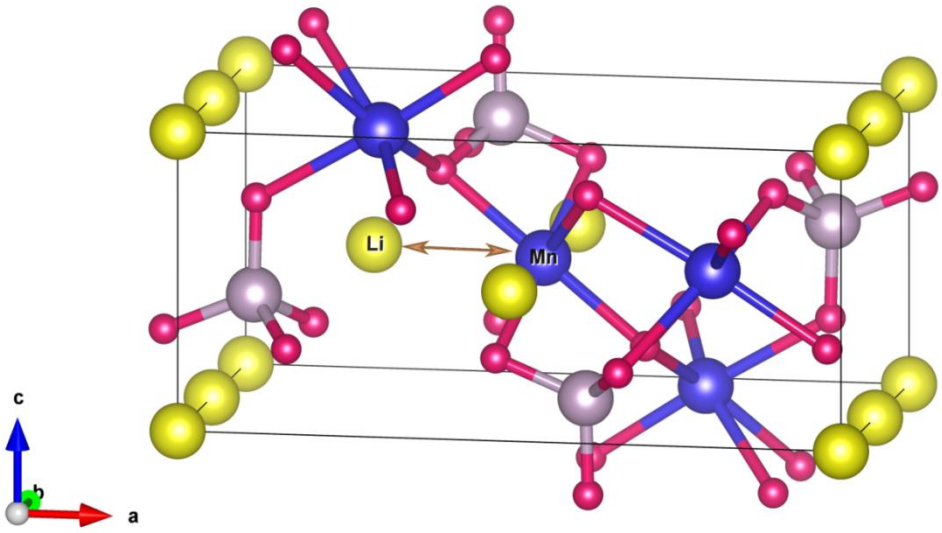

Figure 5.11: Schematic representation of Li/Mn anti-site defect in olivine-type LMP.

ionic conductivity can also be attributed to structural changes. As discussed above, the volume of the system gradually increases as the value of tensile strain increases. This increase in volume makes the Li-ion migration barrier less affected by the presence of an anti-site defect in one of the channels along [010] in the system.

Table 5.3: Activation Barrier Energies and Diffusion Coefficient for Li Diffusion Along the b-Axis in Unstrained and Strained Defective MP Structures.

Compounds	Activation barrier E_{act} [eV]	Diffusion Coefficient D [cm^2/s]
L-ion in unstrained MP	0.40	1.55×10^{-10}
Li-ion in defective unstrained MP	1.12	1.05×10^{-22}
Li-ion in strained MP (+2%)	0.28	1.66×10^{-8}
Li-ion in defective-strained MP (+2%)	0.37	1.61×10^{-9}

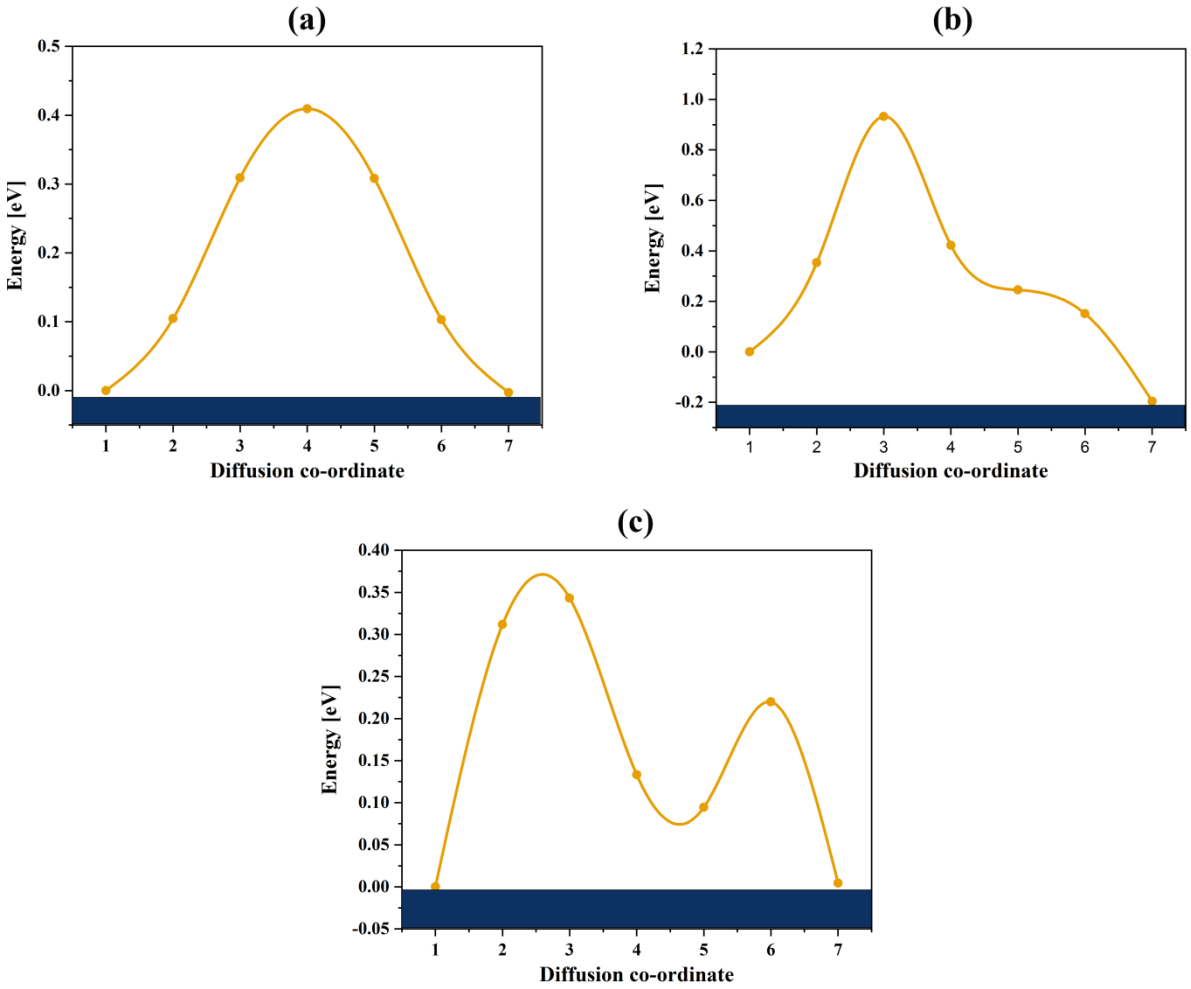

Figure 5.12: The energy profiles of lithium-ion diffusion in (a) non-defective MP structure, (b) defective MP structure, and (c) strained defective MP structure.

5.4 Chapter Summary

DFT calculations were carried out to investigate the effect of biaxial strain on the dynamic and thermal stabilities, structural, electronic, ionic diffusion, electrochemical potential, and defect properties of $LMnPO_4$ (LMP) structure, as well as on the average (Mn–O, Li–O and P–O) bond lengths, electrical conductivity, and charge transfer. The influence of anti-site defects on the ionic conductivity of LMP compound was also evaluated. The key results are as follows:

1. The results indicated that the unstrained and strained compounds (from -2.5 to +2%) are dynamically and thermally stable.
2. Electronic property analysis reported that the band gap ranges from 3.84 to 3.41 eV when the strain is applied from compressive -2.5% to tensile +2%, indicating that the

biaxial tensile strain can improve the electronic conductivity of LMP. The charge transfer and intercalation voltage of Li-ions in LMP is not affected by biaxial tensile strain to some extent.

3. The +2% biaxial tensile strain leads to a 100 times increase in diffusion coefficient, ensuring that the application of tensile strain in the ac-plane perpendicular to the main diffusion path in olivine cathode materials is an efficient strategy to improve their ionic conductivity. Furthermore, the migration barrier was calculated to be 0.37 eV for strained (+2%) defective MP, lower than 1.12 eV for unstrained defective MP, indicating that biaxial tensile strain can mitigate the negative effect of anti-site defects on Li-ion migration.

These results suggest that an appropriate biaxial strain can be an alternative strategy for improving the electronic and ionic conductivities and mitigates the negative effect of Li/M anti-site defect.

Chapter 6

Conclusions and Future Work

6.1 General Remarks

This thesis has described computer modelling studies of olivine cathode materials for Li-ion rechargeable batteries. This work has been motivated by the knowledge that emerging grid storage technologies of electric vehicles and grid storage require a new generation of batteries with excellent cathode materials, beyond the current commercial Li-ion cells. The development of these new batteries depends on the evolution of new materials and an understanding of their properties on a scale difficult to probe using experimental techniques. Using DFT calculations, a broad range of properties have been provided including structural, electronic, defect, diffusion, magnetic, capacity, charge transfer, and cell voltage. It is appropriate to conclude this thesis with a summary of the main results and conclusions, as well as suggesting possible future studies.

6.2 Nickel and iron single doped $LiMnPO_4$ as cathode materials for Li-Ion Batteries

In the **chapter 3** the structural, electronic, magnetic (total magnetization), electrochemical potential, and kinetic properties of mixed olivine phases $LiMn_{1-x}M_xPO_4$ / $Mn_{1-x}M_xPO_4$ (M= Ni, Fe; x=0, 0.25, 0.5, 0.75, 1) were investigated using DFT calculations.

Conclusions

The results indicated that the Ni and Fe substitutions notably affected the structural, electronic, and kinetic properties. So that, the volume of $LiMnPO_4$ (LMP) is decreased with increasing concentrations of Ni and Fe in Mn sites. Moreover, the band gap (E_g) of LMP (3.62 eV) is reduced with substitutions of Mn sites by Ni and Fe especially for the compounds $LiMn_{0.5}Ni_{0.5}PO_4$ (LMNP) (2.77 eV) and $LiMn_{0.5}Fe_{0.5}PO_4$ (LMFP) (3.35 eV) and then the electronic conductivity is increased. Furthermore, the diffusion barrier of Li-ion in $Mn_{0.5}Ni_{0.5}PO_4$ and $Mn_{0.5}Fe_{0.5}PO_4$ is 0.34 eV and 0.39 eV respectively which is lower than

pristine $MnPO_4$ (0.42 eV). Therefore 50% of Ni and Fe are beneficial to improve the kinetic properties in LMP. Moreover, Fe and Ni form a stronger bond length with O than Mn, which signifies a good improvement in structural stability of the doped LMP structures. According to this study, LMNP and LMFP could be great alternatives for $LiMnPO_4$ (LMP), $LiNiPO_4$ (LNP), and $LiFePO_4$ (LFP) as cathode materials of LIBs due to their good performances and abilities to overcome the main problems of olivines materials (ionic and electronic conductivity). These results are very important in improving the performance of LMP as a cathode material for LIBs and it is very useful to understand the effect of cation doping (Ni and Fe).

6.3 Ni-Fe co-doping to enhance the performance of $LiMnPO_4$ as cathode materials for Li-Ion Batteries

Chapter IV presents a study on the effect of Ni–Fe codoping (i.e. $LiMn_{0.5}Ni_{0.25}Fe_{0.25}PO_4$) on the structural, electronic, magnetic, electrochemical potential and kinetic properties of Li-ions in pristine LMP, as well as on the thermodynamic stability, theoretical capacity, charge transfer, average M–O bond lengths, and electrical conductivity. In addition, the thermodynamic stability and charge transfer of Ni/Fe single doping in lithiated/delithiated ($LiMnPO_4$/$MnPO_4$) pristine phases were examined, through the use of DFT calculations.

Conclusions

The calculations suggested that all compounds are thermodynamically stable. A small change in unit cell volume between lithiated and delithiated phases for all structures was observed, suggesting good reversibility during Li insertion/extraction. Electronic property analysis revealed that Ni–Fe codoping reduces the bandgap of LMP from 3.62 to 1.55 eV, indicating that Ni–Fe co-doping can improve the electronic conductivity of LMP. The theoretical capacity and intercalation voltage of Li-ions in pristine LMP are slightly affected by Ni–Fe co-doping. Furthermore, the migration barrier energy of Li-ion in MNFP (0.34 eV) is lower than that in MP (0.40 eV), implying that Ni–Fe codoping is beneficial for improving the ionic conductivity of Li-ion pristine MP. This study suggests that LMNFP could be a promising cathode material for high-performance lithium-ion batteries. Simultaneously, this study is crucial for better understanding the effect of Ni–Fe codoping on the performance of LMP as a cathode material for LIB batteries.

6.4 Strain effects on the electrochemical performance of $LiMnPO_4$

Chapter V provides a study on the effect of biaxial strain on the dynamic and thermal stabilities, structural, electronic, ionic diffusion, electrochemical potential, and defect properties of $LMnPO_4$ (LMP) structure, as well as on the average (Mn–O, Li–O, and P–O) bond lengths, electrical conductivity, and charge transfer. The influence of anti-site defects on the ionic conductivity of LMP compound was also evaluated, using DFT calculations.

Conclusions

The findings suggested that the unstrained and strained compounds (from -2.5 to +2%) are dynamically and thermally stable. In addition, the results suggest that the biaxial tensile strain has a remarkable effect on the rate performance of LMP cathode material. Electronic property analysis reported that the band gap ranges from 3.84 to 3.41 eV when the strain is applied from compressive -2.5% to tensile +2%, indicating that the biaxial tensile strain can improve the electronic conductivity of LMP. The charge transfer and intercalation voltage of Li-ions in LMP is not affected by biaxial tensile strain to some extent. Moreover, the +2% biaxial tensile strain leads to a 100 times increase in diffusion coefficient, ensuring that the application of tensile strain in the ac-plane perpendicular to the main diffusion path in olivine cathode materials is an efficient strategy to improve their ionic conductivity. Furthermore, the migration barrier was calculated to be 0.37 eV for strained (+2%) defective MP, lower than 1.12 eV for unstrained defective MP, indicating that biaxial tensile strain can mitigate the negative effect of anti-site defects on Li-ion migration. This study suggests that an appropriate biaxial strain is an alternative strategy for improving the electronic and ionic conductivities and mitigates the negative effect of Li/M anti-site defect.

6.5 Future Work

- Previous works have shown that single and co-doping on the transition metal site of LMP cathode material can improve its ionic and electronic conductivities. Therefore, divalent transition metals (Co^{2+}, Ni^{2+} and Fe^{2+}) should be incorporated into the Mn site to determine if this incorporation could be used to further improve the rate performance of LMP. For example, Co^{2+} could be incorporated in small concentrations into the Mn site due to its toxicity.

- Investigate the defect and migration properties of both the olivine and maricite forms of

NaMnPO4.

- Examine the effect of both doping and codoping strategies on the defect properties of LMP.

- Investigate other cathode materials including layered oxides, spinel structures using DFT calculations.

References

[1] Khossossi, Nabil.; Benhouria, Younes.; Naqvi, Syeda R.; Panda, Pritam K.; Essaoudi, Ismail.; Ainane, Abdelmajid.; Ahuja, Rajeev. Sustain. Energy Fuels. 2020, 4 (9), 4538–4546.

[2] Aman, M. M.; Solangi, K. H.; Hossain, M. S.; Badarudin, A.; Jasmon, G. B.; Mokhlis, H.; Bakar, A. H.A.; Kazi, S. N. Renew. Sustain. Energy Rev. 2015, 41, 1190–1204.

[3] Islam, M. R.; Mekhilef, S.; Saidur, R. Renew. Sustain. Energy Rev. 2013, 21, 456–468.

[4] Balat, M.; Balat, H.; Faiz, U. Energy Sources, Part B Econ. Plan. Policy. 2009, 4 (3), 95–309.

[5] Maymoun. M.; Elomrani, A.; Oukahou. S.; Bahou. Y.; Hasnaoui. A.; Sbiaai. K. Phys. Chem. Chem. Phys. 2023, 25, 3401–3412.

[6] He, Qiu.; Yu, Bin.; Li, Zhaohuai.; Zhao, Yan. Energy Environ. Mater. 2019, 2 (4), 264–279.

[7] Miao, Yu.; Hynan, Patrick.; Von Jouanne, Annette.; Yokochi, Alexandre. Energies. 2019, 12 (6), 1–20.

[8] Gummow, R. J.; He, Y. J. Power Sources. 2014, 253, 15–331.

[9] Nitta, N.; Wu, F.; Lee, J.T.; Yushin, G. Mater. Today. 2014, 18 (5), 252–264.

[10] Shi, J.; Wang, Z.; Fu, Y.Q. J. Phys. D. Appl. Phys. 2016, 49 (50), 505601.

[11] J Padhi, A. K.; Nanjundaswamy, K.S.; Goodenough, J.B. J. Electrochem. Soc. 1997, 144 (4), 1188–1194.

[12] Zhang. Xiaoxiao.; Li. Li.; Fan. Ersha.; Xue. Qing.; Bian. Yifan.; Wu. Feng.; Chen. Renjie. Chem. Soc. Rev. 2018, 47 (19), 7239–7302.

[13] *Mathewa, V.; Alfaruqia, M. H.; Gima, J.; Songa, J.; Kima, S.; Ahnb, D.; Kim, J. Mater. Charact. 2014, 89, 93–101.*

[14] [15] Snydacker, D. H.; Wolverton, C. J. Phys. Chem. C. 2016, 120 (11), 5932–5939.

[15] Oh, B. S. M.; Oh, S. W.; Yoon, C. S.; Scrosati, B.; Khalil, A.; Sun, Y. K. Adv. Funct. Mater. 2010,20 (19), 3260–3265.

[16] Li, G.; Azuma, H.; Tohda, M. Solid-State Lett. 2002, 5 (6), 135–137.

[17] Aravindan, V.; Gnanaraj, J.; Lee, Y. S.; Madhavi, S. J. Mater. Chem. A. 2013, 1(11),

3518-3539.

[18] Phan, A. T.; Gheribi, A. E.; Chartrand, P. J. Alloys Compd. 2020, 838, 155550.

[19] Kim, M. S.; Jegal, J. P.; Roh, K. C.; Kim, K. B. J. Mater. Chem. A. 2014, 2 (27), 10607–10613.

[20] Delacourt, C.; Laffont, L.; Bouchet, R.; Wurm, C.; Leriche, J. B.; Morcrette, M.; Tarascon, J. M.; Masquelier, C. J. Electrochem. Soc. 2005, 152 (5), A913.

[21] Wang, C.; Li, S.; Han, Y.; Lu, Z. ACS Appl. Mater. Interfaces. 2017, 9 (33), 27618–27624.

[22] Lv, T.; Min, H.; Shu, H.; Zhou, Y.; Liang, Q.; Li, Xiaolong.; Ren, Q.; Ma, Z.; Wang, X. Electrochim. Acta 2020, 359, 136945.

[23] Oukahou, S.; Elomrani, A.; Maymoun, M.; Sbiaai, K.; Hasnaoui, A. J.Computational Materials Science 2022, 202, 1–11.

[24] Whittaker, Carly.; McManus, Marcelle C.; Hammond, Geoffrey P. Energy Policy. 2011, 39 (10), 5950–5960.

[25] Islam, M. Saiful. J. Mater. Chem. 2007, 17 (30), 3069–3070.

[26] Zhang. Xiaoxiao.; Li. Li.; Fan. Ersha.; Xue. Qing.; Bian. Yifan.; Wu. Feng.; Chen. Renjie. Chem. Soc. Rev. 2018, 47 (19), 7239–7302.

[27] Alfaruqi, M. H.; Kim, S.; Park, S.; Lee. S.; Lee, J.; Hwang, J. Y.; Sun, Y. K.; Kim. J. ACS Appl. Mater. Interfaces. 2020, 12 (14), 16376–16386.

[28] Tarascon, J. M.; Armand, M. Appl. Radiol. 2001, 414(2), 359–367.

[29] Mong, Anh Le.; Shi, Qing Xuan.; Jeon, Hyungjoon.; Ye, Yun Sheng.; Xie, Xiao Lin.; Kim, Dukjoon. Adv. Funct. Mater. 2021, 31(12), 1–47.

[30] Synthesis, Selective. Cryst. Growth Des. 2008, 8(12), 2–6.

[31] Islam, M. Saiful.; Fisher, Craig A.J. Lithium and sodium battery cathode materials: Computational insights into voltage, diffusion and nanostructural properties. Chem. Soc. Rev. 2014, 43 (1), 185–204.

[32] J.-M. Tarascon.; M. Armand,.Nature. 2009, 414, 167–170.

[33] Bruce, Peter G. Chem. Commun. 1997, 19, 1817–1824.

[34] Korthauer, Reiner. Springer Berlin Heidelberg, Berlin, Heidelberg. 2018, 1-413.

[35] Wang, Y.; Cheng, T.; Yu, Z. Er.; Lyu, Y.; Guo, B. J. Alloys Compd. 2020, 842, 155827 .

[36] Whittingham, M. Stanley. Chem. Rev. 2004, 104(10), 4271–4301.

[37] Palacín, M. Rosa. Chem. Soc. Rev. 2009, 38(9), 2565–2575.

[38] Sauvage, F.; Laffont, L.; Tarascon, J. M.; Baudrin, E. J. Power Sources. 2008, 175 (1),

495–501.

[39] Ignatiev, Alex.; Chen, Xin.; Wu, Naijuan.; Lu, Zigui.; Smith, Laverne. Dalt. Trans. 2008, 40, 5501–5506.

[40] Tarascon, J. M.; Armand, M. Nature. 2001, 414 (6861), 359–367.

[41] Park, Cheol Min.; Kim, Jae Hun.; Kim, Hansu.; Sohn, Hun Joon. Chem. Soc. Rev. 2010, 39 (8), 3115–3141.

[42] Li, Hong.; Huang, Xuejie.; Chen, Liquan. Solid State Ionics. 1999, 123(1), 189–197.

[43] Idota, Yoshio.; Kubota, Tadahiko.; Matsufuji, Akihiro.; Maekawa, Yukio.;Miyasaka, Tsutomu. Science. 1997, 276 (5317), 1395–1397.

[44] Poizot, P.; Laruelle, S.; Grugeon, S.; Dupont, L.; Tarascon, J. M. Nature. 2000, 407(6803), 496–499.

[45] Xu, Wu.; Canfield, Nathan L.; Wang, Deyu.; Xiao, Jie.; Nie, Zimin.; Zhang, Ji Guang. J. Power Sources. 2010, 195 (21), 7403–7408.

[46] Ji, Liwen.; Lin, Zhan.; Alcoutlabi, Mataz.; Zhang, Xiangwu. Energy Environ. Sci. 2011, 4(8), 2682–2689.

[47] Deng, Da.; Kim, Min Gyu.; Lee, Jim Yang.; Cho, Jaephil. Energy Environ. Sci. 2009, 2 (8), 818–837,.

[48] Shoufeng Yang.; Peter Y.Zavalij.; M. Stanley Whittingham. Electrochem. commun. 2018, 3, 21–23.

[49] Gardiner, Grahame. University of Bath. 2012.

[50] K. Mizushima.; P.C. Jones.; P.J. Wiseman.; J.B. Goodenough. Japanese J. Appl. Physics. 2003, 42 (9). 6131–6134.

[51] Ozawa, Kazunori. Solid State Ionics. 1994, 69, 212–221.

[52] Bruce, Peter G. Solid State Ionics. 2008, 179, 752–760.

[53] Thackeray, M. M.; David, W. I.F.; Bruce, P. G.; Goodenough, J. B. Mater. Res. Bull. 1983, 18 (4), 461–472.

[54] Qiming Zhong.; Arman Bonakclarpour.; Meijie Zhang.; Yuan Gao.; J. R. Dahn. J. Electrochem. Soc. 2007, 144 (1), 2688–2693.

[55] Kunduraci, M.; Al-Sharab, Jf.; Amatucci, Gg. Chem. Mater. 2006, 18 (15), 3585–3592.

[56] Oukahou, S.; Elomrani, A.; Maymoun, M.; Sbiaai, K.; Hasnaoui, A. J.Computational Materials Science 2022, 202, 1–11.

[57] Jung, Jongboo.; Cho, Maenghyo.; Zhou, Min. J. Power Sources. 2013, 243, 706–714.

[58] Ahsan, Zishan.; Ding, Bo.; Cai, Zhenfei.; Wen, Cuie.; Yang, Weidong.; Ma, Yangzhou.; Zhang, Shihong. J. Electrochem. Energy Convers. Storage. 2021, 18 (1),

010801.

[59] Tolganbek, Nurbol.; Yerkinbekova, Yerkezhan.; Kalybekkyzy, Sandugash.; Bakenov, Zhumabay.; Mentbayeva, Almagul. J. Alloys Compd. 2021, 882, 160774.

[60] Liu, Yadong.; Liu, Qi.; Li, Zhefei.; Ren, Yang.; Xie, Jian.; He, Hao.; Xu, Fan. J. Electrochem. Soc. 2014, 161 (4), A620–A632.

[61] Mauger, Alain.; Julien, Christian M. Julien. Batteries. 2018, 4 (3), 1–32.

[62] N Lethole, N. L.; Ngoepe, P. E.; Chauke, H. R. Comput. Condens. Matter, 2020, 22, e00437.

[63] Osnis, A.; Kosa, M.; Aurbach, D.; Major, D. T. J. Phys. Chem. C. 2013, 117 (35), 17919–17926.

[64] Z Li, Zhaojin.; Yang, Jinxing.; Guang, Tianjia.; Fan, Bingbing.; Zhu, Kongjun Wang, Xiaohui. Small Methods. 2021, 5 (6), 1–24.

[65] Zhao, Qun Fang.; Zhang, Shu Qiong.; Hu, Min Yi.; Wang, Chang.; Jiang, Guang Hui. Int. J. Electrochem. Sci. 2021, 16, 1–10.

[66] Dees, Dennis W.; Kawauchi, Shigehiro.; Abraham, Daniel P.; Prakash, Jai. J. Power Sources. 2009, 189 (1), 263–268.

[67] Yu, Denis Y. W.; Fietzek, Christopher.; Weydanz, Wolfgang.; Donoue, Kazunori.; Inoue, Takao.; Kurokawa, Hiroshi.; Fujitani, Shin. J. Electrochem. Soc. 2007, 154 (4), A253.

[68] Urban, Alexander.; Seo, Dong Hwa.; Ceder, Gerbrand. npj Comput. Mater. 2016, 2, 16002.

[69] Ju, Seo Hee.; Kang, Yun Chan. Mater. Chem. Phys. 2008, 107, 328–333.

[70] Konarova, Muxina.; Taniguchi, Izumi. Mater. Res. Bull. 2008, 43(12), 3305–3317.

[71] Wang, G. X.; Bewlay, Steve.; Yao, Jane.; Ahn, J. H.; Dou, S. X.; Liu, H. K. Electrochem. Solid-State Lett. 2004, 7 (12), 506–509.

[72] Arnold, G.; Garche, J.; Hemmer, R.; Ströbele, S.; Vogler, C.; Wohlfahrt-Mehrens, M. J. Power Sources. 2003, 119–121, 247–251.

[73] Long, Yunfei.; Zhang, Zhihua.; Wu, Zhi.; Su, Jing.; Lv, Xiaoyan.; Wen, Yanxuan. Particuology. 33, 42–49, 2017.

[74] Sukkabot, W. Phys. Scr. 2020, 95 (4), 045811.

[75] Gao, Yuan.; Xiong, Kun.; Zhang, Haidong.; Zhu, Bingfeng. ACS Omega. 2021, 6 (22), 14122–14129.

[76] Cui, Zhihong.; Guo, Xin.; Ren, Junqiang.; Xue, Hongtao.; Tang, Fuling.; La, Peiqing.; Li, Hui.; Li, Junchen.; Lu, Xuefeng. Electrochim. Acta. 2021, 388, 38592.

[77] Wang, Li.; Li, Yin.; Dai, Yongnian.; Yao, Yaochun.; Zhang, Keyu . j. vacuum. 2022, 196, 110730.

[78] El-Khalfaouy, Redouan.; Turan, Servet.; Rodriguez, Miguel A.; Dermenci, Kamil Burak.; Savacı, Umut.; Addaou, Abdellah.; Laajeb, Ali.; Lahsini, Ahmed. J. Appl. Electrochem. 2021, 51 (4), 681–689.

[79] Gao, Libin.; Xu, Zhengrui.; Zhang, Shu. J. Alloys Compd.739, 529–535, 2018.

[80] Yi, Huihua.; Hu, Chenglin.; He, Xiangming.; Xu, Hongyun. Ionics (Kiel). 2015, 21(3), 667–671.

[81] Huang, Yimeng.; Dong, Yanhao.; Li, Sa.; Lee, Jinhyuk.; Wang, Chao Zhu, Zhi.; Xue, Weijiang.; Li, Yao.; Li, Ju . Adv. Energy Mater. 2021, 11(2), 1–21..

[82] He, Ping.; Wang, Haoran.; Qi, Lu.; Osaka, Tetsuya . J. Power Sources. 2006, 160 (1), 627–632.

[83] Liang, Longwei.; Hu, Guorong.; Jiang, Feng.; Cao, Yanbing . J. Alloys Compd. 2016, 657, 570–581.

[84] Wu, Naiteng.; Wu, Hao.; Yuan, Wei.; Liu, Shengjie.; Liao, Jinyu.; Zhang, Yun . J. Mater. Chem. A. 2015, 3 (26), 13648–13652.

[85] Lee, Min Joon.; Lee, Sanghan.; Oh, Pilgun.; Kim, Youngsik.; Cho, Jaephil . Nano Lett. 2014, 14 (2), 993–999.

[86] Zhang, Wei Jun . J. Power Sources. 2011, 196 (6), 2962–2970.

[87] S Martha, S. K.; Grinblat, J.; Haik, O.; Zinigrad, E.; Drezen, T.; Miners, J. H.; Exnar, I.; Kay, A.; Markovsky, B.; Aurbach, D. Angew. Chem. Int. Ed. 2009, 48, 8559 – 8563.

[88] Xie, Qian.; Zhu, Jihua.; Wang, Chengyun.; Fang, Kaibin.; Yang, Wei.; Liu, Quanbing.; Wang, Yali.; Chen, Shengzhou. Chinese J. Chem. Eng. 2021, 36, 181–189.

[89] Zhao, Huifang.; Yu, Yong.; Wang, Guojing.; Chen, Yunchao.; Liu, Xiaomin.; Yang, Hui. Funct. Mater. Lett. 2018, 11(5), 850037.

[90] Allen, J. L.; Jow, T. R.; Wolfenstine, J. J. Power Sources. 2011, 196 (20), 8656–8661.

[91] Taddesse, Paulos.; Berie, Alemken.; Babu, K. Vijaya . J. Mol. Struct. 2020, 1219,128593.

[92] Bagayoko, Diola. AIP Adv. 2014, 4 (12), 0–12, 127104.

[93] Gross, Axel. Theoretical surface science . A Microscopic Perspective. Originally published in the series: Advanced Texts in Physics. 2003, 132 .

[94] Holton, G. 1984, 162–163.

[95] Prodans, E.; Kohn, W. PNAS. 2005, 102 (33), 11635–11638.

[96] Hohenbergt, P. Integr. Equations Oper. Theory. 2001, 40 (4), 391–402.

[97] Schrödinger, E. Phys. Rev. 1926, 28 (6), 1049–1070.

[98] Wu, Zhigang.; Cohen, R. E. Phys. Rev. B - Condens. Matter Mater. Phys. 2006, 73 (23), 2–7.

[99] Perdew, John P.; Wang, Yue. Phys. Rev. B. 2018, 98(7), 244–249.

[100] Perdew, John P.; Burke, Kieron.; Ernzerhof, Matthias. Phys. Rev. Lett. 1996, 77(18), 3865–3868.

[101] Anisimov, Vladimir I.; Zaanen, Jan.; Andersen, Ole K. Phys. Rev. B. 1991, 44 (3), 943–954.

[102] Claisse, Antoine.; Klipfel, Marco.; Lindbom, Niclas.; Freyss, Michel

Olsson, Pär. J. Nucl. Mater. 2016, 478, 119–124.

[103] Bloch, Felix. Zeitschrift für Phys. 1929, 52, 555–600.

[104] Blöchl, P. E. Phys. Rev. B. 1994, 50 (24), 17953–17979.

[105] hi Nhu Tranh, Duong.; Van Hoang, Vo. EPJ Appl. Phys. 2015, 70 (1), 1–7.

[106] Pack, Hendrik J. Monkhorst.; James D. J. Mater. Chem. A. 2019, 7 (5), 2156–2164.

[107] Troullier, N.; Martins, José Luriaas . Phys. Rev. B. 1991, 43 (3), 1993–2006.

[108] Giannozzi, P.; Baroni, S.; Bonini, N.; Calandra, M.; Car, R.; Cavazzoni, C.; Ceresoli, D.; Chiarotti, G. L.; Cococcioni, M.; Dabo, I.; Corso, A. D.; Gironcoli, S. d.; Fabris, S.; Fratesi, G.; Gebauer, R.; Gerstmann, U.; Gougoussis, C.; Kokalj, A.; Lazzeri, M.; Samos, L. M.; Marzari, N.; Mauri, F.; Mazzarello, R.; Paolini, S.; Pasquarello, A.; Paulatto, L.; Sbraccia, C.; Scandolo, S.; Sclauzero, G.; Seitsonen, A. P.; Smogunov, A.; Umari, P.; Wentzcovitch, R. M. J. Phys. Condens. Matte. 2009, 21 (39), 395502.

[109] Momma, K.; Izumi, F. J. Appl. Crystallogr. 2011, 44 (6), 1272–1276.

[110] Balakrishnan, P. G.; Ramesh, R.; Prem Kumar, T. J. Power Sources. 2006, 155(2), 401–414.

[111] Henkelman, G.; Arnaldsson, A.; Jónsson, H. Comput. Mater. Sci. 2006, 36 (3), 354–360.

[112] Sheppard, Daniel.; Terrell, Rye.; Henkelman, Graeme. J. Chem. Phys. 2008, 128 (13), 134106.

[113] Jiang, J.; Dahn, J. R. Electrochem. commun. 2004, 6 (1), 39–43.

[114] ong, Zhengliang.; Yang, Yong. Energy Environ. Sci. 2011, 4(9), 3223–3242.

[115] W.F. Howard, R.M. Spotnitz, Theoretical evaluation of high-energy lithium metal phosphate cathode materials in Li-ion batteries, J. Power Sources. 2007, 165(2), 887 891.

[116] Kandhasamy, Sathiyaraj.; Nallathamby, Kalaiselvi.; Minakshi, Manickam. Prog. Solid State Chem. 2012, 40, 1–5.

[117] Zong, Jun.; Liu, Xingjiang. Electrochim. Acta. 2014, 116, 9–18.

[118] Li, Huiqiao.; Zhou, Haoshen.Chem. Commun. 2012, 48, 1201–1217.

[119] Kwon, Nam Hee.; Drezen, Thierry.; Exnar, Ivan.; Teerlinck, Ivo.; Isono, Motoshi.; Graetzel, Michael. Electrochem. Solid-State Lett. 2006, 9 (6), A277-A280.

[120] Bakenov, Zhumabay.; Taniguchi, Izumi. J. Electrochem. Soc. 2010, 157, 430-436.

[121] Wang, D.; Ouyang, C.; Drézen, T.; Exnar, I.; Kay, A.; Kwon, N. H.; Gouerec, P.; Miners, J. H.; Wang, M.; Grätzela, M. J. Electrochem. Soc. 2010, 157 (2), A225–A229.

[122] Wu, Ling; Zhong, Shengkui.; Lu, Jiajia.; Liu, Jiequn.; Lv, Fan. Ionics. 2013, 19 (7), 1061–1065.

[123] Fang, Haisheng.; Yi, Huihua.; Hu, Chenglin.; Yang, Bin.; Yao, Yaochun.; Ma, Wenhui.; Dai, Yongnian. Electrochim. Acta. 2012, 71, 266–269.

[124] F Zhou, F.; Kang , K.; Maxisch, T.; Ceder, G.; Morgan, D. Solid State Commun. 2004, 132 (3-4), 181–186.

[125] Yi, T. F.; Fang, Z. K.; Xie, Y.; Zhu, Y. R.; Dai. C. J. Alloys Compd. 2014, 617, 716–721.

[126] Nie, Z. X.; Ouyang,, C. Y.; Chen, J. Z.; Zhong, Z.Y.; Du, Y. L.; Shi, S. Q.; Lei, M. S. Solid State Commun. 2010, 150 (1-2), 40–44.

[127] Wang, L.; Maxisch, T.; Ceder, G. Phys. Rev. B - Condens. Matter Mater. Phys. 2006, 73 (19), 195107.

[128] Perdew, J. P.; Ruzsinszky , A.; Csonka , G. I.; Vydrov, O. A.; Scuseria, G. E.; Constantin, L. A.; Zhou, X.; Burke, K. Phys. Rev. Lett. 2008, 100 (13), 136406.

[129] *Dai, Y. H. SIAM J. Optim. 2003, 13 (3), 693–701*.

[130] Henkelman, G.; Uberuaga, B. P.; Jónsson, H. J. Chem. Phys. 2000, 113, 9901-9904

[131] Elomrani, A.; Lamhani, M.; Oukahou, S.; Sbiaai, K.; Lebègue, S.; Hasnaoui. A. Materials Chemistry and Physics. 2021, 275, 125191.

[132] Santoro, R. P. Acta Crystallogr. 1967, 22 (3), 344–347.

[133] Tang and W. Holzwarth, Electronic structure of $FePO_4$, $LiFePO_4$, and related materials, Phys. Rev. B - Condens. Matter Mater. Phys. 2003, 68 (16), 1–10.

[134] Wang , L.; Li , Y.; Wu, J.; Liang, F.; Zhang, K.; Xu, R.; Wan, H.; Dai, Y.; Yao, Y. Journal of Alloys and Compounds. 2020, 839, 155653.

[135] Julien, C. M.; Mauger, A.; Zaghib, K.; Veillette, R.; Groult, H. Ionics. 2012, 18 (7) 625–633.

[136] Xu, Jing.; Chen, Gang. Phys. B Condens. Matter. 2010, 405(3), 803–807.

[137] Zhou, F.; Cococcioni, M.; Kang, K.; Ceder, G. Electrochem. commun. 2004, 6 (11), 1144–1148.

[138] Zhou, F.; Cococcioni, M.; Marianetti, C. A.; Morgan, D.; Ceder.G. Phys. Rev. B. 2004, 70 (23), 235121.

[139] Saravanan, K.; Ramar, V.; Balaya, P.; Vittal, J. J. J. Mater. Chem. 2011, 21 (38), 14925–14935.

[140] Ottmann, A.; Jähne, C.; Meyer, H. P.; Klingeler, R.Mater. Res. Bull. 2015, 63, 6–12.

[141] Yi, T. F.; Peng , P. P.; Fang , Z.; Zhu, Y. R.; Xie, Y.; Luo, S. Compos. Part B Eng. 2019, 175, 107067.

[142] Seo, Inseok.; Senthilkumar, B.; Kim, Kwang Ho.; Kim, Jae Kwang.; Kim, Youngsik.; Ahn, Jou Hyeon. J. Power Sources. 2016, 320, 59–67.

[143] Galakhov, V. R.; Mesilov, V. V.; Shamin, S. N.; Urusova, N. V.; Barykina, Yu A.; Kellerman, D. G. Phys. Status Solidi Basic Res. 2017, 254 (4), 1–6.

[144] Kellerman, D.; Medvedeva, N.; Mukhina, N.; Semenova, A.; Baklanova, I.; Perelyaeva, L.; Gorshkov, V.. Phys. Lett. 2014, 591, 21–24.

[145] Madsen, G. K. H.; Singh, D. J. BoltzTraP. Phys. Commun. 2006, 175 (1), 67–71.

[146] Hu, LingjunQiu, Bao.; Xia, Yonggao.; Qin, Zhihong.; Qin, Laifen.; Zhou, Xufeng.; Liu, Zhaoping. Solvothermal synthesis of Fe-doping $LiMnPO_4$ nanomaterials for Li-ion batteries. J. Power Sources. 2014, 248, 246–252.

[147] Aydinol, M.; Kohan, A.; Ceder, G.; Cho, K.; Joannopoulos, J. Phys. Rev. B. 1997,56 (3),1354.

[148] T. Muraliganth, A. Manthiram. J. Phys. Chem. C. 114 (2010) 15530–15540.

[149] Whiteside, Alexander.; Fisher, Craig A.J.; Parker, Stephen C.; Saiful Islam, M. Phys. Chem. Chem. Phys. 2014, 16 (39), 21788–21794.

[150] Persson, Kristin.;Sethuraman, Vijay A.; Hardwick, Laurence J.; Hinuma, Yoyo. J. Phys. Chem. 2010, 1, 1176–1180.

[151] Zou, B.; Yu , R.; Deng , M.; Zhou, Y.; Liaoa, J.; Chen, C. RSC Adv. 2016, 6 (57), 52271–52278.

[152] Liu, T.; Xia, Q.; Lu, W.; Xu, J.; Wu, X. Electrochim. Acta 2015, 174 (1), 120–126.

[153] Huang, Q. Y.; Wu, Z.; Su, J.; Long, Y. F.; Lv, X. Y.; Wen, Y. X. Ceram. Int. 2016, 42 (9), 11348–11354.

[154] Ramar, V.; Balaya, P. Phys. Chem. Chem. Phys. 2013, 15 (40), 17240–17249.

[155] Paier, J.; Hirschl, R.; Marsman, M.; Kresse, G. J. Chem. Phys. 2005,122 (23), 234102.

[156] Marzari , N.; Vanderbilt, D.; Vita, A. D.; Payne, M. C. Phys. Rev. Lett. 1999, 82 (16), 3296–3299.

[157] Vineyard, G. H. J. Phys. Chem. Solids. 1957, 3 (1-2), 121–127.

[158] Hu , C.; Yi, H.; Fang, H.; Yang, B.; Yao, Y.; Ma, W.; Dai, Y. commun. 2010, 12 (12), 1784–1787.

[159] L. F. J. Piper.; Quackenbush, N. F.; Sallis. S.; Scanlon, D. O.; Watson, G. W.; Nam , K. W.; Yang, X. Q.; Smith, K. E.; Omenya, F.; Chernova , N. A.; Whittingham , M. S. J. Phys. Chem. C. 2013, 117, 10383–10396.

[160] Lei, Z.; Wang , J.; Yang, J.; Nuli, Y.; Ma, Z. ACS Appl. Mater. Interfaces. 2018, 10 (50), 43552–43560.

[161] Mishima, Y.; Hojo, T.; Nishio, T.; Sadamura, H.; Oyama, N.; Moriyoshi, C.; Kuroiwa, Y. J. Phys. Chem. C. 2013, 117 (6), 2608–2615.

[162] Maymoun. M.; Elomrani, A.; Oukahou. S.; Bahou. Y.; Hasnaoui. A.; Sbiaai. K. Phys. Chem. Chem. Phys. 2023, 25, 3401–3412.

[163] Xie, Y.; Yu, H. T.; Yi , T. F.; Zhu Y. R. ACS Appl. Mater. Interfaces. 2014, 6 (6), 4033-4042.

[164] Kim, S. W.; Kim, J.; Gwon, H.; Kang. K. J. Electrochem. Soc. 2009, 156 (8), A635-A638.

[165] Sgroi, M. F.; Lazzaroni, R.; Beljonne, D.; Pullini, D. Batteries. 2017, 3 (2), 1–10.

[166] Bakenov, Z.; Taniguchi, I. Open Mater. Sci. J. 2011, 5, 222–227.

[167] Dathar, G. K. P.; Sheppard, D.; Stevenson, K. J.; Henkelman, G. Chem. Mater. 2011, 23 (17), 4032–4037.

[168] Martha , S. K.; Markovsky, B.; Grinblat, J; Gofer. Y.; Haik . O; Zinigrad, E.; Aurbach, D.; Drezen, T.; Wang, D.; Deghenghi, G.; Exnar, I. J. Electrochem. Soc. 2009, 156 (7), A541-A552.

[169] Jarolimek, K.; Risko, C. ACS Appl. Mater. Interfaces. 2021, 13 (24), 29034-29040.

[170] Morgan , D.; Van der Ven, A.; Ceder, G. Electrochem. Solid-State Lett 2004, 7 (2), A30-A32.

[171] Zheng, Zhipeng.; Wu, Li.; Han, Yuqiu.; Chen, Jun.; Zhu, Shuai.; Yao.; Yuanyuan.; Wang, Baohong.; Li, Lanjuan. Engineering. 2022, 14, 134-146.

[172] Oukahou, Said.; Maymoun, Mohammad.; Elomrani, Abdelali.; Sbiaai, Khalid.; Hasnaoui, Abdellatif . ACS Appl. Energy Mater. 2022, 5 (9), 10591–10603.

[173] Drezen, Thierry.; Kwon, Nam Hee.; Bowen, Paul.; Teerlinck, Ivo.; Isono.; Motoshi.; Exnar, Ivan. J. Power Sources. 2007, 174 (2), 949–953.

[174] Han, Jing.; Yang, Jun.; Xu, Zhixin.; Li, Hongping.; Wang, Jiulin. J. Alloys Compd. 2022, 894, 162510.

[175] Zaghib, K.; Guerfi, A.; Hovington, P.; Vijh, A.; Trudeau, M.; Mauger, A.; Goodenough, J. B.; Julien, C. M. J. Power Sources. 2013, 232, 357–369.

[176] Tealdi, Cristina.; Heath, Jennifer.; Islam, M. Saiful. J. Mater. Chem. A. 2016, 4 (18), 6998–7004.

[177] Nabeshima, Fuyuki.; Imai, Yoshinori.; Hanawa, Masafumi.; Tsukada.; Ichiro.; Maeda, Atsutaka. Appl. Phys. Lett.2013, 103 (17), 0–4.

[178] Haeni, J. H.; Irvin, P.; Chang, W.; Uecker, R.; Reiche, P.; Li, Y. L.; Choudhury, S.; Tian, W.; Hawley, M. E.; Craigo, B.; Tagantsev, A. K; Pan, X. Q.; Streiffer, S. K.; Chen, L. Q.; Kirchoefer, S. W.; Levy, J.; Schlom, D. G. Nature. 2004, 430 (7001), 758–761.

[179] Kushima, Akihiro.; Yildiz, Bilge. J. Mater. Chem. 2010, 20 (23), 4809–4819.

[180] Pennycook, Timothy J.; Beck, Matthew J.; Varga, Kalman.; Varela, Maria.; Pennycook, Stephen J.; Pantelides, Sokrates T. Phys. Rev. Lett. 2010,104 (11),1–4.

[181] Janek, J.; Martin, M.; Becker, K. D. Phys. Chem. Chem. Phys. 2009,11 (17), 3010.

[182] Sata, N.; Eberman, K.; Eberl, K.; Maier, J. Nature. 2000, 408 (6815), 946–949.

[183] Shahid, Raza.; Murugavel, Sevi. Phys. Chem. Chem. Phys. 2013, 15 (43), 18809–18814.

[184] Lee, Jaekwang.; Pennycook, Stephen J.; Pantelides, Sokrates T. Appl. Phys. Lett. 2012, 101(3), 1–5.

[185] A. Togo and I. Tanaka, “First principles phonon calculations in materials science,” Scr. Mater., vol. 108, pp. 1–5, 2015.

[186] De Klerk, Niek J.J.; Van Der Maas, Eveline.; Wagemaker, Marnix. ACS Appl. Energy Mater. 2018, 1(7), 3230–324.

[187] Koettgen, Julius.; Zacherle, Tobias.; Grieshammer, Steffen.; Martin, Manfred. Phys. Chem. Chem. Phys. 2017, 19 (15), 9957–9973.

[188] Jia, Mingzhen.; Wang, Hongyan.; Sun, Zhandong.; Chen, Yuanzheng.; Guo, Chunsheng.; Gan, Liyong. RSC Adv. 2017, 7 (42), 26089–26096.

[189] Benzidi, H.; Lakhal, M.; Benyoussef, A.; Hamedoun, M.; Loulidi, M.; El kenz, A.; Mounkachi, O. Int. J. Hydrogen Energy. 2017, 42 (30), 19481–19486.

[190] Rkhis, M.; Laasri, S.; Touhtouh, S.; Hlil, E. K.; Bououdina, M.; Ahuja, R.; Zaidat, K.; Obbade, S.; Hajjaji, A. Int. J. Hydrogen Energy. 2022, 47(5), 3022–3032.

[191] Ji, Hongmei.; Yang, Gang.; Ni, Huan.; Roy, Soumyajit.; Pinto, João.; Jiang, Xuefan.

Electrochim. Acta. 2011,56 (9), 3093–3100.

[192] Dong, Youzhong.; Wang, Long.; Zhang, Shouliang.; Zhao, Yanming.; Zhou, Jiping.; Xie, Hui.; Goodenough, John B. J. Power Sources. 2012, 215, 116–121.

[193] Chang, Longjiao.; Bi, Xiaolong.; Luo, Shaohua.; Cao, Shiyuan.; Wei, Anlu.; Yang, Wei.; Liu, Jianan.; Zhang, Fusheng. Int. J. Energy Res. 2021, 45 (15), 20715–20728.

[194] Qin, Laifen; Xia, Yonggao.; Qiu, Bao.; Cao, Hailiang.; Liu, Yuanzhuang.; Liu, Zhaoping. J. Power Sources. 2013, 239, 144–150.

[195] Martha, Surendra K.; Haik, Ortal.; Borgel, Valentina.; Zinigrad, Ella.; Exnar, Ivan.; Drezen, Thierry.; Miners, James H.; Aurbach, Doron. J. Electrochem. Soc. 2011, 158 (7), A790.

[196] Di Lecce, Daniele.; Hu, Tao.; Hassoun, Jusef. J. Alloys Compd. 2017, 693, 730–737.

[197] Fisher, Craig A J.; Prieto, Veluz M Hart.; Islam, M Saiful. Chem. Mater. 2008, 4 (16), 5907–5915.

[198] Kanungo, Sayan.; Bhattacharjee, Ankur.; Bahadursha, Naresh.; Ghosh, Aritra. Nanomaterials. 2022, 12 (19), 3266.

[199] Islam, M. Saiful.; Driscoll, Daniel J.; Fisher, Craig A.J.; Slater, Peter R. Chem. Mater. 2005, 17 (20), 5085–5092.

[200] Gardiner, Grahame R.; Islam, M. Saiful. Chem. Mater. 2010, 22 (3), 1242–1248.

[201] Guo, Xiuping.; Wang, Min.; Huang, Xiaolan.; Zhao, Pengfei.; Liu, Xialin.; Che, Renchao. J. Mater. Chem. A. 2013, 1 (31), 8775–8781.

[202] Chen, Jiajun.; Graetz, Jason. ACS Appl. Mater. Interfaces. 2011, 3 (5), 1380–1384.

[203] Chung, Sung Yoon.; Choi, Si Young.; Yamamoto, Takahisa.; Ikuhara, Yuichi. Phys. Rev. Lett. 2008, 100 (12), 1–4.

[204] Paolella, Andrea.; Turner, Stuart.; Bertoni, Giovanni.; Hovington, Pierre Flacau, Roxana.; Boyer, Chad.; Feng, Zimin.; Colombo, Massimo.; Marras, Sergio.; Prato, Mirko.; Manna, Liberato.; Guerfi, Abdelbast.; Demopoulos, George P.; Armand, Michel.; Zaghib, Karim. Nano Lett. 2016, 16 (4), 2692–2697.

[205] Paolella, Andrea.; Bertoni, Giovanni.; Hovington, Pierre Feng, Zimin.; Flacau, Roxana.; Prato, Mirko.; Colombo, Massimo Marras, Sergio.; Manna, Liberato.; Turner, Stuart.; Van Tendeloo, Gustaaf.; Guerfi, Abdelbast.; Demopoulos, George P.; Zaghib, Karim. Nano Energy. 2015, 16, 256–267.

[206] Yang, Li; Deng, Wentao.; Xu, Wei.; Tian, Ye.; Wang, Anni.; Wang, Baowei.; Zou, Guoqiang.; Hou, Hongshuai.; Deng, Weina.; Ji, Xiaobo. J. Mater. Chem. A. 2021, 9 (25), 14214–14232.

Appendices

Appendix A | $LiMn_{1-x}M_xPO_4$ (M=Ni, Fe) supplementary material

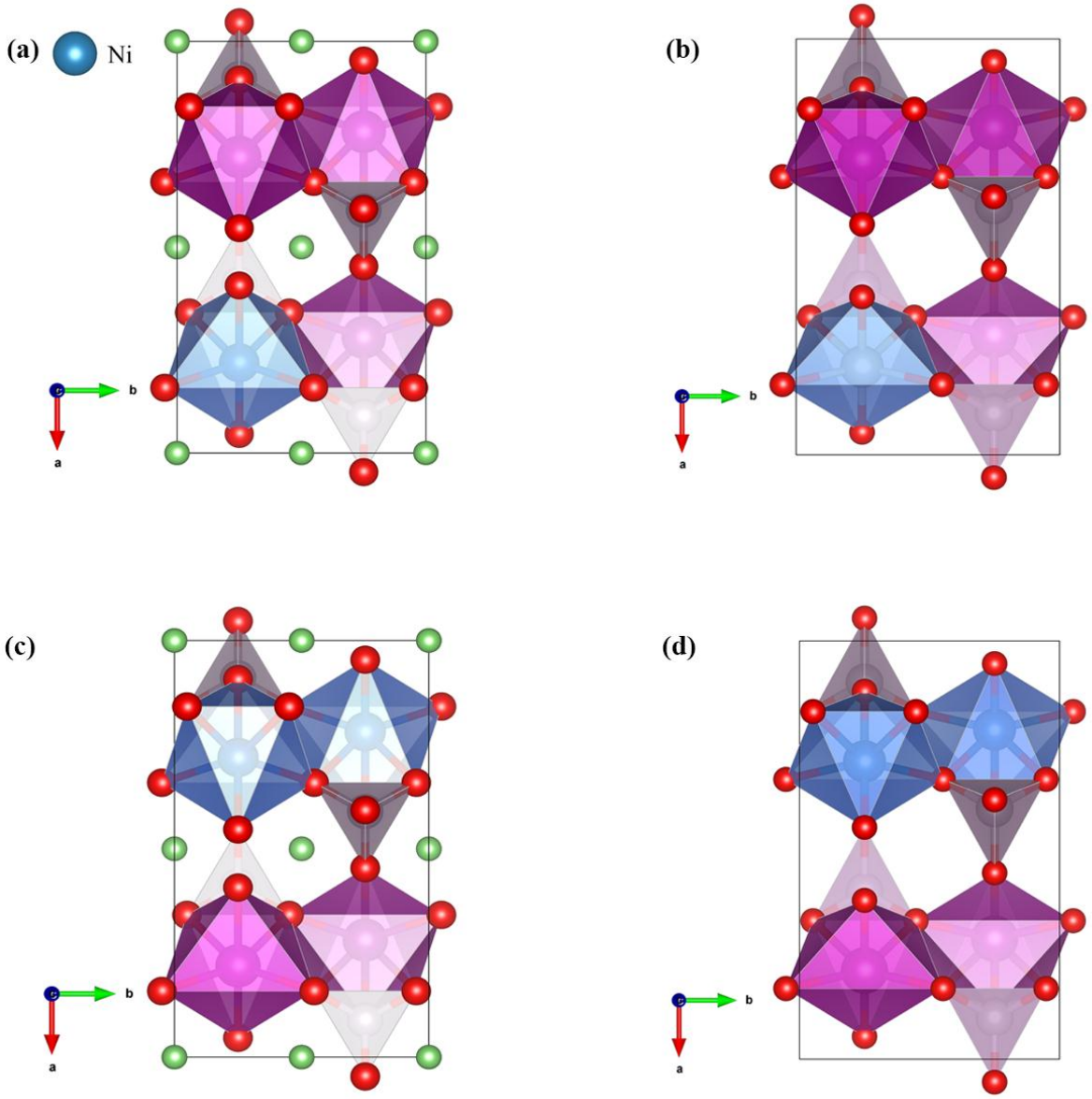

(e)

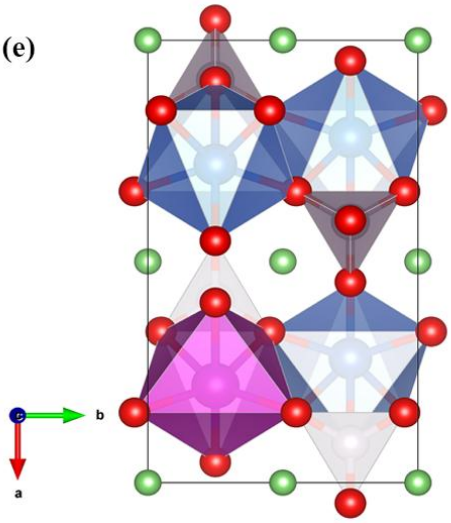

(f)

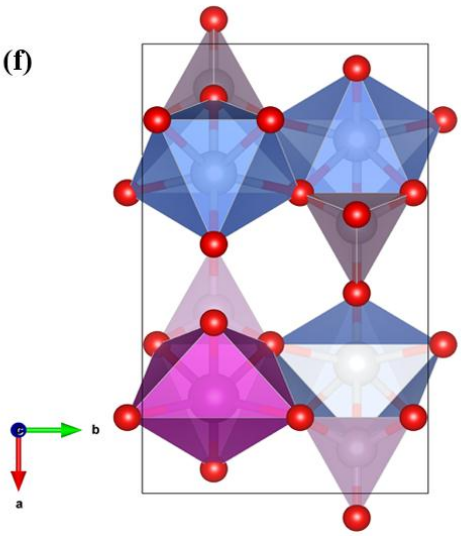

(g)

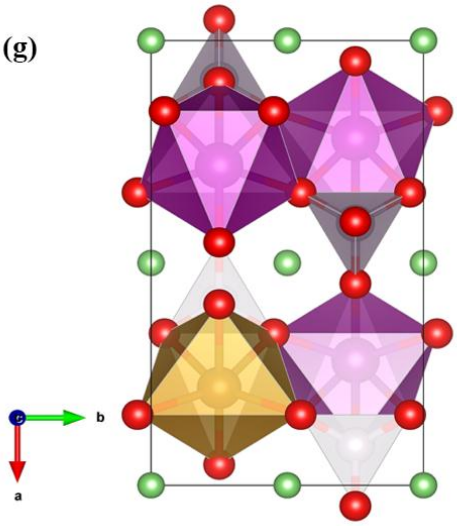

(h)

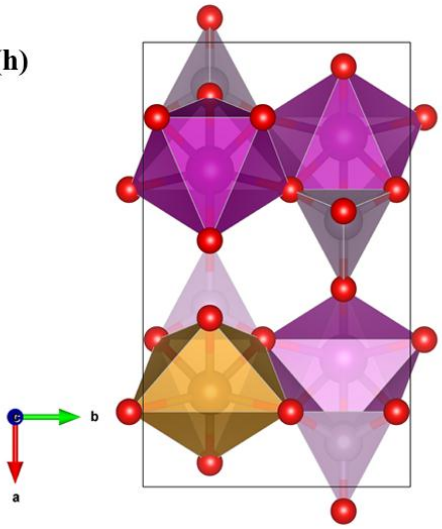

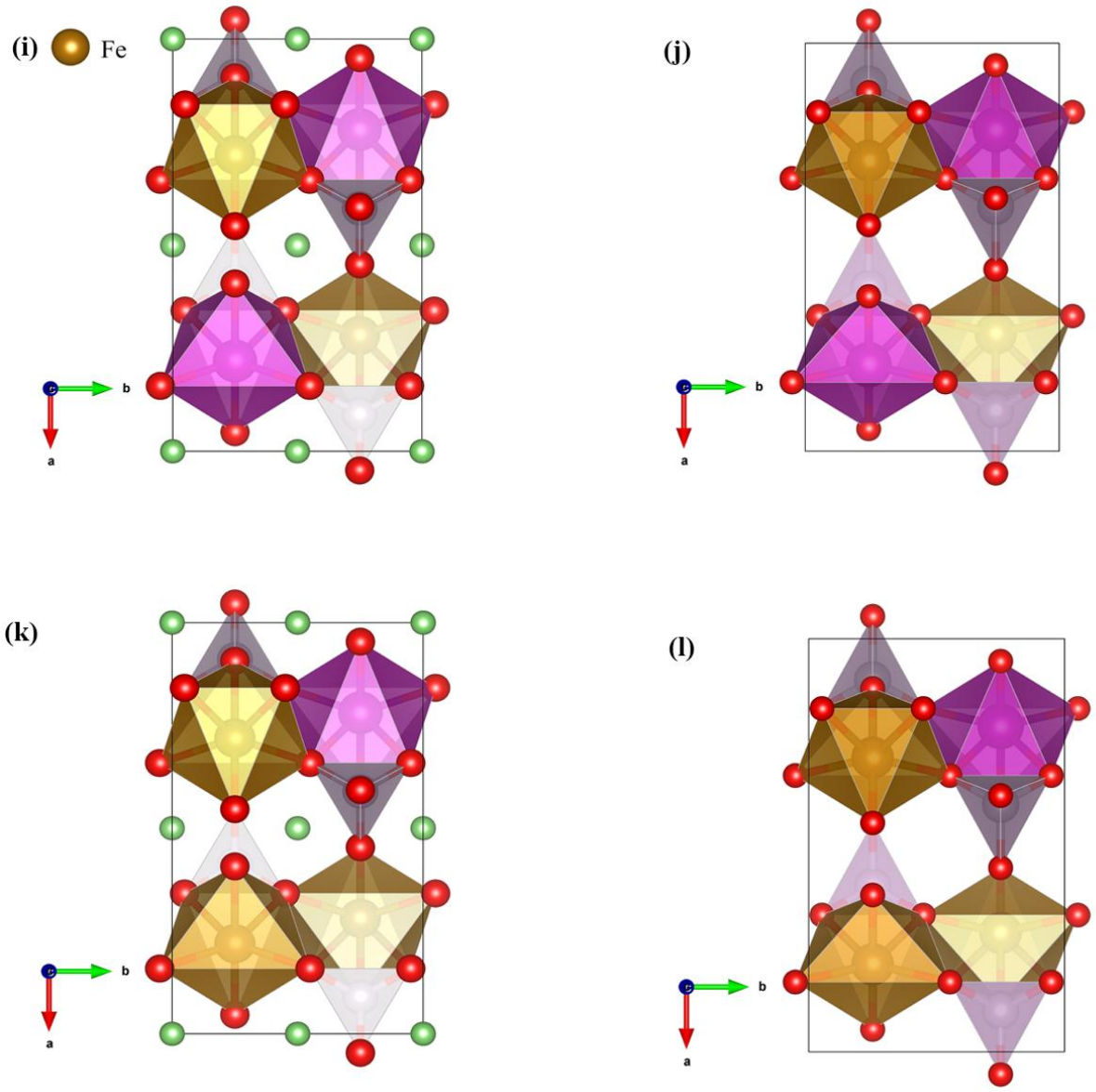

Figure A.1: Crystallographic structures of (a) $LiMn_{0.75}Ni_{0.25}PO_4$, (b) $Mn_{0.75}Ni_{0.25}PO_4$, (c) $LiMn_{0.5}Ni_{0.5}PO_4$, (d) $Mn_{0.5}Ni_{0.5}PO_4$ and (e) $LiMn_{0.25}Ni_{0.75}PO_4$ and (f) $Mn_{0.25}Ni_{0.75}PO_4$, (g) $LiMn_{0.75}Fe_{0.25}PO_4$, (h) $Mn_{0.75}Fe_{0.25}PO_4$, (i) $LiMn_{0.5}Fe_{0.5}PO_4$, (j) $Mn_{0.5}Fe_{0.5}PO_4$, (k) $LiMn_{0.25}Fe_{0.75}PO_4$ (l) $Mn_{0.25}Fe_{0.75}PO_4$. purple , Brown and blue are MnO_6, FeO_6 and NiO_6 octahedral units, respectively.

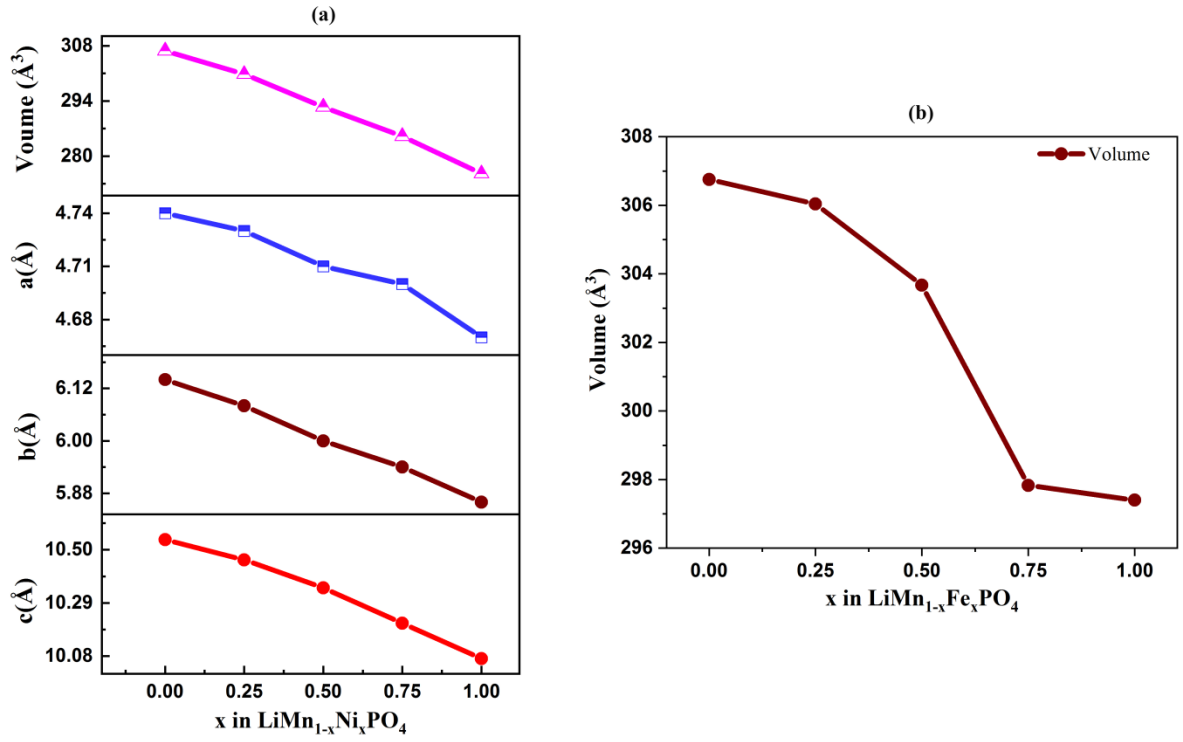

Figure A.2: (a) Lattice parameters a, b, and c and resulting unit cell volume V of $LiMn_{1-x}Ni_xPO_4$ (x=0, 0.25, 0.5, 0.75,1) and (b) unit cell volume V of $LiMn_{1-x}Fe_xPO_4$ (x=0, 0.25, 0.5, 0.75,1).

Table A.2: Calculated bond lengths (M'−O) in both structures $LiMn_{1-x}M_xPO_4/Mn_{1-x}M_xPO_4$.

(x=0, 0.25, 0.5, 0.75, 1).

(a)

	x	Mn-O(Å)						Ni-O(Å)					
		O1	O2	O3	O3	O3'	O3'	O1	O2	O3	O3	O3'	O3'
$LiMn_{1-x}Ni_xPO_4$	0	2.284	2.173	2.296	2.296	2.156	2.156						
	0.25	2.247	2.207	2.289	2.289	2.151	2.151	2.149	2.059	2.170	2.170	2.102	2.102
	0.5	2.293	2 .177	2.285	2.285	2.138	2.138	2.106	2.043	2.164	2.164	2.088	2.088
	0.75	2.241	2.152	2.272	2.272	2.132	2.132	2.124	2.052	2.157	2.157	2.076	2.076
	1							2.103	2.044	2.144	2.144	2.054	2.054
$Mn_{1-x}Ni_xPO_4$	0	1.938	1.933	2.354	2.354	2.040	2.040						

	0.25	1.935	1.931	2.267	2.267	2.035	2.035	1.945	1.936	2.189	2.189	2.074	2.074
	0.5	1.941	1.939	2.235	2.235	2.028	2.028	1.945	1.937	2.152	2.152	2.060	2.060
	0.75	1.946	1.939	2.149	2.149	2.020	2.020	1.955	1.939	2.140	2.140	2.029	2.029
	1							1.968	1.944	2.119	2.119	2.014	2.014

(b)

	x	Mn-O(Å)						Fe-O(Å)					
		O1	O2	O3	O3	O3'	O3'	O1	O2	O3	O3	O3'	O3'
$LiMn_{1-x}Fe_xPO_4$	0	2.284	2.173	2.296	2.296	2.156	2.156						
	0.25	2.291	2.178	2.302	2.302	2.236	2.236	2.254	2.135	2.253	2.253	2.112	2.112
	0.5	2.288	2 .171	2.306	2.306	2.153	2.153	2.253	2.139	2.254	2.254	2.102	2.102
	0.75	2.279	2.169	2.301	2.301	2.145	2.145	2.125	2.124	2.258	2.258	2.078	2.078
	1							2.225	2.136	2.270	2.270	2.084	2.084
$Mn_{1-x}Fe_xPO_4$	0	1.938	1.933	2.354	2.354	2.040	2.040						
	0.25	1.947	1.926	2.286	2.286	2.053	2.053	1.944	1.905	2.988	1.988	2.066	2.066
	0.5	1.928	1.905	2.349	2.349	2.050	2.050	1.956	1.935	2.158	2.158	2.029	2.029
	0.75	1.933	1.907	2.371	2.371	2.039	2.039	1.935	1.926	2.165	2.165	2.059	2.059
	1							1.934	1.923	2.161	2.161	2.069	2.069

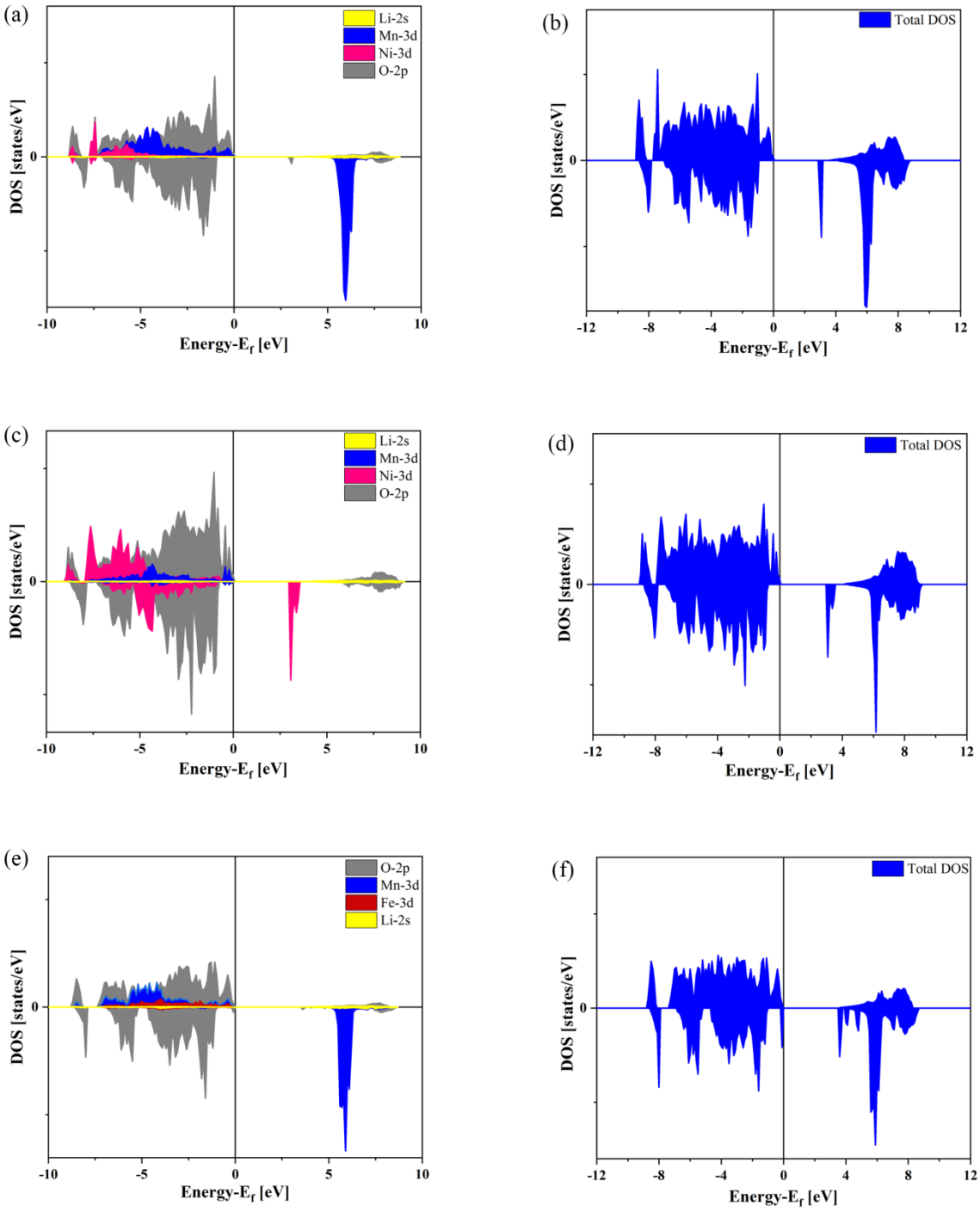
(a)
Li-2s
Mn-3d
Ni-3d
O-2p
DOS [states/eV]
Energy-E$_f$ [eV]
(b)
Total DOS
DOS [states/eV]
Energy-E$_f$ [eV]
(c)
Li-2s
Mn-3d
Ni-3d
O-2p
DOS [states/eV]
Energy-E$_f$ [eV]
(d)
Total DOS
DOS [states/eV]
Energy-E$_f$ [eV]
(e)
O-2p
Mn-3d
Fe-3d
Li-2s
DOS [states/eV]
Energy-E$_f$ [eV]
(f)
Total DOS
DOS [states/eV]
Energy-E$_f$ [eV]

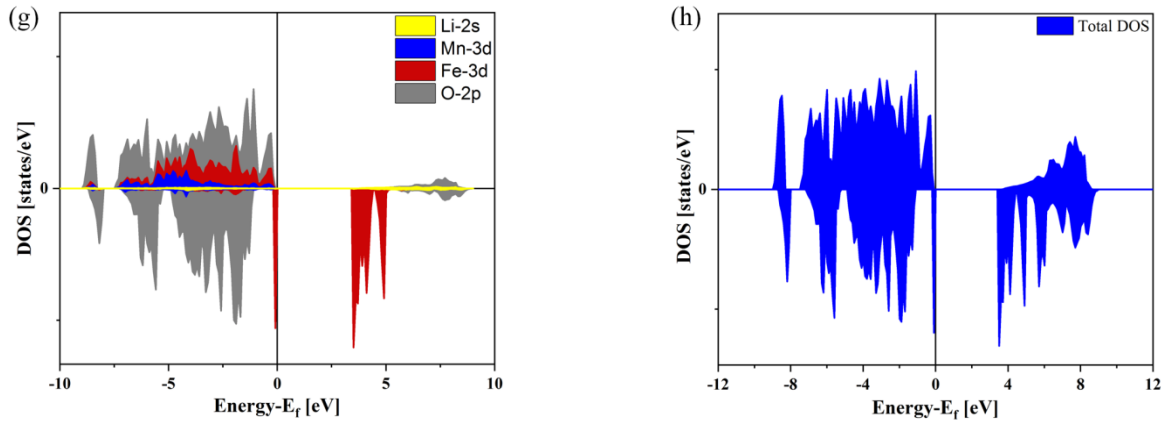

Figure A.3: Projected DOS of (a) $LiMn_{0.75}Ni_{0.25}PO_4$, (c) $LiMn_{0.25}Ni_{0.75}PO_4$ (e) $LiMn_{0.75}Fe_{0.25}PO_4$ and (g) $LiMn_{0.25}Fe_{0.75}PO_4$ and total DOS of (b) $LiMn_{0.75}Ni_{0.25}PO_4$and (d) $LiMn_{0.25}Ni_{0.75}PO_4$, (f) $LiMn_{0.75}Fe_{0.25}PO_4$ and (h) $LiMn_{0.25}Fe_{0.75}PO_4$.

Table A.1: The average bond lengths (M'-O) in MO6 octahedral of LiMnxM1-xPO4 (x=0, 0.25, 0.5, 0.75, 1).

	x	Average Distance Mn-O(Å)	Average Distance Ni-O(Å)
$LiMn_{1-x}Ni_xPO_4$	**0**	**2.227**	
	0.25	**2.222**	**2.125**
	0.5	**2.219**	**2.109**
	0.75	**2.200**	**2.105**
	1		**2.090**
	x	**Average Distance Mn-O(Å)**	**Average Distance Fe-O(Å)**
$LiMn_{1-x}Fe_xPO_4$	**0**	**2.227**	
	0.25	**2.231**	**2.186**
	0.5	**2.229**	**2.184**
	0.75	**2.223**	**2.170**
	1		**2.178**

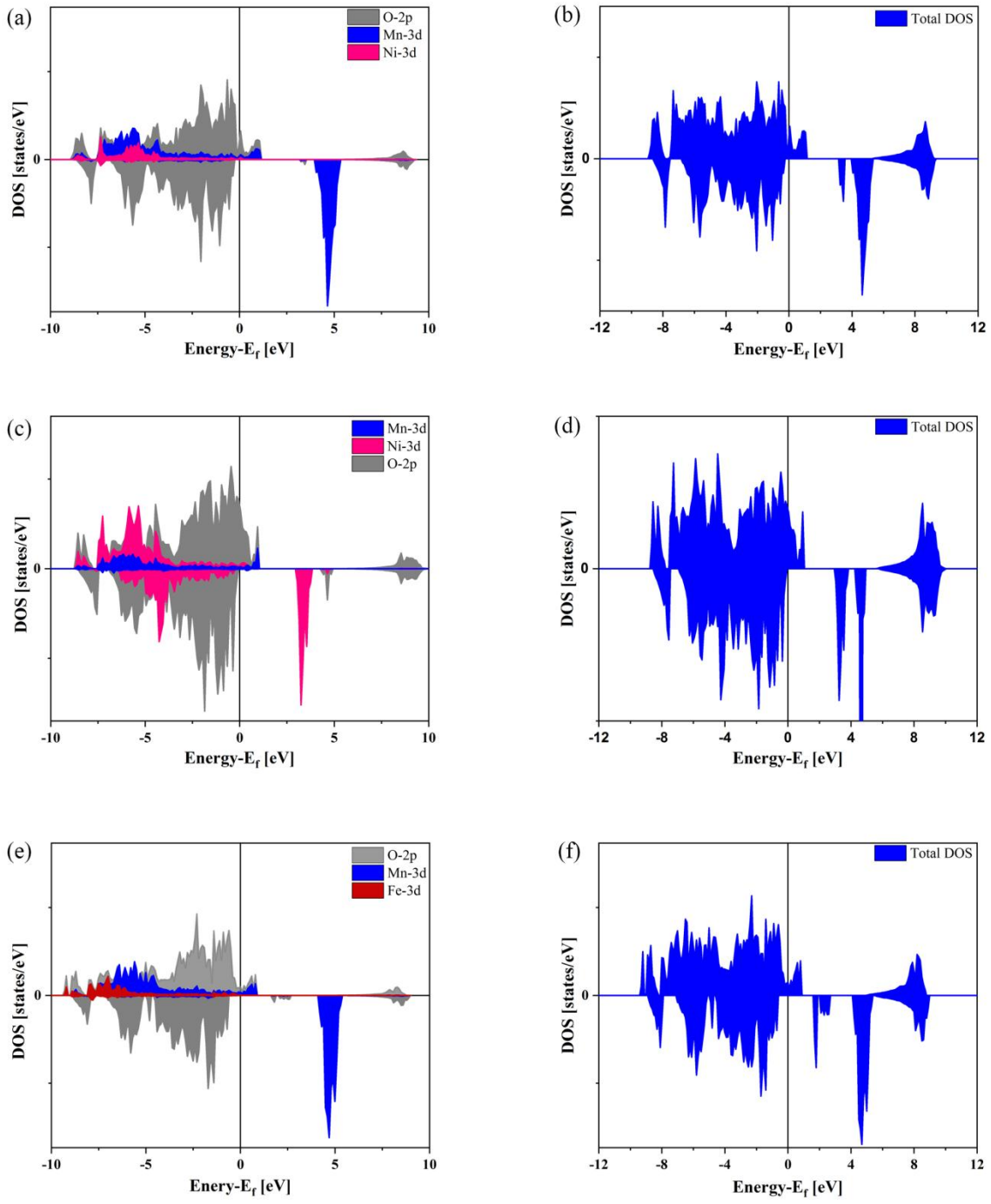
(a)
O-2p
Mn-3d
Ni-3d
DOS [states/eV]
Energy-E$_f$ [eV]
(b)
Total DOS
DOS [states/eV]
Energy-E$_f$ [eV]
(c)
Mn-3d
Ni-3d
O-2p
DOS [states/eV]
Energy-E$_f$ [eV]
(d)
Total DOS
DOS [states/eV]
Energy-E$_f$ [eV]
(e)
O-2p
Mn-3d
Fe-3d
DOS [states/eV]
Enery-E$_f$ [eV]
(f)
Total DOS
DOS [states/eV]
Energy-E$_f$ [eV]

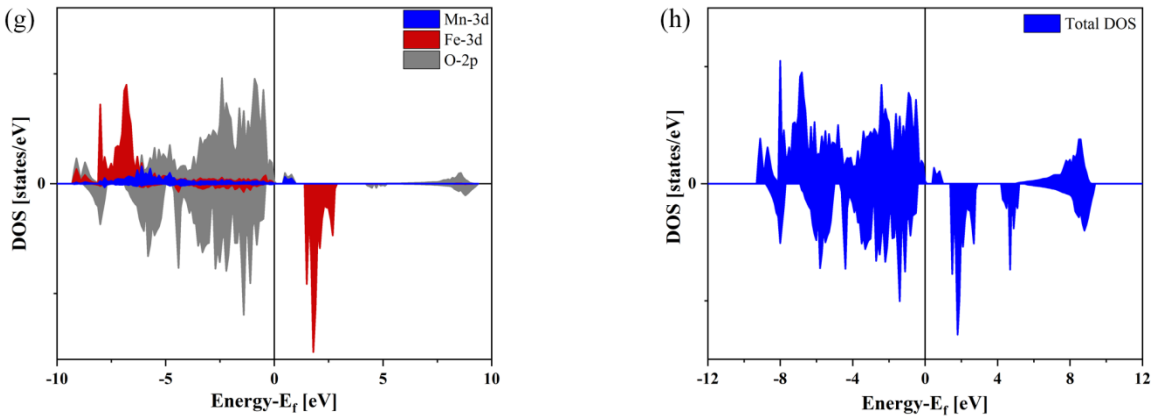

Figure A.4: Projected DOS of (a) $Mn_{0.75}Ni_{0.25}PO_4$, (c) $Mn_{0.25}Ni_{0.75}PO_4$ (e) $Mn_{0.75}Fe_{0.25}PO_4$ and (g) $Mn_{0.25}Fe_{0.75}PO_4$ and total DOS of (b) $Mn_{0.75}Ni_{0.25}PO_4$and (d) $Mn_{0.25}Ni_{0.75}PO_4$,(f) $Mn_{0.75}Fe_{0.25}PO_4$ and (h) $Mn_{0.25}Fe_{0.75}PO_4$.

Appendix B | Strain effects on the electrochemical performance of LiMnPO4 supplementary material

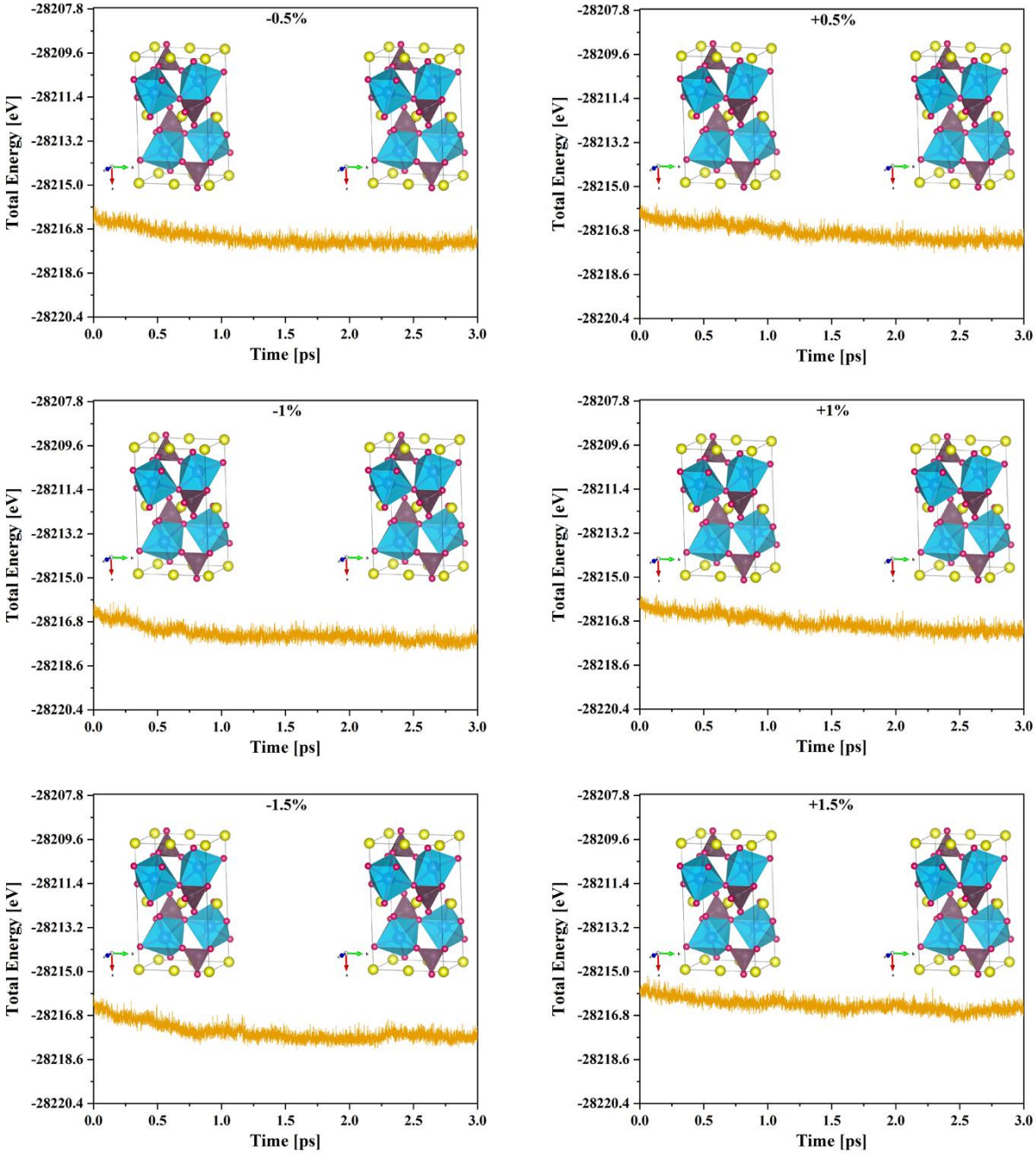

Figure B.1: Total energy variation during a simulation of 3 ps at room temperature of strained LMP systems. Snapshots of strained structures at the end of MD simulation are inserted in figures.

Table B.1: Net Charges of Atoms in Unstrained and Strained Compounds and Their Delithiated Phases.

Strained LMP		Net charge					
		Li	Mn	P	O1	O2	O3
-2.5%	LMP	0.89	1.58	5	-1.89	-1.88	-1.83
	MP		1.69	5	-1.71	-1.66	-1.61
0%	LMP	0.89	1.57	5	-1.90	-1.88	-1.82
	MP		1.68	5	-1.70	-1.66	-1.60
+2%	LMP	0.90	1.58	5	-1.90	-1.87	-1.82
	MP		1.67	5	-1.70	-1.65	-1.60

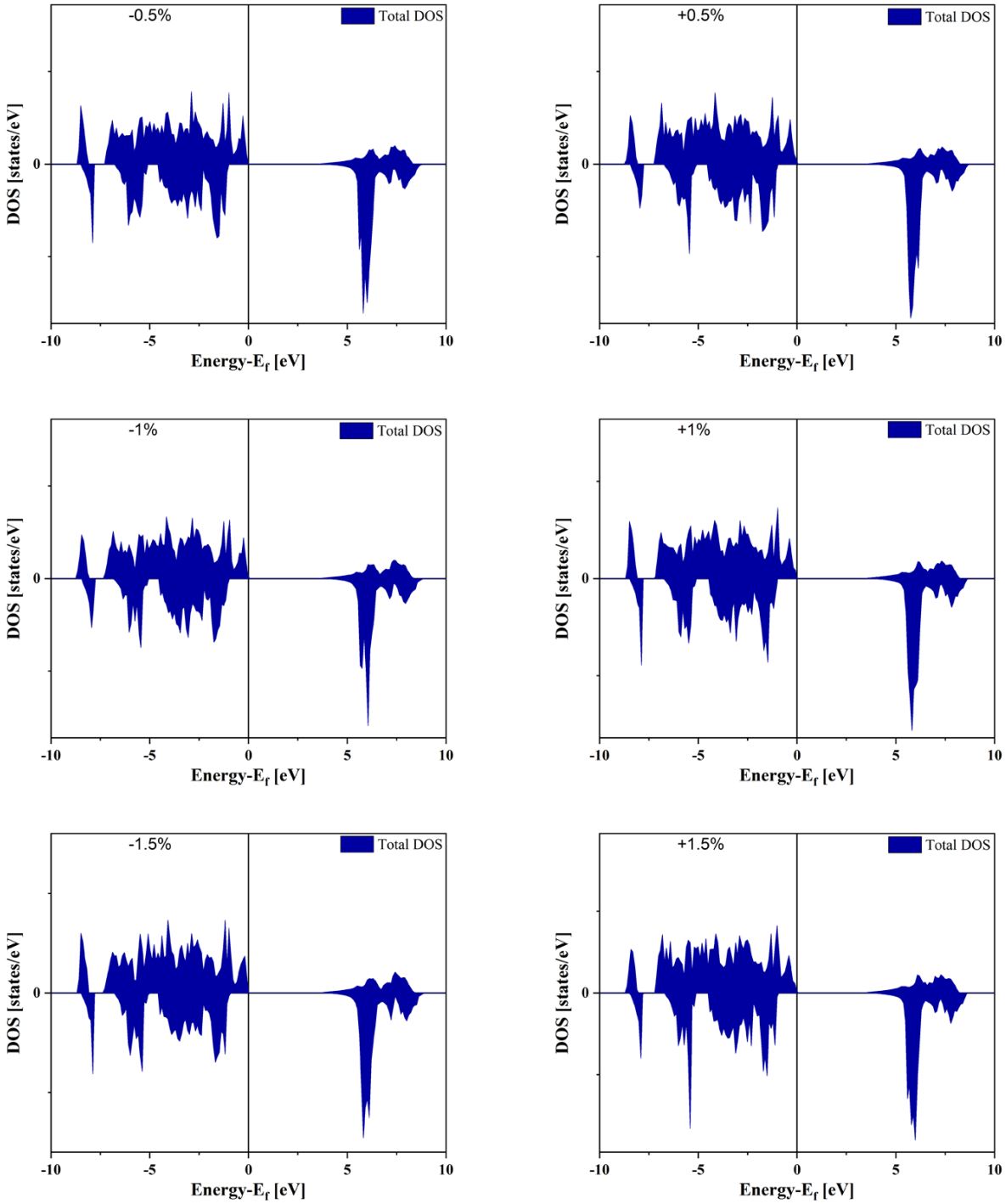

Figure B.2: Total DOS of strained LMP compounds.

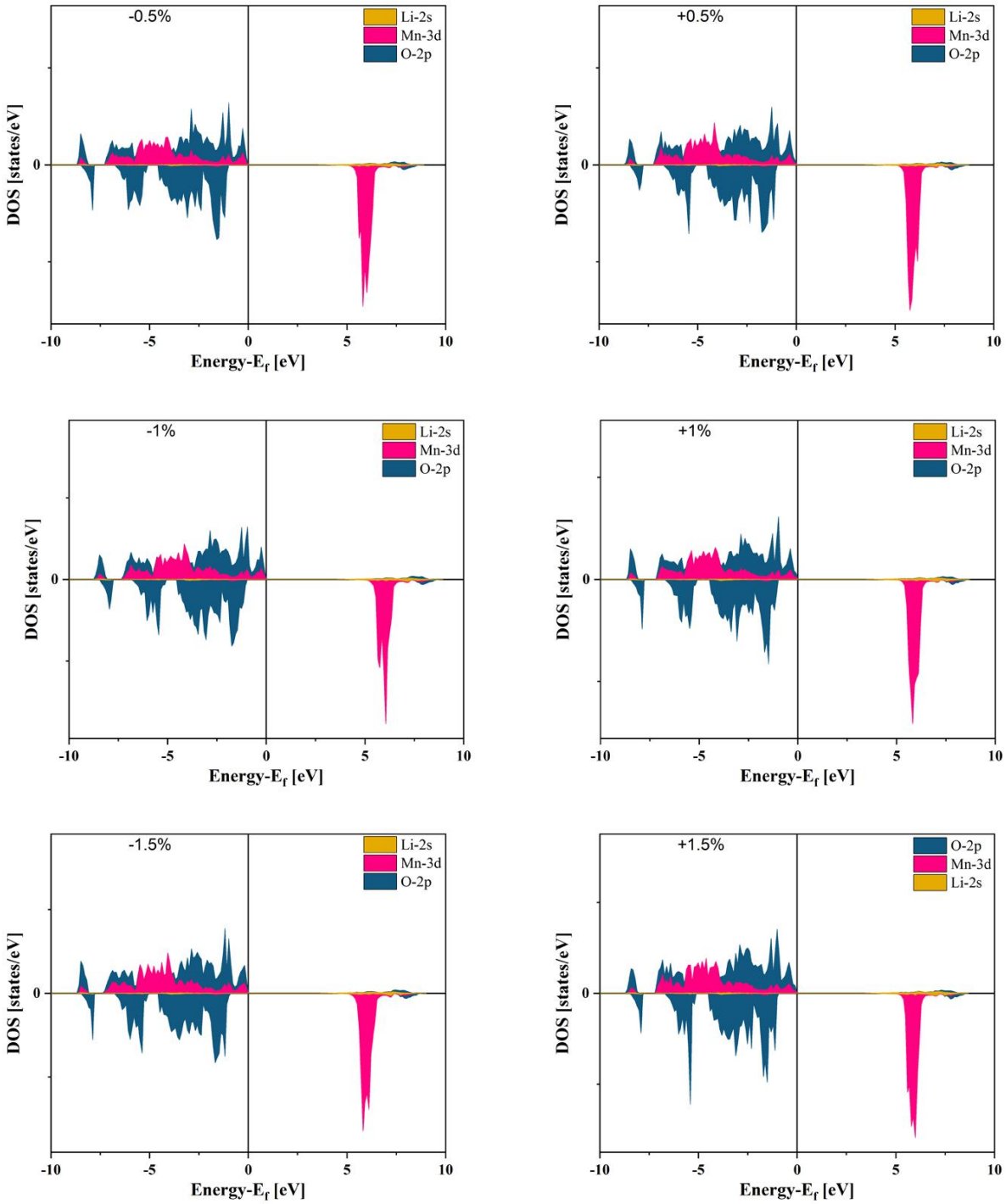

Figure B.3: Projected DOS of strained LMP compounds.